

NORTHWESTERN UNIVERSITY

Hybrid Incremental Sheet Forming Methods for Enhanced Process Performance and Material  
Properties

A DISSERTATION

SUBMITTED TO THE GRADUATE SCHOOL  
IN PARTIAL FULFILLMENT OF THE REQUIREMENTS

for the degree

DOCTOR OF PHILOSOPHY

Field of Mechanical Engineering

By

Zixuan Zhang

EVANSTON, ILLINOIS

September 2018

© Copyright by Zixuan Zhang 2018

All Rights Reserved

## **Abstract**

Demands in the aerospace, automotive and biomedical sectors for low-volume sheet metal parts made from materials with high specific strength are growing due to the needs imposed by rapid product development cycles, and personalized products to mention a few. However, high strength-to-weight ratio materials, such as Ti6Al4V, are usually difficult to form at room temperature necessitating the use of complex and costly hot forming processes. Alternatively, processes with combined actions of local deformation and heating, such as Electrically-assisted Incremental Sheet Forming (EA-ISF), are attractive when compared to conventional methods due to their increased process flexibility, decreased equipment capacity requirements, and shortened production cycles. In EA-ISF, the absence of a geometry-specific punch and die makes this process ideal for industries with small batch production runs. A few technical issues, however, hinder the wide commercialization of EA-ISF. Major roadblocks include the limited geometric accuracy of the final parts, unstable electric circuits during processing and the lack of in-depth knowledge on the material's responses during processing and on the achieved product properties such as formability, hardness, surface topography and fatigue. Additionally, the dominant mechanisms behind electrically-assisted manufacturing processes remain a debatable research topic.

To address the aforementioned issues, this work aims to: 1) improve the geometric accuracy of the final parts along with process efficiency, 2) realize the capability of deforming materials that are hard-to-form at room temperature, 3) unveil the dominant mechanisms behind the coupled electro-thermo-mechanical loading, and 4) enhance the performance of materials processed by EA-ISF.

Specifically, this thesis develops a novel hybrid ISF process that synergizes the desirable features of two different ISF processing modes. This strategy, in which the material is pre-strained followed by a low-force fine-tuning process, ensures the robustness, doubles forming efficiency and secures contact between the tools and the sheet metal. As such it was used as the basis for the development of two alternative variants of hybrid EA-ISF processes. Using this method, the forming depth has been increased by 115% compared to conventional EA-ISF. A practical post-forming annealing process that significantly increases geometric accuracy (up to 95%) is developed thereafter. This thesis discovers that apart from sparks, large forming forces limit the capability of deforming hard-to-form material in EA-ISF as well.

To identify the dominant deformation mechanisms under electro-thermo-mechanical loading, a novel *in situ* characterization method for the material's microstructure responses under macroscopic EA tensile loading is established. Combining both the material's macroscopic and microstructural responses, this thesis refutes the existence of electrical-specific athermal effects in Ti6Al4V, regardless of the different patterns of electricity applied. Finally, an in-depth investigation of the resulting microstructures and material properties, obtained in ISF processes, is carried out. This thesis reveals the key factors that affect the material's formability, hardness, surface quality, and fatigue life.

The ability to easily and rapidly manufacture sheet metal parts with the desired geometric accuracy and material properties, will unlock an entirely new design domain in product development that will allow for the continuing improvements in the processing and use of strong, lightweight parts in manufacturing industries. The methods and results generated in this work will contribute to the understanding and development of other manufacturing processes that are flexible

or hybrid in nature. These could include processing ideas such as electrically-assisted rolling, electrically-assisted tube forming, on-site annealing and electrically-assisted vibrational surface treatment.

## Acknowledgements

During my Ph.D. study, there has not been greater fortune that is comparable to the continuous support given by my committee members, collaborators, friends, and family.

I would like to first express the sincerest gratitude to my committee members Professor Jian Cao, Professor Kornel Ehmann, and Professor Gregory Olson for their valuable suggestions, guidance, and insights. They not only delivered professional knowledge, but also influenced me to strive for their enthusiasm, responsibility, and perseverance.

I would like to acknowledge the financial support from the Energy Efficiency and Renewable Energy Research Fellowship, made possible by Dr. David Forrest and the U.S. Department of Energy.

I would also like to thank my supportive collaborators Dr. Yang Ren and Fangmin Guo at Argonne National Laboratory, Beatrice Valoppi at the University of Padova, Antonio Sánchez Egea at the Universitat Politècnica de Catalunya, Mohammad Ali Davarpanah at Oregon State University, Taekyung Lee at Kumamoto University, Huan Zhang at Shanghai Jiao Tong University, and all the past and current members of the Advanced Manufacturing Processes Laboratory for their devout encouragement, engaging discussions, and quality assistance.

This work could not be carried out without the assistance and equipment provided by the shared facilities at Northwestern University. I would like to thank the managers of those facilities: Mark Seniw from the Central Laboratory for Materials Mechanical Properties, Carla Shute from the Materials Characterization and Imaging Facility, Jerry Carsello from the J.B. Cohen X-Ray Diffraction Facility, Scott Simpson and Robert Taglia from the machine shop.

Acknowledgement is also due for my dearest friends who always offered wholehearted support: Li Zeng, Rui Xu, Xiangfan Chen, Lingxuan Peng, Ping Guo, Jiachen Xu, Yichi Zhang, Jiawei Fu, Zijiang Yang, Xiaolin Li, Yunli Shao, Jiali Liu, Chengyi Song, and Zheren Ma.

Finally, I owe my deepest gratitude to my parents for raising me. I see the beauty of the world because of you; I see who I am because of you; I persist and love because of you.

## Table of Contents

<b>Abstract</b> .....	3
<b>Acknowledgements</b> .....	6
<b>List of figures</b> .....	14
<b>List of tables</b> .....	21
<b>Chapter 1: Introduction</b> .....	23
1.1 Background and motivation .....	23
1.2 Research objectives .....	26
1.3 Outline of the thesis.....	27
<b>Chapter 2: Incremental Sheet Forming (ISF) process for enhanced in-process     geometric accuracy</b> .....	30
2.1 Literature review of Incremental Sheet Forming (ISF).....	30
2.1.1 Single Point Incremental Forming (SPIF) .....	32
2.1.2 Double-sided Incremental Forming (DSIF).....	33
2.1.3 Accumulative Double-sided Incremental Forming (ADSIF) .....	33
2.2 Mixed Double-sided Incremental Forming (MDSIF) for improved in-process geometric accuracy and efficiency .....	36
2.2.1 Experimental setup.....	37
2.2.2 Toolpath parameters.....	39



	9
2.2.3 Measurement of geometric deviations .....	41
2.3 Results .....	43
2.3.1 Geometric accuracy .....	43
2.3.2 Thickness profiles .....	47
2.3.3. Force histories .....	48
2.4 Summary .....	51

**Chapter 3: Process design for post-forming annealing methods that increase**

<b>geometric accuracy after unclamping and trimming processes .....</b>	<b>52</b>
3.1 Literature review of springback in ISF .....	52
3.2 Design of clamping devices for annealing processes .....	55
3.3 Methods for selecting the annealing parameters .....	56
3.4 Reducing springback in the unclamping process .....	59
3.4.1 Experimental setup .....	60
3.4.2 Springback evaluation method for the unclamping process .....	61
3.4.3 Results .....	63
3.5 Reducing springback in the trimming process .....	66
3.5.1 Experimental setup .....	68
3.5.2 Springback evaluation method for the trimming process .....	69
3.5.3 Results .....	70

	10
3.6 Mechanisms of stress-relief annealing .....	71
3.6.1 Residual stresses .....	71
3.6.2 The recovery stage of annealing .....	73
3.7 Summary .....	75

#### **Chapter 4: Electrically-assisted Double-sided Incremental Forming(EA-DSIF) methods**

<b>for hard-to-form materials</b> .....	76
4.1 Literature review of electrically-assisted (EA) manufacturing processes .....	76
4.2 Electrically-assisted Conventional Double-sided Incremental Forming (EA-cDSIF) .	81
4.2.1 Experimental setup.....	81
4.2.2 Results.....	84
4.3 Development of Electrically-assisted Accumulative Double-sided Incremental Forming (EA-ADSIF) .....	89
4.3.1 Methodology .....	89
4.3.2 Results.....	90
4.3.3 Determination of the actual forming temperature.....	96
4.4 Development of Electrically-assisted Mixed Double-sided Incremental Forming (EA- MDSIF) .....	99
4.4.1 Experimental setup.....	100
4.4.2 Results.....	100

	11
4.5 Implementation of Electrically-assisted post-forming annealing treatment.....	102
4.5.1 Experimental setup.....	102
4.5.2 Results.....	103
4.6 Summary .....	106
<b>Chapter 5: Discovery of the mechanisms of electro-thermo-mechanical processes.....</b>	<b>107</b>
5.1 Literature review of the mechanisms of electro-thermo-mechanical loading processes .....	107
5.2 <i>In/ex situ</i> X-ray diffraction study .....	117
5.3 Electrically-assisted tensile tests .....	120
5.2.1 Experimental setup.....	120
5.2.2 Results.....	123
5.4 Microstructural responses under electro-thermal-mechanical loading .....	126
5.5 Microstructure evolution under pure thermal condition.....	130
5.5.1 <i>In situ</i> XRD study in annealing conditions .....	130
5.5.2 Kinetic simulations for diffusion-based phase transformation .....	133
5.6 Summary .....	136
<b>Chapter 6: Enhancement of material properties through EA-DSIF processes .....</b>	<b>137</b>
6.1 Formability .....	137
6.1.1 Investigation of fracture mechanics in EA-cDSIF.....	138

	12
6.1.2 Results and discussion .....	141
6.2 Hardness .....	149
6.3 Surface topography.....	152
6.3.1 Effects of the material’s initial states and strain levels.....	153
6.3.2 Effects of toolpath strategy .....	155
6.3.3 Effects of electricity and tool material.....	160
6.4 Fatigue life.....	165
6.4.1 Fatigue life measurements .....	167
6.4.2 Residual stress measurements.....	169
6.5 Summary .....	173
<b>Chapter 7: Summary and future directions .....</b>	<b>174</b>
7.1 Summary .....	174
7.2 Future directions.....	176
7.2.1 On-site annealing .....	176
7.2.2 DSIF for post-treatment: EA vibrational surface treatment.....	177
7.2.3 Residual stress analysis due to non-uniform deformation and heating.....	178
<b>References.....</b>	<b>180</b>
<b>Appendix A .....</b>	<b>194</b>
<b>Appendix B.....</b>	<b>206</b>

**Appendix C**..... 208

## List of figures

Figure 1.1 GDP from manufacturing in the United States.....	24
Figure 1.2 The outline of the thesis .....	28
Figure 2.1 Toolpath strategies in incremental forming: (a) SPIF; (b) DSIF; (c) ADSIF (Zhang et al., 2015) .....	32
Figure 2.2 Improved geometric accuracy for a 40°cone with ADSIF and the influence of incremental depth in ADSIF on geometric accuracy (data obtained from (Malhotra et al., 2012a)) .....	35
Figure 2.3 (a) CAD model of desired geometry; (b) formed part.....	37
Figure 2.4 DSIF machine system: (a) DSIF machine; (b) forming tools; (c) clamping system ...	38
Figure 2.5 Definition of tool positioning parameters: (a) squeeze factor $s$ in DSIF; (b) $S$ and $D$ in ADSIF .....	39
Figure 2.6 Comparison between a contour and a spiral toolpath in ADSIF: (a) toolpath; (b) geometric accuracy .....	40
Figure 2.7 Definition of geometric error used in this work .....	42
Figure 2.8 3D shape deviation contour for a part formed by DSIF $\Delta Z=100 \mu m, s=1.0$ .....	43
Figure 2.9 Experimentally measured geometric deviation .....	44
Figure 2.10 Geometries formed with a squeeze factor $s=0.75$ with various incremental depths .	46
Figure 2.11 Thickness profiles along a cross section of parts formed by different processes.....	47

Figure 2.12 Z-direction force for $\Delta Z=100 \mu m$ at different $s$ in D-stage: (a) $s=1.0$ ; (b) $s=0.9$ ; (c) $s=0.8$ ; (d) $s=0.75$ .....	49
Figure 2.13 Z-direction force for $\Delta Z=100 \mu m$ at $s=0.8$ in DSIF .....	50
Figure 3.1 Clamp design for the annealing process (unit: $mm$ ): (a) fixed clamp; (b) roller clamp .....	55
Figure 3.2 Annealing parameter selection setup (unit: $mm$ ): (a) specimen dimension; (b) bending test configuration; (c) clamping before the annealing process; (d) definition of strip angles .....	58
Figure 3.3 Shape recovery of the strips after different annealing processes .....	59
Figure 3.4 Draft of desired geometries (unit: $mm$ ): (a) pyramid; (b) cone .....	60
Figure 3.5 Formed parts after releasing from the clamps: (a) pyramid; (b) cone .....	61
Figure 3.6 Sample 3D deviation map on the original pyramid surface within the clamp: .....	62
Figure 3.7 Examples of freestanding annealed parts: (a) a pyramid part annealed with the fixed clamp at $250^\circ C$ for 1 $hr$ ; (b) a cone part annealed with the roller clamp at $250^\circ C$ for 1 $hr$ .....	63
Figure 3.8 Shape deviation RMS between the freestanding pyramid part and the original part within the clamp.....	64
Figure 3.9 Shape deviation RMS between the freestanding cone part and the original part within the clamp.....	64
Figure 3.10 The geometry of the part from: (a) design; (b) unclamping; (c) trimming .....	67
Figure 3.11 Definition of the angles utilized to evaluate the annealing processes for reducing springback after trimming processes .....	69

	16
Figure 3.12 Shape recovery of the trimmed parts by different annealing methods.....	71
Figure 3.13 Microstructures of the as-received and annealed materials.....	74
Figure 4.1 Hot stamping process chain (Karbasian and Tekkaya, 2010) .....	77
Figure 4.2 Configuration of the experimental set-up of EA-cDSIF .....	82
Figure 4.3 Microstructure of the as-received Ti6Al4V material .....	82
Figure 4.4 CAD drawing of the desired geometry of an acetabular cup used in hip replacement	84
Figure 4.5 Cross-sections of the parts formed by EA-cDSIF .....	85
Figure 4.6 View of the IR camera during the measurement of the EA-DSIF processes .....	86
Figure 4.7 Forming temperature history of EA-cDSIF at 87.5 A .....	86
Figure 4.8 Average forming temperature measured in EA-cDSIF .....	87
Figure 4.9 Measured resultant force histories of: (a) EA-cDSIF at 87.5 A; (b) D-stage of the EA-MDSIF at 87.5 A.....	88
Figure 4.10 Average resultant forces measured in EA-cDSIF .....	88
Figure 4.11 Configuration of the experimental set-up of EA-ADSIF .....	90
Figure 4.12 Cross-sections of the parts formed by EA-ADSIF and EA-MDSIF .....	91
Figure 4.13 Z-direction force history in EA-ADSIF at 100 A .....	92
Figure 4.14 Top and bottom tool normalized resultant forces and associated measured and estimated temperatures in EA-ADSIF .....	93
Figure 4.15 Forming temperature history of the EA-ADSIF baseline.....	94



	17
Figure 4.16 Forming temperature history of the EA-ADSIF 100 <i>A</i> .....	95
Figure 4.17 Color comparison between the samples obtained from the tensile and EA-ADSIF tests. The red box represents the area heated by the induction heating system during the tensile tests.	97
Figure 4.18 Measured temperature via color comparison and estimated temperature using different contact areas.....	98
Figure 4.19 Contact area calculated through FEA simulation.....	99
Figure 4.20 Ti6Al4V acetabular cup obtained with EA-MDSIF 50 <i>A</i> .....	101
Figure 4.21 Ti6Al4V pyramid part using EA-MDSIF 50 <i>A</i> : (a) desired part; (b) formed part ..	101
Figure 4.22 Experimental setup for electrically-assisted on-site annealing .....	103
Figure 5.1 Interactions between mechanical, thermal, electrical, and microstructural phenomena .....	110
Figure 5.2 <i>In situ</i> high-energy XRD measurement setup. The yellow line (from right to left) indicates the X-ray path. ....	118
Figure 5.3 Dimension of the tensile test specimen .....	121
Figure 5.4 Relationships between energy inputs and outputs.....	121
Figure 5.5 Energy inputs, temperature histories and macroscale tensile behaviors in the low temperature group.....	123
Figure 5.6 Energy inputs, temperature histories and macroscale tensile behaviors in the medium temperature group.....	125

Figure 5.7 Energy inputs, temperature histories and macroscale tensile behaviors in the high temperature group .....	126
Figure 5.8 <i>In situ</i> high-energy XRD measurements for EA tensile tests under a continuous current density of $17.5 A/mm^2$ .....	127
Figure 5.9 <i>In situ</i> measurements of $\beta$ phase fraction evolution in: (a) room temperature; (b) low temperature group; (c) medium temperature group; (d) high temperature group.....	129
Figure 5.10 <i>Ex situ</i> XRD patterns for electrically-assisted tension specimen at different locations just after fracture (initial continuous current with density of $17.5 A/mm^2$ ) .....	130
Figure 5.11 Linkam heating stage.....	131
Figure 5.12 <i>In situ</i> XRD measurements of $\beta$ phase fraction evolution during heating .....	132
Figure 5.13 Fraction evolution of $\beta$ phase measured in EA tensile tests and predicted based on annealing condition for: (a) medium temperature group; (b) high temperature group.....	132
Figure 5.14 Backscattered SEM image of as-received Ti6Al4V .....	133
Figure 5.15 Simulated $\beta$ phase fraction using DICTRA.....	135
Figure 6.1 (a) Sample geometries for the uni-axial tensile and pure shear tests; (b) MTS™ testing machine and details of the induction heating system.....	140
Figure 6.2 SEM images of the EA-cDSIF samples at $50 A$ , $87.5 A$ , and $100 A$ , specifying the inner and outer surfaces of the sheet, and some details of the fracture surfaces.....	142
Figure 6.3 Partially formed dimples oriented towards the outer surfaces in EA-cDSIF at $87.5 A$ and $100 A$ .....	143

	19
Figure 6.4 Fracture surfaces from heated tensile and shear tests.....	144
Figure 6.5 (a) Deformation zones in the E-DSIF process; (b) shear stress components in a small element through the thickness and detail of the dimple orientation .....	145
Figure 6.6 CT scan of the fractured EA-cDSIF 87.5 A part .....	147
Figure 6.7 Material hardness of the formed parts .....	151
Figure 6.8 <i>Ex situ</i> high-energy XRD measurements of the EA-cDSIF samples .....	152
Figure 6.9 Identification of strain values in the pulled specimen .....	154
Figure 6.10 Roughness at different true strain values in tensile tests (redline indicates the direction of profile taken for roughness measurement) .....	155
Figure 6.11 Roughness of parts formed with different toolpath strategies at room temperature	156
Figure 6.12 In-plane forces of forming the same geometry with different strategies.....	157
Figure 6.13 Specifications of: (a) Mountain Hat part; and (b) Shamrock part.....	157
Figure 6.14 Surface topography of Mountain Hat examined with SEM on: (a) internal flat region; (b) internal curved region; (c) external flat region; (d) external curved region.....	159
Figure 6.15 Surface topography of Shamrock examined with SEM on: (a) internal region; (b) external DSIF region; (c) external contact line region; (d) external SPIF region.....	160
Figure 6.16 Surface roughness of the parts formed with EA-DSIF processes .....	162
Figure 6.17 Severe damage of A2 tool steel tool after one EA-ADSIF 120 A process .....	162
Figure 6.18 Microscopic images of tungsten carbide tool (top tool): (a) as-received ( $R_a = 0.88 \mu m$ ); (b) after 3 EA-DSIF processes ( $R_a = 1.5 \mu m$ ).....	163

Figure 6.19 Microscopic images of surfaces on ADSIF formed Ti6Al4V parts .....	165
Figure 6.20 Specimen for fatigue tests (Xu et al., 2014b) .....	167
Figure 6.21 S-N curve of AA2024-T3 under cyclic tensile loading .....	168
Figure 7.1 Configuration of flexible EA vibrational surface treatment .....	178
Figure 7.2 Schematic of possible tool motions .....	178

## List of tables

Table 1 Overview comparison of technologies for low-volume production of sheet metal parts	31
Table 2 Mechanical properties of AA2024-T3 .....	38
Table 3 Experimental conditions .....	41
Table 4 Geometric deviation in different stages (unit: <i>mm</i> ) .....	67
Table 5 Comparison of hot-forming processes .....	79
Table 6 Quantified geometry of the parts formed by EA-ADSIF and EA-MDSIF .....	91
Table 7 Key findings and limitations regarding electro-thermo-mechanical deformation .....	113
Table 8 Electro-mechanical models .....	114
Table 9 Constitutive models for Ti6Al4V at elevated temperature .....	116
Table 10 Experimental specifications of EA tensile tests .....	122
Table 11 Composition of as-received Ti6Al4V determined by EDS .....	134
Table 12 Composition of $\beta$ -Ti determined by EDS .....	134
Table 13 Composition of $\alpha$ -Ti determined by EDS .....	134
Table 14 Summary of the experiments and process parameters .....	140
Table 15 Surface roughness of parts formed with different EA-DSIF processes and forming tools made of different materials .....	164
Table 16 Micro-hardness of formed AA2024-T3 samples .....	169

Table 17 Comparison of the Residual Stress (RS) measurement techniques (Kandil et al., 2001, Schajer, 2013) .....	171
Table 18 Residual stress measurement results.....	172

## **Chapter 1: Introduction**

The disparity between growing market demands and technological difficulties has caused major challenges in the area of flexible manufacturing. This thesis aims to address these challenges. This chapter introduces the background and motivation of this thesis work in detail and specifically laying out its objectives and organization.

### **1.1 Background and motivation**

Manufacturing industries have been driving economic growth and rising living standards for nearly three centuries and continue to do so in developing economies. In the fourth quarter of 2017, the gross domestic product (GDP) from manufacturing in the United States hit almost \$2 trillion (Figure 1.1) which accounts for 11% of GDP in the United States (U.S. Bureau of Economic Analysis, 2017). Manufacturing makes outsized contributions to trade, research and development (R&D), and productivity. It generates 70% of exports in major manufacturing economies and up to 90% of business R&D spending (Manyika et al., 2012). The next decade will bring substantial demand growth in manufacturing since customers are beginning to prefer more choice and customization. According to a report from the McKinsey Global Institute, the United States could boost manufacturing GDP by more than \$500 billion and climb to \$3 trillion in 2025. The biggest upside potential is found in advanced manufacturing industries, automobile industries, aerospace industries, and electronics industries (Ramaswamy et al., 2017). In these industries, sheet metal parts are fundamental components.

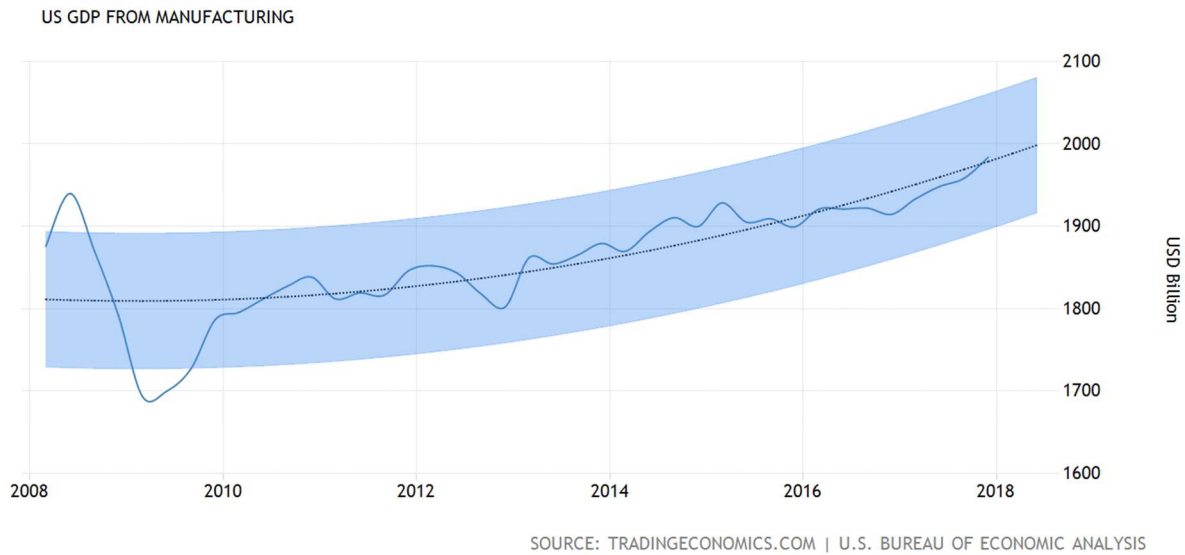


Figure 1.1 GDP from manufacturing in the United States

Rapid and customized part realization coupled with rigorous requirements on geometry and material performance have stimulated the advancement of manufacturing processes. In this context, geometry is related to the shape or dimensional tolerances a manufacturing process can achieve, while material performance is highly related to the resulting material's microstructure, mechanical properties, and surface topography. Both demands are increasingly subjected to other constraints such as shorter production time frames and increased material variety. Traditional forming processes for sheet metal parts, where an expensive and part-specific die set is required, have largely failed to fulfill the demands for cost-effective low-volume production with a short lead time. On the other hand, new flexible or die-less forming processes often failed to meet the stipulations on geometric accuracy. For instance, Incremental Sheet Forming (ISF) is a die-less forming process with several desirable characteristics, particularly for small batch production and prototyping of sheet metal parts. In ISF, a sheet of metal is securely clamped peripherally and is locally deformed by one or more generic hemispherical-ended tools moving along a pre-defined



trajectory. The accumulation of localized deformations results in the final part shape. ISF provides greater process flexibility and eliminates tooling cost while operating at a relatively low energy level, when compared to conventional sheet forming processes such as stamping (Dittrich et al., 2012). With the increasing demand for customization in manufacturing, the inherent flexibility and negligible tooling cost in incremental forming demonstrates an ideal application for low-volume, high-complexity sheet forming. However, part accuracy is still not sufficient for commercial use in most cases (Allwood et al., 2010). As another flexible process, additive manufacturing offers geometric complexity for free with most features needing to be larger than 0.5 mm (Bhushan and Caspers, 2017). It also generates defects such as porosity, lack of fusion, and dimensional inaccuracy due to distortion (DebRoy et al., 2017). Therefore, new forming processes need to be developed to resolve the conflict between process flexibility and product geometric accuracy.

Another constraint in the development of a new sheet forming process is the capability of forming various materials. Among these materials, the demands for lightweight materials are increasing in order to reduce energy consumption, relieve environmental concerns, and fulfill special material behavior stipulations. For example, titanium and its alloys have been widely used for many different applications in the aerospace and biomedical industries due to their high strength-to-weight ratio, elevated corrosion resistance and excellent biocompatibility (Ezugwu and Wang, 1997). However, these materials are usually difficult to form at room temperature.

To achieve better formability and reduced forming forces, high-temperature forming is often utilized. Reductions in stiffness and strength, and an improved plastic flow during forming are achieved due to the softening of the material upon heating (Lin and Chen, 2011). Electrically-

assisted manufacturing processes are attracting more and more attention as a result of their increased energy efficiency. The addition of the electric current passing through a metal during deformation has been observed to reduce its flow stress, increase its formability, and decrease its springback amount. It enables the process to deform materials that are difficult to form at room temperature conditions, such as titanium alloys. During the electro-mechanical deformation processes, the idea of whether athermal effects also exist apart from the inevitable Joule heating effects is currently debated by researchers. Therefore, the dominant mechanisms behind the coupled electro-thermo-mechanical loading process need an in-depth investigation.

In addition to geometric accuracy and the ability to deform materials that are hard to form at room temperature, the subsequent functional performances of the formed parts are critical criteria for evaluating a manufacturing process. The combined effect of mechanical properties of the bulk material and the surface appearance of the processed parts has a great impact on the final material performance and application. The microstructures of the processed material plays a major role in determining the macroscopic material properties of the formed parts (Olson, 2000). Therefore, to further enhance the process, an in-depth microstructural analysis is essential to study the influence of the process on its resulting material properties and performance.

## **1.2 Research objectives**

Considering the challenges of obtaining geometric accuracy, expanding process capability and enhancing material performance through the cost- and time-effective forming techniques discussed in the previous section, both engineering and scientific objectives are set in this study. Meeting the

following research objectives is central towards the development of flexible sheet forming processes. Specifically, the engineering objectives are:

- 1) to improve the final parts' geometric accuracy and the efficiency of the flexible forming process;
- 2) to realize the capability of processing materials that are difficult to form under room temperature conditions; and
- 3) to enhance the material performances of the formed parts.

The fundamental scientific objectives are set as:

- 4) to identify the dominant deformation mechanisms in electro-thermo-mechanical processes; and
- 5) to perform an in-depth study of the achieved microstructures and the resulting material properties (formability, hardness, surface topography, and fatigue).

### **1.3 Outline of the thesis**

To meet the above-stated objectives, a flexible sheet forming process is established, studied and enhanced. In the following chapters, this thesis attempts to provide experimental and theoretical insights to enhance the performance of the processed products. The outline is illustrated in Figure 1.2.

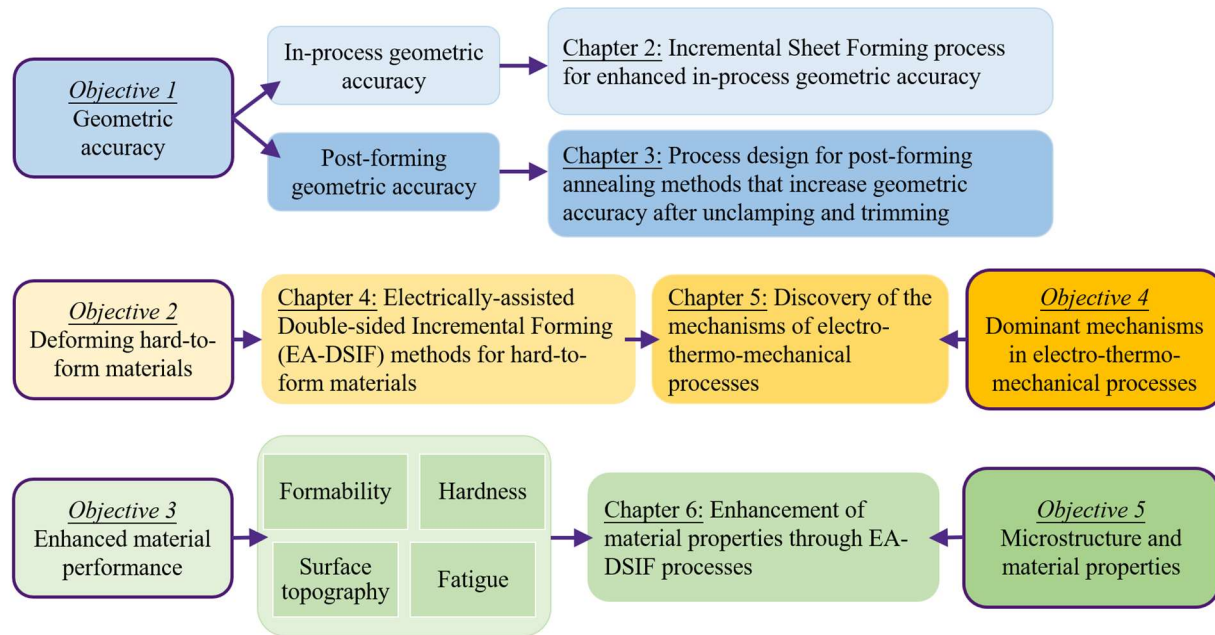


Figure 1.2 The outline of the thesis

First, the sources of geometric inaccuracy in the processed parts have been divided into two categories: in-process and post-forming geometric deviations. Chapter 2 focuses on increasing the in-process geometric accuracy while improving process efficiency. It begins with an introduction to a flexible sheet forming process called incremental sheet forming, followed by the development of a variation of the forming process to address the in-process geometric inaccuracy of the achieved parts as well as the long processing time.

Chapter 3 presents a study on increasing the post-forming geometric accuracy. It proposes and describes a novel and practical annealing methodology to reduce the springback that occurs after the formed parts are taken out from the fixtures and trimmed. The mechanisms of the post-forming stress-relief annealing process are discussed thereafter. Together, Chapter 2's focus on in-process geometric inaccuracies and Chapter 3's examination of post-forming geometric inaccuracies address Objective 1's aim of improving the flexible forming process.

Chapter 4 proposes a new flexible electro-thermo-mechanical process based on the forming process previously developed in Chapter 2. The addition of electricity provides the capability to deform materials that are hard to form at room temperature. This work is designated to fulfill Objective 2.

Chapter 5 investigates the dominant mechanisms behind the electro-thermo-mechanical process mentioned in the previous chapter. A new setup for in-situ microstructural characterization under macroscopic electro-thermo-mechanical loading is established. There are different patterns of electricity that provide similar functions. Under these patterns, an analysis is performed based on the material's macroscopic tensile behavior and microstructural evolution to meet Objective 4.

Chapter 6 studies the microstructures and the resulting material properties from the proposed electrically-assisted forming process, which includes formability, hardness, surface topography, and fatigue. First, a microstructural investigation of the fracture surface is performed to understand the fracture mechanisms of the flexible electro-thermo-mechanical forming process and the formability of the processed materials. Then, to study the competing softening and hardening effects within the process, the hardness of the processed material is evaluated. Additionally, the surface quality is examined to assess and enhance the process. Finally, the fatigue life of the processed material is analyzed based on residual stresses combined with previously measured hardness and surface topography. This work aims to meet Objective 3 and Objective 5.

Finally, Chapter 7 summarizes the entire thesis by describing the major contributions of the work and outlines ideas for future work.

## **Chapter 2: Incremental Sheet Forming (ISF) process for enhanced in-process geometric accuracy**





This chapter first introduces incremental sheet forming, a series of flexible sheet metal forming processes with many characteristics that are desirable for low-volume sheet metal production. However, it also presents a few challenges that hinder this process from mass commercialization. As discussed in the preceding chapter, one of the major challenges is limited geometric accuracy. Geometric deviations on the part occur both during the forming process, when the material is clamped, as well as after it. This chapter presents the development of a new forming process that is capable of increasing the in-process geometric accuracy while reducing processing time.

### **2.1 Literature review of Incremental Sheet Forming (ISF)**

Incremental Sheet Forming (ISF) is a relatively new die-less forming process where a sheet of material is securely clamped peripherally and is locally deformed by one or more simple hemispherical ended tools moving along a trajectory pre-defined by the designed part geometry. The accumulation of the local deformations gives the sheet its final shape. Unlike conventional sheet metal forming processes such as stamping that needs expensive dies and punches that are specific to the part shape being formed while additional dies and punches are needed when the part design changes, incremental forming uses part-shape-independent tools while maintaining a relatively low energy demand (Dittrich et al., 2012). With the increasing demand for customization in manufacturing, this inherent flexibility and negligible tooling cost make incremental forming ideal for customization in sheet forming (Ambrogio et al., 2005). Additionally, it has also been

shown that incremental forming results in substantially increased formability as compared to conventional sheet metal forming (Huang et al., 2007, Kim and Park, 2002). An overview comparison of technologies for low-volume production and rapid prototyping of sheet metal parts is shown in Table 1.

Table 1 Overview comparison of technologies for low-volume production of sheet metal parts

<u>Key Aspects</u>	<u>Die Stamping</u> 	<u>Manual Sheet Forming</u> 	<u>Machining</u> 	<u>Additive Manufacturing</u> 	<u>DSIF</u> 
Cost	High	High	High	Medium	Low
Lead Time	6-15 Weeks	6-10 Weeks	6-10 Weeks	3-5 Weeks	<1 Week
Design Flexibility	Low	High	High	High	High
Controllability	Low	High	High	High	High
Tooling Reusability	No	Yes	Yes	Yes	Yes
Accuracy	High	Low	Medium	Low	High
Experience-Based	Medium	High	Medium	Medium	Low
Automation	High	Low	High	High	High
Part Complexity	High	Medium	Low-Medium	High	High
Facility Size	Large	Small	Small	Small	Small
Thin Wall	Good	Good	Limited	Limited	Good
Production Volume	High	Low	Medium	Low	Low
Materials	Broad	Broad	Broad	Limited	Broad
Die	Fully Required	Partial Required	No	No	No
Energy Cost	High	Low	High	Medium	Low

There are different types of ISF which are introduced and compared below.

### 2.1.1 Single Point Incremental Forming (SPIF)

Single Point Incremental Forming (SPIF) is the simplest form of incremental forming in that the process only utilizes one tool to locally deform the material (Figure 2.1a). However, the geometric accuracy of SPIF is poor due to the undesirable bending that occurs in the region between the forming tool and the fixture (Jeswiet et al., 2005). Some attempts have been made to alleviate this issue. Ambrogio et al. (Ambrogio et al., 2007) attempted to optimize the parameters of SPIF to compensate for the in-process springback of a single pyramid geometry, but this method is again, geometry-specific. Time-consuming Design of Experiments methods have to be applied for every different geometry.

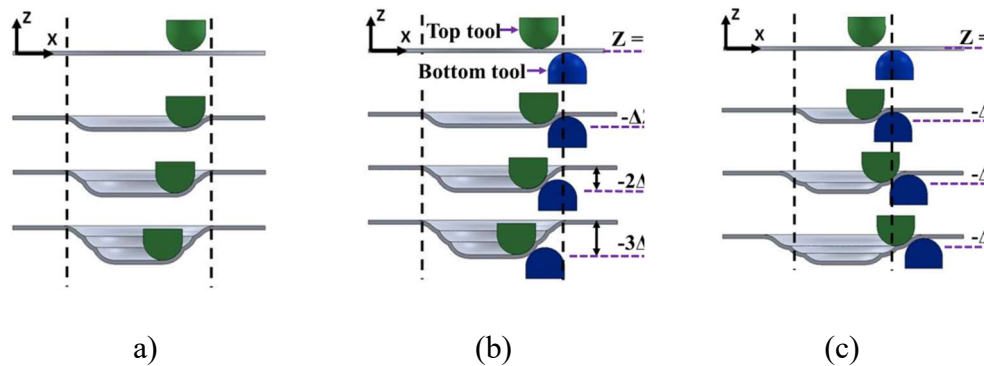


Figure 2.1 Toolpath strategies in incremental forming: (a) SPIF; (b) DSIF; (c) ADSIF (Zhang et al., 2015)

Allwood et al. (Allwood et al., 2010) tried the use of partially cut-out blanks to eliminate the deformation in the undesired regions, but concluded that a backing plate is necessary for improvement of the geometric accuracy in SPIF.

Fiorentino et al. (Fiorentino et al., 2009), Attanasio et al. (Attanasio et al., 2008), and Tekkaya et al. (Tekkaya et al., 2007) utilized supporting dies beneath the sheet during SPIF to control the



inherently poor geometric accuracy in a variant of incremental forming known as Two Point Incremental Forming (TPIF). This method can be extended towards an array of flexible support features, which ultimately leads to a die made of pins that may require an interpolation polymer-layer to smooth out the transitions between pin tips (Walczyk and Hardt, 1998). However, these approaches require some form of a bottom die, which compromises process flexibility that is a key desirable characteristic of incremental forming.

### ***2.1.2 Double-sided Incremental Forming (DSIF)***

Another variant of incremental forming, Double-Sided Incremental Forming (DSIF), adds another tool on the opposing side of the sheet that acts as a moving support tool (Maidagan et al., 2007, Meier et al., 2007, Wang et al., 2008), as shown in Figure 2.1b. This supporting tool is programmed to move along with the forming tool acting as a local die to support or squeeze the sheet, while retaining the shape-independent-tooling nature of incremental forming. Previous work by Malhotra et al. (Malhotra et al., 2011) investigated a conventional DSIF toolpath (Figure 2.1b) and found that while the geometric accuracy was improved as compared to SPIF there was a loss of contact between the supporting tool and the sheet during the forming process. This resulted in the process degenerating into SPIF and significant geometric deviations in the formed part (Malhotra et al., 2011). Additionally, we found that the loss of contact will also cause early failure of the part (Moser et al., 2016b).

### ***2.1.3 Accumulative Double-sided Incremental Forming (ADSIF)***

As an alternative, a novel toolpath strategy called Accumulative Double-Sided Incremental Forming (ADSIF) was developed by Malhotra et al. (Malhotra et al., 2012a) through changing the

nature of the toolpath used in DSIF. In conventional DSIF, the tools move from the outside of the desired geometry to the inside while travelling vertically from the top to the depth of the desired geometry (Figure 2.1b). In ADSIF the tools move from the inside of the desired part outwards without moving down in the depth direction (Figure 2.1c). The depth of the final part in each incremental deformation is achieved via accumulated rigid body motion of the already formed part of the metal sheet. Because the tools are kept within a given horizontal plane and moving outwards, the thickness does not have to be predicted *a-priori* to position the tools, thus resolving the aforementioned issue with the conventional DSIF toolpath strategy. Along with an improvement in geometric accuracy of the formed part, ADSIF also enables greater formability (Malhotra et al., 2012a) and better fatigue performance (Xu et al., 2014b). However, as shown in Figure 2.2 the use of a greater incremental depth ( $\Delta Z$ , in Figure 2.1c) causes a reduction in part accuracy. Furthermore, the forming time is inversely proportional to the incremental depth. In summary, ADSIF requires the use of a very small incremental depth in order to form a part with accurate geometry, which results in significantly increased forming time.

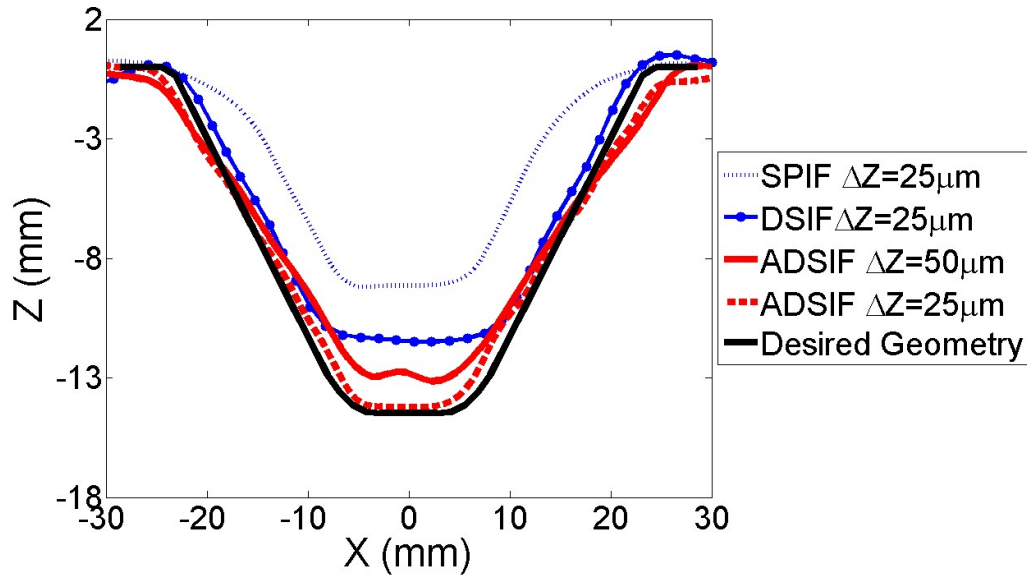


Figure 2.2 Improved geometric accuracy for a 40° cone with ADSIF and the influence of incremental depth in ADSIF on geometric accuracy (data obtained from (Malhotra et al., 2012a))

To overcome the limitations of ADSIF discussed above, a Mixed Double-Sided Incremental Forming (MDSIF) toolpath strategy to achieve higher geometric accuracy of the formed parts while reducing the forming time is developed in the following sections. The geometric accuracy of the parts formed with DSIF, ADSIF and MDSIF are evaluated experimentally in terms of the effects of incremental depth and tool positioning used. Also, the thickness profiles of these parts are acquired using a non-destructive optical detection method. The conclusions drawn from the above experiments are discussed in terms of their implications on toolpath planning. The mechanisms of this process are presented. Possibilities for future work are also discussed.

## **2.2 Mixed Double-sided Incremental Forming (MDSIF) for improved in-process geometric accuracy and efficiency**

In the MDSIF strategy, a part is first pre-formed using ADSIF with a relatively large incremental depth to ensure that the loss of contact between the supporting tool and the sheet is avoided and to reduce forming time. This ADSIF processing step acts as a rough forming pass to bring the formed part close to the desired geometry. Then, without unclamping the fixture or moving the metal sheet, DSIF is used as the second forming step on the pre-formed part to fine tune the geometric accuracy of the part.

As mentioned before, ADSIF is able to generate a part closer to the as-designed geometry than DSIF in the first step with the same incremental depth, since the global bending problem is hard to eliminate in the DSIF process without using a backing plate (Lu et al., 2015b). The forming force in the second forming step will hence be reduced due to smaller plastic deformation. Therefore, global bending and loss of contact between the tools and the sheet due to compliance will be reduced, and the geometric accuracy will be improved.

In the most general sense, DSIF can refer to any strategy utilizing two stylus-like tools to locally deform a metal sheet, as previously described. However, in this study, DSIF is used to specifically refer to conventional tool paths in which the two tools progress inward and downward to form the desired part (Figure 2.1b). This is in contrast to ADSIF (Figure 2.1c). MDSIF uses two stages of forming. For convenience, the terms A-stage and D-stage will be used to represent the ADSIF or DSIF stages in MDSIF, respectively.

### 2.2.1 Experimental setup

To experimentally examine the MDSIF strategy, a pyramidal part (Figure 2.3) with a concave pocket on each face was experimentally formed. The cross section of the desired geometry is given in Figure 2.3a and Figure 2.6. Note that this geometry cannot be generated by SPIF due to the convex-concave nature of the part. The sheet material used was 0.5 mm thick aluminum alloy AA2024-T3 which is a lightweight material that is used in aerospace applications for its high strength to weight ratio, high toughness and good resistance to stress corrosion effects (Hussain et al., 2010). The mechanical properties of the experimental material are given in Table 2. Both tools were 5 mm diameter hemispherical ended tools made of A2 tool steel. The tool speed in the experiment was fixed at 5 mm/s. The experiments were performed on a custom-built DSIF machine system (Figure 2.4) with a forming area of 250 mm × 250 mm and capable of forming parts up to 100 mm in depth on either side of the sheet (tutorial in Appendix A). The machine has a positioning accuracy to within 30 μm. No backing plate was used in the experiments which allows the incremental forming of generic part sizes and does not limit the desired flexibility of the process.

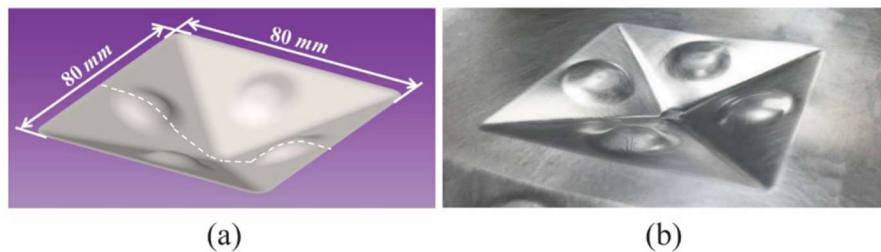


Figure 2.3 (a) CAD model of desired geometry; (b) formed part

Table 2 Mechanical properties of AA2024-T3

Density ( $kg/m^3$ )	Young's modulus ( $GPa$ )	Yield Strength ( $MPa$ )	Ultimate tensile strength ( $MPa$ )	Elongation (%)
2796	73	283	447	14

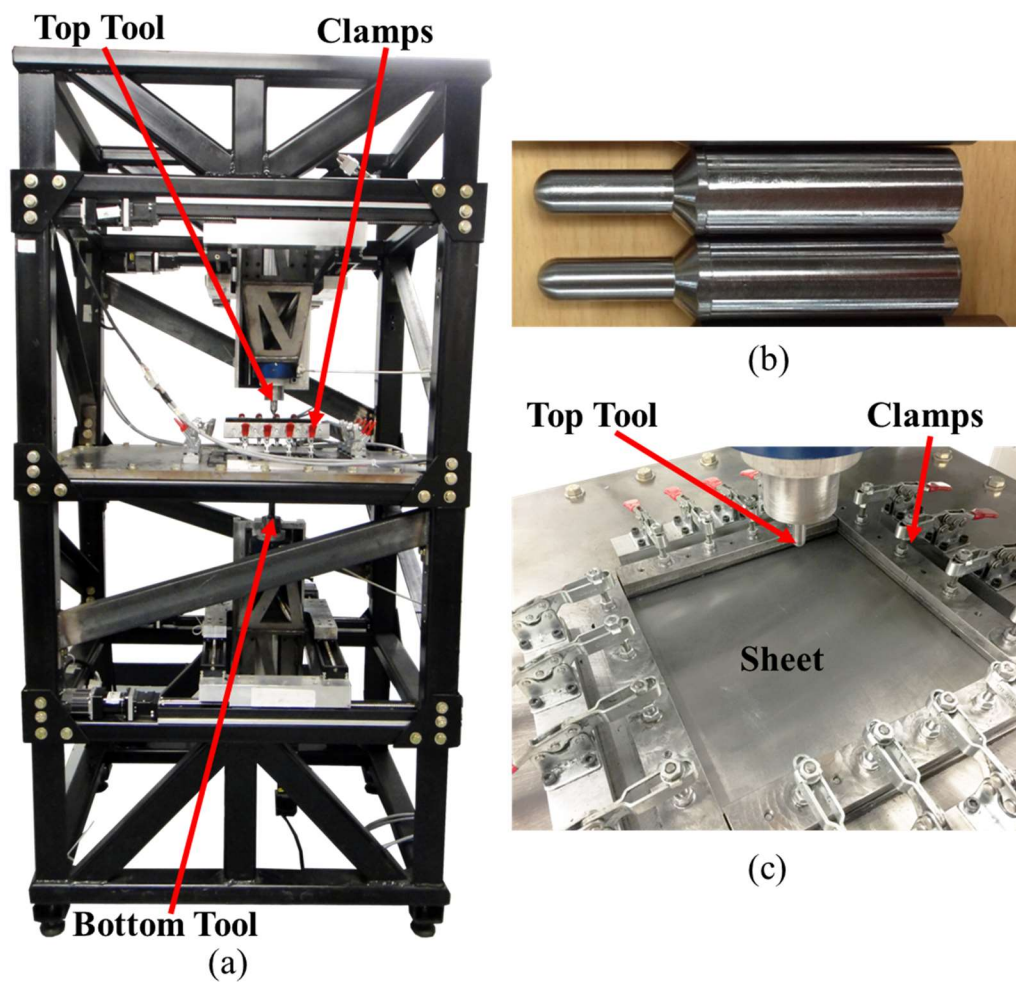


Figure 2.4 DSIF machine system: (a) DSIF machine; (b) forming tools; (c) clamping system

### 2.2.2 Toolpath parameters

The geometric accuracy of the formed parts was explored as a function of two key toolpath parameters, namely the incremental depth and the relative position of the supporting tool. In DSIF, the squeeze factor  $s$  (Figure 2.5a), indicates the magnitude of squeezing within the local area between the tools, while the surface normal is used to orient the tip of the supporting tool with respect to the forming tool, or top tool. When  $s = 1.0$ , the bottom tool is just touching the sheet and when  $s < 1.0$ , the top tool and the bottom tool are actively squeezing the sheet metal. Values of  $s = 1.0, 0.9, 0.8,$  and  $0.75$  were used in DSIF and in the D-stage of MDSIF to study the effect of sheet squeezing on the achievable geometric accuracy.

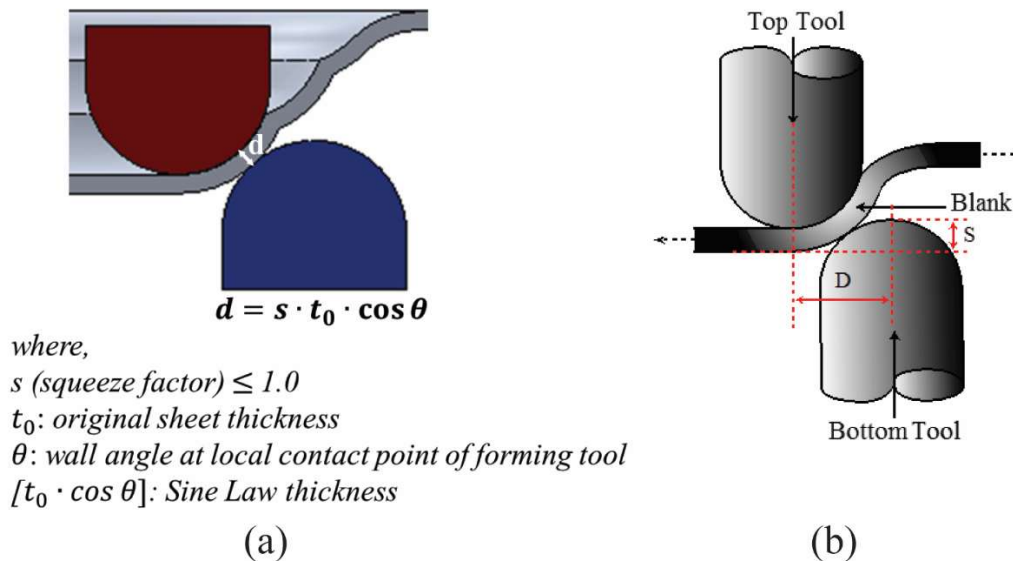


Figure 2.5 Definition of tool positioning parameters: (a) squeeze factor  $s$  in DSIF; (b)  $S$  and  $D$  in ADSIF

The position of the tools in ADSIF and A-stage was defined via two parameters  $D$  (distance between the axes of the two tools) and  $S$  (vertical distance between the bottom of the sheet and the tip of the bottom tool), which were fixed at  $2.5 \text{ mm}$  and  $0.43 \text{ mm}$ , respectively (Figure 2.5b). The

geometric accuracy of the parts formed by MDSIF were compared to that achievable with DSIF and ADSIF toolpaths using a low incremental depth of  $25 \mu m$  and a high incremental depth of  $100 \mu m$ . The  $D$  and  $S$  values for ADSIF were obtained from the previous work (Ndip-Agbor et al., 2013) since they yielded the best possible geometric accuracy. In MDSIF the same incremental depth was used for both the A-stage and D-stage. Additionally, MDSIF was also performed using an incremental depth of  $80 \mu m$ ,  $100 \mu m$ , and  $120 \mu m$ .

For all toolpaths, a spiral tool motion strategy was used since it has shown a better geometric accuracy as compared to contour toolpaths, which is illustrated by the comparison of cross-section profiles of the inner surface (Figure 2.6). The specifications of the experiments are summarized in Table 3, where  $b$  is the base time, to which every process is compared, and equals to 7 hours under the previously set forming speed of  $5 \text{ mm/s}$ .

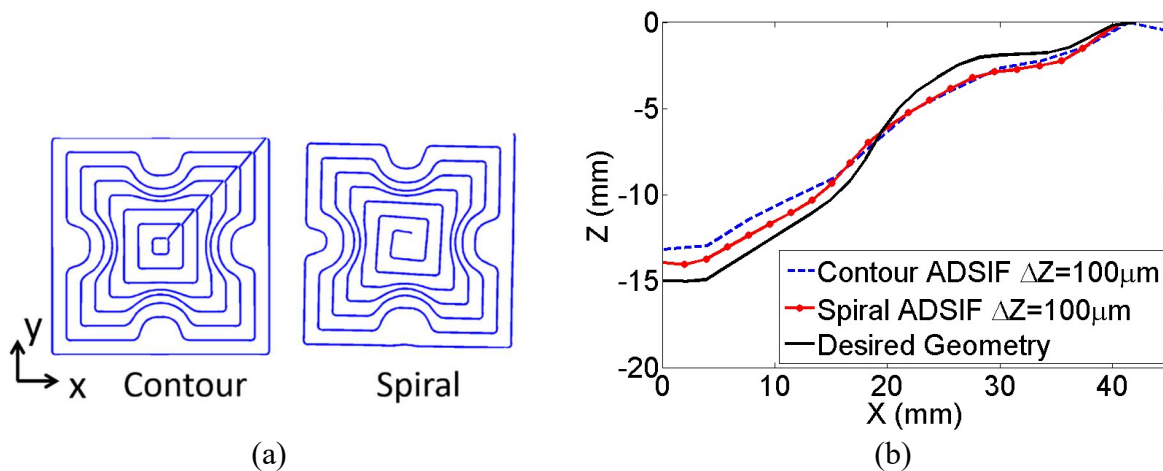


Figure 2.6 Comparison between a contour and a spiral toolpath in ADSIF: (a) toolpath; (b)

geometric accuracy



Table 3 Experimental conditions

Process		Incremental depth $\Delta Z$ ( $\mu m$ )		Forming time ( $b = 7$ hr)		Squeeze factor $s$
ADSIF		25		$b$		N/A
		100		$0.25b$		
DSIF		25		$b$		1.00, 0.90, 0.80, 0.75
		100		$0.25b$		
MDSIF	A-Stage	80	80	$0.62b$	$0.31b$	N/A
	D-Stage		80		$0.31b$	1.00, 0.90, 0.80, 0.75
MDSIF	A-Stage	100	100	$0.50b$	$0.25b$	N/A
	D-Stage		100		$0.25b$	1.00, 0.90, 0.80, 0.75
MDSIF	A-Stage	120	120	$0.42b$	$0.21b$	N/A
	D-Stage		120		$0.21b$	1.00, 0.90, 0.80, 0.75

### 2.2.3 Measurement of geometric deviations

The inner surfaces of the formed parts were scanned using a Konica Minolta laser scanner. Then, commercial software was used to generate a surface fit of the point cloud. The inner surface was chosen since it is the surface based on which the forming toolpaths are generated. The profiles were then compared to the desired geometry. In this work the geometric error was defined as the normal distance from each point on the desired geometry to the corresponding point on the formed part (Figure 2.7). Figure 2.8 shows the 3D comparison between the desired part and the formed part.

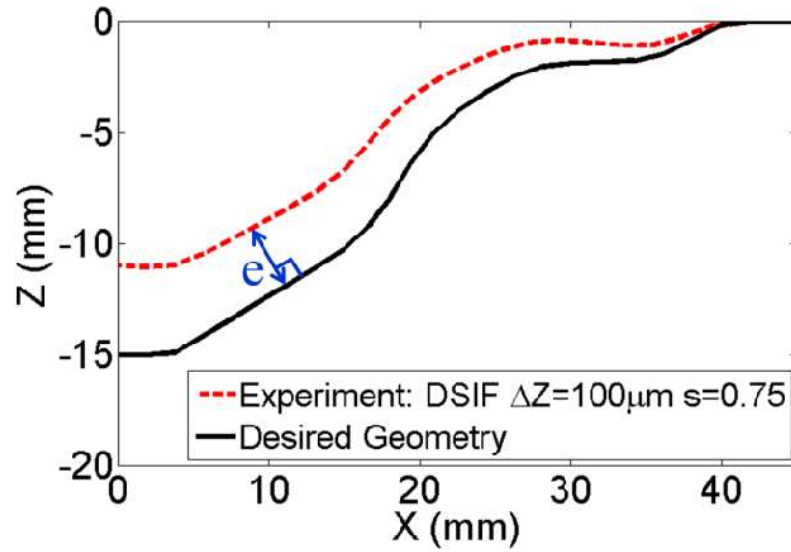


Figure 2.7 Definition of geometric error used in this work

In the current work the root mean square (RMS) value,  $E$ , of the errors along the cross section on a plane of symmetry ( $Y=0$  in Figure 2.8) will be used as a criterion to compare the deviations of the key features of the formed parts, i.e., the depth and the pocket features formed by using different strategies (Matlab code is provided in Appendix B):

$$E = \sqrt{\frac{1}{n}(e_1^2 + e_2^2 + \dots + e_n^2)} \quad \text{Eq. (1)}$$

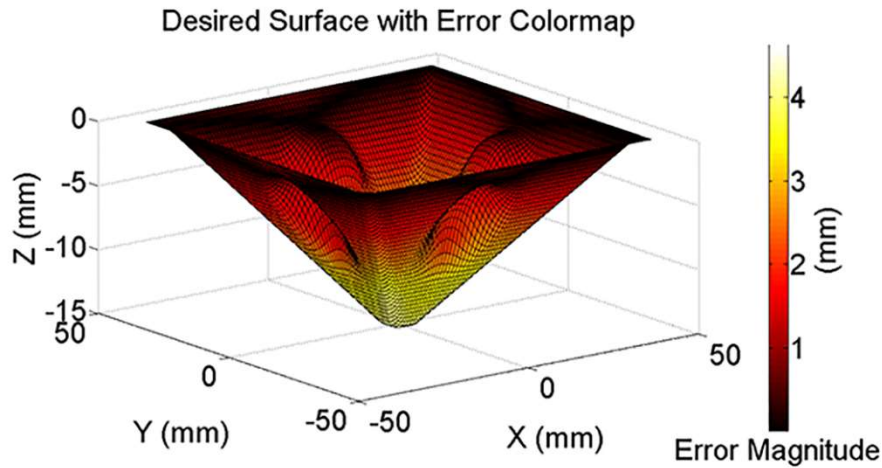


Figure 2.8 3D shape deviation contour for a part formed by DSIF  $\Delta Z=100 \mu m$ ,  $s=1.0$

## 2.3 Results

This section first discusses the influence of incremental depth and tool positioning on geometric accuracy in DSIF, ADSIF and MDSIF toolpath strategies and illustrates a special case in the MDSIF process. The thickness profiles in DSIF, ADSIF and MDSIF are discussed in the second part. Force analysis is presented at the end of this section.

### 2.3.1 Geometric accuracy

The geometric deviations of different forming strategies in terms of the RMS error, as expressed by Eq. 1, are plotted in Figure 2.9, grouped by different squeeze factors used in DSIF and D-stage. Note that in the ADSIF case, no squeeze factor was used, hence, the results of ADSIF are represented by two horizontal lines for two different incremental depths. In ADSIF, a reduction in incremental depth increases the part accuracy, as mentioned earlier in the introduction. Utilizing ADSIF with an incremental depth  $\Delta Z=25 \mu m$ , the same incremental depth that was used in our previous work to demonstrate the advantage of ADSIF (Malhotra et al., 2012a), leads to a

geometric accuracy of  $0.49 \text{ mm}$ . ADSIF with a  $\Delta Z=100 \mu\text{m}$  resulted in a geometric accuracy of  $0.88 \text{ mm}$ . These two ADSIF processes act as references to which the geometric accuracy of the DSIF and MDSIF processes are compared.

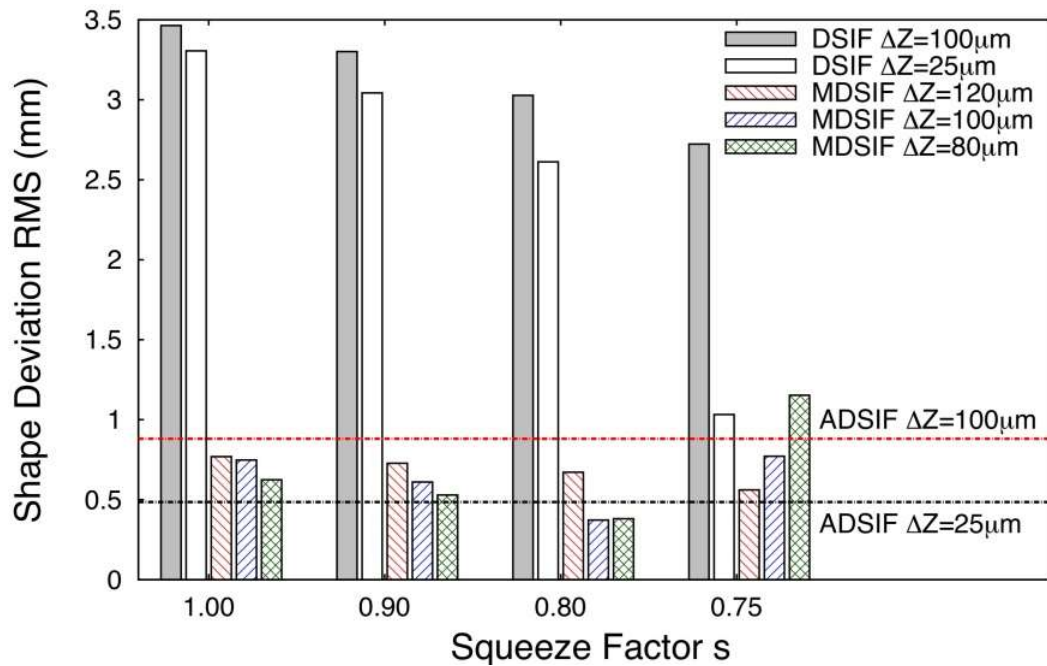


Figure 2.9 Experimentally measured geometric deviation

For DSIF, at the same value of the squeeze factor  $s$  ( $s=1.0, 0.9, 0.8$ ), smaller incremental depths ( $\Delta Z=25 \mu\text{m}$ ) result in slightly improved geometric accuracy of the formed part. The geometric accuracy is improved by 4.6% for  $s=1.0$ , 7.8% for  $s=0.9$ , and 13.7% for  $s=0.8$ . Furthermore, for a squeeze factor of  $s=0.75$ , a similar reduction in the incremental depth results in a significant improvement (62%) in the part accuracy, as compared to the same reduction in incremental depth at a large squeeze factor as mentioned before. It can be seen that in DSIF, with the decrease of the squeeze factor, the influence of the incremental depth on the improvement in geometric accuracy becomes greater. However, even for the best case in DSIF (at  $\Delta Z=25 \mu\text{m}$ ,  $s=0.75$ ) the geometric

deviation is still larger than that achieved by the pure ADSIF strategy with  $\Delta Z=100 \mu m$ , while the forming time is three times greater (Table 3).

In MDSIF, a reduction in  $s$  (from 1.0 to 0.8) at a constant incremental depth (in the  $80 \mu m$  to  $120 \mu m$  range) causes a reduction in the geometric deviation. According to the previous work of the authors (Xu et al., 2014a), with a reduction in the squeeze factor in the D-stage, the forming forces on the bottom tool are higher for a longer duration during the forming process, which mitigates the issue of loss of contact between the bottom tool and sheet. This better contact is able to ensure that the D-stage fulfills its purpose of forming the finer geometric details of the part. With the same  $s$  value ( $s=1.0, 0.9$ ) as used in the D-stage, the part accuracy increases with a reduction in incremental depth from  $120 \mu m$  to  $80 \mu m$ . In fact, for a squeeze factor of 0.8, incremental depths of  $80 \mu m$  and  $100 \mu m$  achieve similar and better accuracy respectively, than the ADSIF toolpath with an incremental depth of  $25 \mu m$ . At the same time, with an incremental depth of  $100 \mu m$  the forming time of MDSIF is reduced by 50% as compared to ADSIF performed with  $\Delta Z=25 \mu m$ . Thus, MDSIF can simultaneously reduce the forming time and the geometric deviation as compared to ADSIF and DSIF if the squeeze factor  $s$  can be properly tuned.

The depth of the DSIF formed part shows an obvious deviation from the desired depth, as shown in Figure 2.7 and Figure 2.8, highlighting the disadvantage in geometric accuracy of DSIF as compared to the ADSIF and MDSIF processes. Therefore, ADSIF can offer a pre-formed shape that is closer to the desired geometry than DSIF. DSIF, where the tools move along the desired geometry rather than staying in-plane as in ADSIF, can tune the pre-formed shape. The combination of the two toolpath strategies in MDSIF can improve the geometric accuracy.

It should, however, be noted that a special case is observed when a squeeze factor of  $s=0.75$  was used in the D-stage of MDSIF (Figure 2.9). Reducing the incremental depth reduces the geometric accuracy, which is opposite to the well-adopted understanding observed in other cases. An examination of the cross-section profiles on the inner surface of the formed geometries (Figure 2.10) shows that the final geometric features are deeper than desired, and the depth increases with the decrease of the incremental depth. This situation was never observed for other squeeze factors. In the D-stage of MDSIF, the vertical travel limit of the tools is the desired depth, however, in the current case a deeper-than-designed final part was observed in MDSIF with small squeeze factors. It is believed that due to volume conservation, additional material was pushed down when the sheet was excessively thinned by over-squeezing during the D-stage, causing an undesired downward rigid body translation of the part which is already formed in the previous stage.

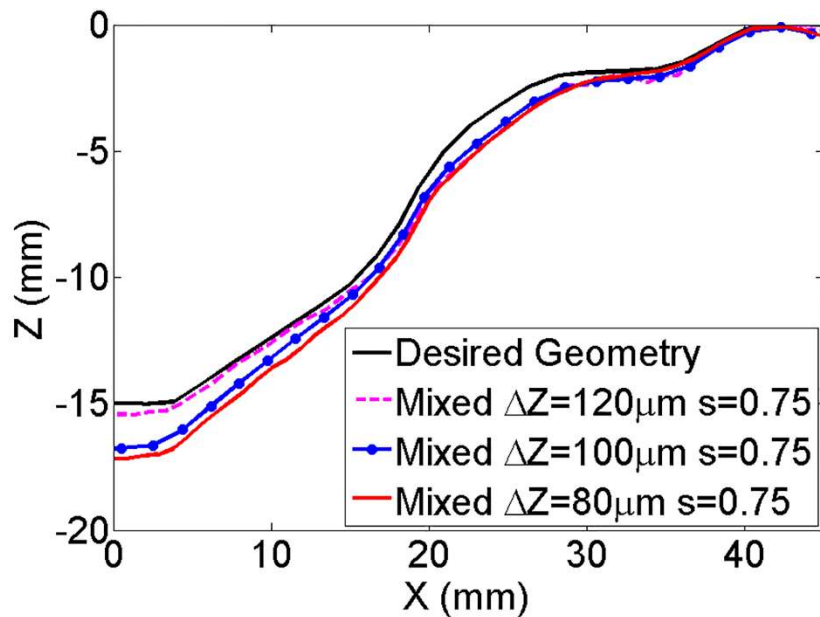


Figure 2.10 Geometries formed with a squeeze factor  $s=0.75$  with various incremental depths

### 2.3.2 Thickness profiles

To non-destructively obtain the thickness profiles over the entire parts, a Romer Absolute Arm with an integrated laser scanner was used to scan both the internal and external surfaces in a run so that they are at their actual positions in the same coordinate system to avoid the need for transferring the surfaces during data processing which may lead to extra errors. The thickness was then obtained by using the same method with calculating the geometric error as shown in Figure 2.7. This method also has the potential to reconstruct the 3D thickness map of the parts being investigated. The theoretical thickness distribution of the desired geometry predicted by the sine law (Jeswiet et al., 2005) and the thickness profiles of three different processes along the same cross section ( $Y=0$ ) are given in the Figure 2.11. The irregular oscillations of the thickness profiles are likely caused by the inaccuracy ( $30 \mu\text{m}$ ) of the laser scanner (Hexagon, 2017).

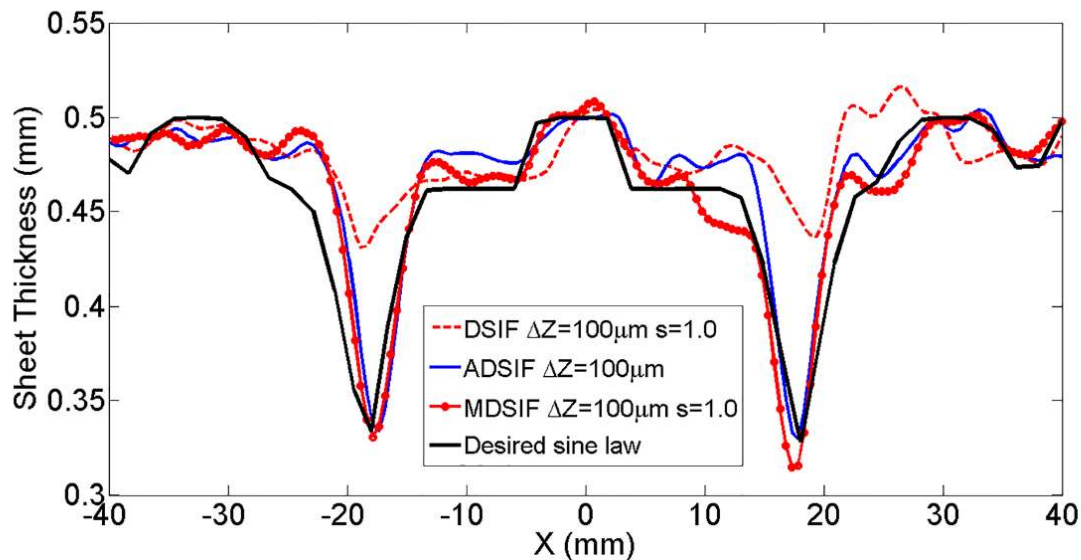


Figure 2.11 Thickness profiles along a cross section of parts formed by different processes

From Figure 2.11, the thickness profile of DSIF deviates from the theoretical calculation using the sine law. On the contrary, the sheet thickness profiles of the parts formed by ADSIF and

MDSIF processes are closer to the sine law curve. Therefore, the ADSIF and MDSIF processes (with proper squeeze factors) have a better predictability of the thickness profile. Although the advantage of MDSIF over ADSIF cannot be indicated by Figure 2.11 because of the measurement accuracy, MDSIF outperforms ADSIF in geometric accuracy as discussed in Section 2.3.1.

### ***2.3.3. Force histories***

A 6-axis load cell from JR3 was attached to each side of the tool. The force readings in the z-direction (or along the tool axis) for  $\Delta Z=100 \mu m$  during the D-stage and DSIF were compared below.

Figure 2.12 shows that with an increase in  $s$ , the forming forces on the bottom tool are higher during the D-stage. This indicates that with MDSIF the issue of loss of contact in DSIF (Figure 2.13) between the bottom tool and the sheet is mitigated. This better contact between the bottom tool and the sheet ensures that the DSIF portion of the mixed toolpath fulfills its purpose of forming the finer geometric details of the part. Moreover, when the process was close to the end, the forming forces of the top tool for  $s=1.0$  and  $s=0.9$  were higher than the forces of the bottom tool. For  $s=0.8$ , the forces on both tools were equal, while the force on the bottom tool exceeded that on the top tool for  $s=0.75$ . This indicates that a proper squeeze factor for the MDSIF process to achieve the highest geometric accuracy is one that would guarantee equal forming forces on both the top tool and bottom tool throughout the entire process. Otherwise, the material would either be under-squeezed or over-squeezed.



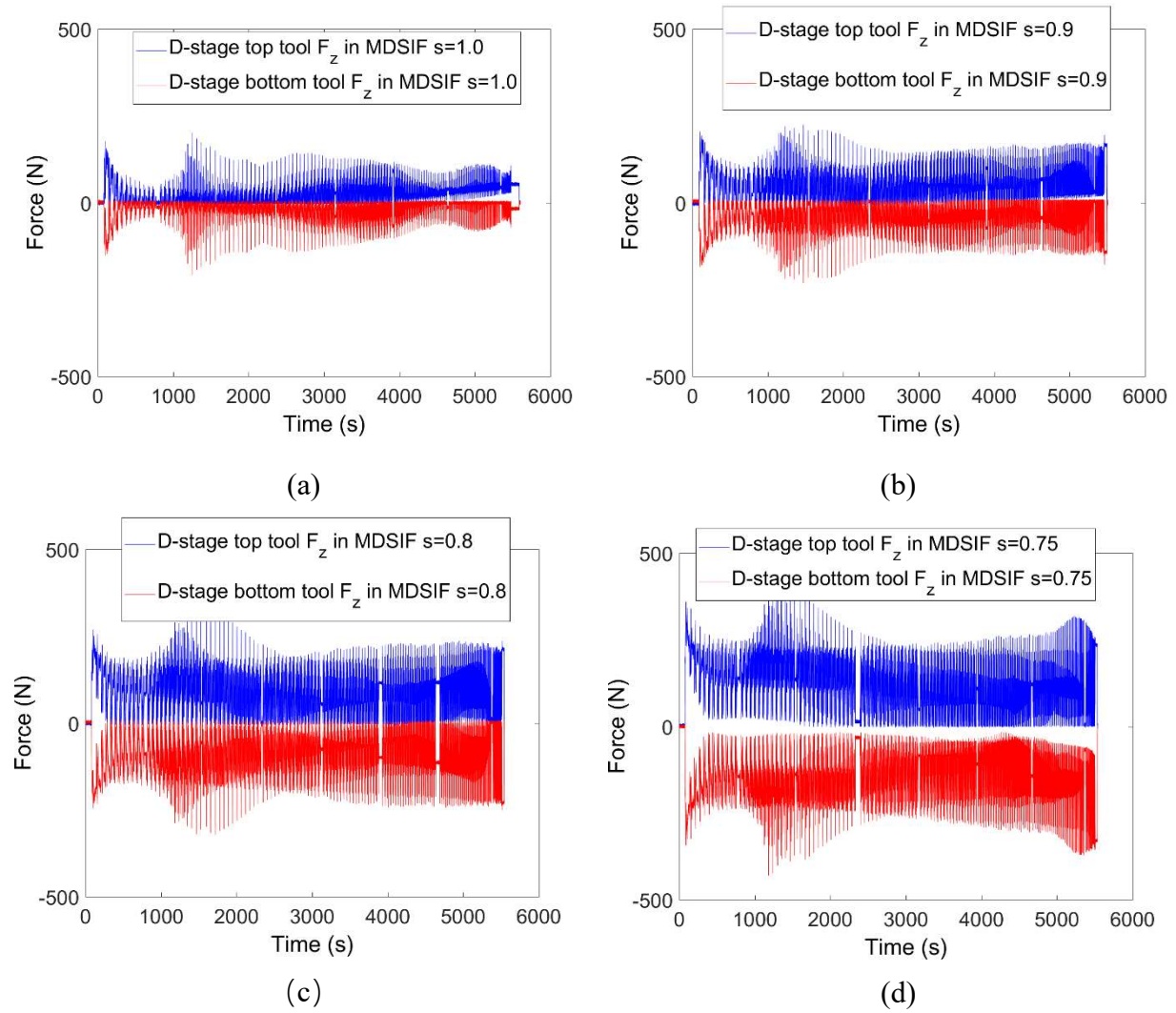


Figure 2.12 Z-direction force for  $\Delta Z=100 \mu\text{m}$  at different  $s$  in D-stage: (a)  $s=1.0$ ; (b)  $s=0.9$ ;

(c)  $s=0.8$ ; (d)  $s=0.75$

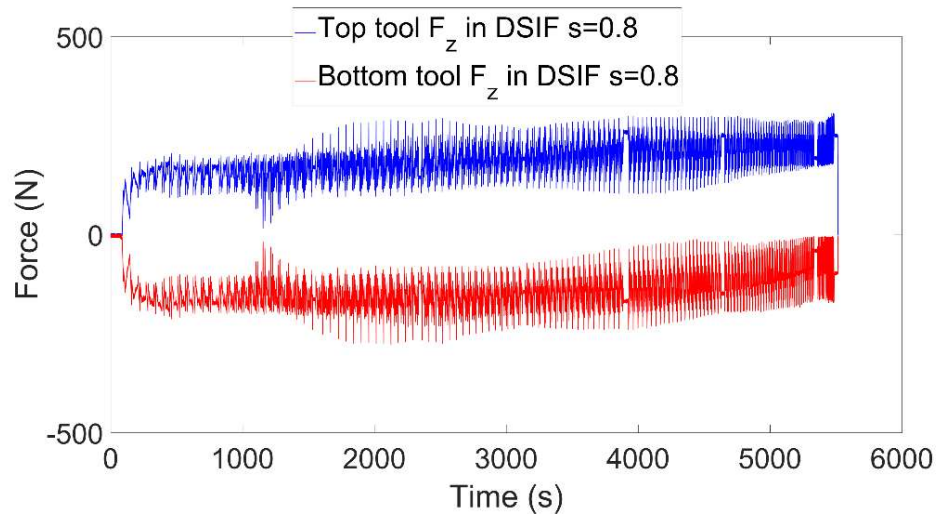


Figure 2.13 Z-direction force for  $\Delta Z=100 \mu m$  at  $s=0.8$  in DSIF

## 2.4 Summary

The MDSIF strategy, proposed in this chapter, aims to improve the in-process geometric accuracy while reducing the forming time. It has fulfilled half of Objective 1 which is to improve the final parts' geometric accuracy and the efficiency of the flexible forming process.

The performances of ADSIF, DSIF and MDSIF with different incremental depths and squeeze factors were experimentally compared. It was observed that increasing the incremental depth or the squeeze factor has negative effects on part accuracy in DSIF. Furthermore, MDSIF with  $\Delta Z = 100 \mu m$  and  $s = 0.8$  was shown to be able to attain a better geometric accuracy (with deviations under  $0.4 mm$ ) than the previous best achievable geometry that was obtained by ADSIF with  $\Delta Z = 25 \mu m$ , while reducing the forming time by 50%. Moreover, predictable thickness profiles and secured contact between the bottom tool and the sheet have been achieved.

This work has provided a novel and promising incremental forming process, which has the capability to reduce the manufacturing time as well as to improve part quality. Therefore, this new cost-effective process has great potential to increase the forming throughput yield and resolve the conflict between process flexibility and product quality.

The squeeze factors in this chapter were chosen without the consideration of machine compliance and tool deflection. Different squeeze factors may apply on different machines. Future work will take machine compliance and tool deflection into account and develop more generalized DSIF parameters and control algorithms, so that equal forming forces on both the top and bottom tools are achieved during the D-stage, which generates the best geometric accuracy as we have discovered in this work.

## **Chapter 3: Process design for post-forming annealing methods that increase geometric accuracy after unclamping and trimming processes**

The in-process geometric accuracy of the parts and the efficiency of the process have been greatly improved in the previous chapter. This chapter aims to reduce the geometric deviation occurring in the post-forming stages, including unclamping and trimming. Though existing studies in reducing the geometric deviation (i.e., the springback) in ISF have primarily targeted springback that arises before the unclamping stage, little work has been done to address springback in the post-forming stages. Therefore, this chapter proposes a practical post-forming annealing method to reduce up to 95% of the springback that occurs during the unclamping and trimming stages.

### **3.1 Literature review of springback in ISF**

One of the predominant sources of geometric inaccuracy in ISF is due to springback. The undesirable dimensional changes that occur upon removal of the clamping constraints after forming, due to the occurrence of primarily elastic recovery of the part, is generally referred to as springback (Cheng et al., 2007). In ISF, springback of the formed parts may involve the following four components (Essa and Hartley, 2011): (1) local deformation during the forming process, (2) springback after unloading the forming tool or tools, (3) global springback after releasing the formed parts from the clamping devices, and (4) springback induced by the trimming process. Here, we categorize (1) and (2) as in-process geometric deviations, while (3) and (4) are the post-forming geometric deviations.

There have been numerous investigations related to heat-assisted ISF processes to reduce global springback. For instance, Duflou et al. (Duflou et al., 2007) and Göttmann et al. (Göttmann et al., 2011) improved the geometric accuracy of formed parts by laser-assisted incremental forming, where the material was locally heated by a laser beam. Electrically-assisted ISF has shown similar capabilities for springback reduction (Ambrogio et al., 2012, Fan et al., 2010, Meier and Magnus, 2013). Ortiz et al. (Ortiz et al., 2014) heated the material globally during the incremental forming process by placing a big furnace below the entire sheet metal. Al-Obaidi et al. (Al-Obaidi et al., 2015) combined induction heating with ISF. These heat-assisted incremental forming processes exhibited reduced springback effects to some extent. However, they also required the integration of in-situ equipment, e.g., lasers or electrical currents, which increase the complexity of the process setup and control. Additionally, the introduced thermal stresses may contribute to springback after the parts are unclamped and trimmed.

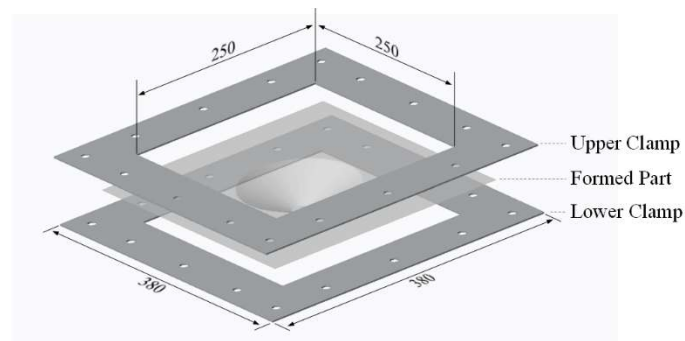
Other researchers proposed toolpath modifications to compensate for springback. Ambrogio et al. (Ambrogio et al., 2007) introduced an analytical model for truncated pyramid parts to over-deform and compensate for the in-process springback that occurred after unloading the forming tool but before removing the part from the clamps. Fu et al. (Fu et al., 2013) developed a closed-loop toolpath correction algorithm for a truncated pyramid part. A multi-stage forming strategy that reduced local springback in the final forming step compared to single-stage forming was suggested by Bambach et al. (Bambach et al., 2009). Although all these approaches have shown improvements in springback reduction, the use of toolpath modification for springback compensation still lacks robustness because of its dependence on part geometry and related residual stress distribution.

Previous investigations were primarily directed towards springback that occurred before the unclamping stage. There has been little work done to address springback after releasing the formed part from the clamps. A practical stress-relief annealing method to address springback that occurs during the post-forming stages is developed in this chapter. In the proposed method, the part is removed from the clamping system of the incremental forming machine after the forming process and placed in a portable clamping device. The part and portable clamping device are then placed into a furnace and annealed. It is worth mentioning that this proposed annealing method has the potential of being coupled with other springback reduction methods. The aforementioned methods for reducing in-process springback can be unaffectedly applied. Furthermore, the geometric accuracy of the part after trimming can significantly benefit from the stress-relief annealing as well (Bambach et al., 2009).

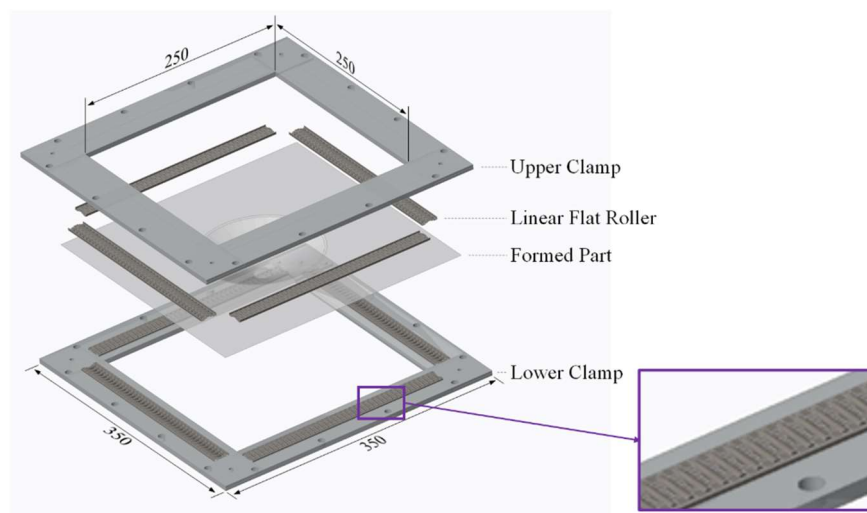
In this chapter, Section 3.2 explains the design of two clamping devices for constraining the formed part during the annealing process. Section 3.3 introduces an easy annealing parameter selection method. The performance of this annealing method on two different geometries is illustrated in the following sections. It will be shown in Section 3.4 that the springback generated during the unclamping process is considerably reduced by the proposed method. In Section 3.5, this annealing method is effectively extended to the trimming stage. The mechanisms of stress-relief annealing are discussed in Section 3.6. Conclusions drawn from the experiments and possible future works are discussed at the end in Section 3.7.

### 3.2 Design of clamping devices for annealing processes

To relieve the residual stresses that cause springback, a practical annealing process is proposed utilizing a portable clamping fixture to constrain the part geometry. Two portable clamping devices (Figure 3.1) with the same clamping area as in the incremental forming process were designed in order to maintain the part geometry as formed throughout the annealing process. Both clamps were made of low-carbon steel. The clamps and the formed parts were fixed by bolts, nuts and washers prior to the annealing process.



(a)



(b)

Figure 3.1 Clamp design for the annealing process (unit: *mm*): (a) fixed clamp; (b) roller clamp

The fixed clamp (Figure 3.1a) was designed because of its simplicity in manufacturing and serves as a good basis for comparison of other clamping designs. The thickness of the fixed clamp on each side was 2 *mm*.

During the annealing process, plastic deformation on the clamped part in the fixed clamp design is likely to be present because of the difference in thermal expansion between the clamp and the sheet metal, especially if the clamping friction is significant. To address this issue, the roller clamp (Figure 3.1b) was designed with the goal of reducing the friction between the formed part and the clamps, thereby preventing the undesirable plastic deformation of the formed parts caused by the annealing process. The thickness of the roller clamp on each side was 6 *mm*, the model of the linear flat rollers was NTN BF-3020. The rollers were assembled in the channels milled on the clamps. MoS<sub>2</sub> powder was applied to the rollers to further reduce friction.

The formed parts fixed within the clamping devices were placed into a furnace and underwent a stress-relief annealing process. The annealing parameters were determined by the method introduced in the next section. The clamped parts were then taken out from the furnace and cooled in the air until reaching room temperature with the clamps.

### **3.3 Methods for selecting the annealing parameters**

Strip bending tests were often utilized to evaluate springback under different process conditions (Wang et al., 1993, Wang et al., 2004, Yu and Johnson, 1983). To choose the annealing temperature and the corresponding annealing time for satisfactory springback reduction, a strip bending test coupled with the annealing process was established.



Strips were cut from the same batch of the material used in the aforementioned studies with dimensions given in Figure 3.2a. The strips were deformed under bending within a semi-cylindrical die by a matched round-end punch (Figure 3.2b). Both the die and the punch were made of low-carbon steel. A constant punch load of 4.9 *kN* was applied to the strips by a Carver Standard Press. The deformed strip was then clamped onto a block with the same thickness as the punch by a C-clamp (Figure 3.2c) and annealed in a preheated furnace under various annealing temperatures and annealing times, which was the soaking time at the set annealing temperature. According to the ASM Handbook (Handbook, 1991), for the material used in this study, stress-relief annealing employs temperatures up to about 345°C. Therefore, the annealing temperatures investigated in this study were 200°C, 250°C, 300°C and 350°C. Annealing times of 15 *min*, 30 *min* and 1 *hr* were performed for each annealing temperature. The annealed and clamped strips were cooled in air to ambient temperature. Each experiment was repeated three times. After the annealing processes, the strips were released from the clamps, and the strip angle  $\theta$  (Figure 3.2d) was measured via a digitized image.

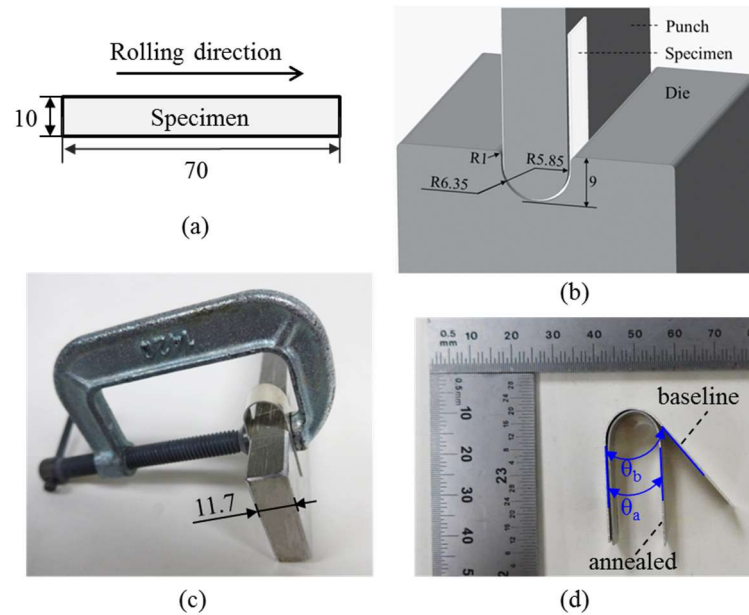


Figure 3.2 Annealing parameter selection setup (unit: *mm*): (a) specimen dimension; (b) bending test configuration; (c) clamping before the annealing process; (d) definition of strip angles

To evaluate the effectiveness of the stress-relief annealing processes on the springback reduction, a shape retention index is defined as:

$$\text{shape retention} = \frac{\theta_b - \theta_a}{\theta_b - \theta_i} \times 100\% \quad \text{Eq. (2)}$$

where  $\theta_i$  is the initial strip angle before unloading the punch, which equals to zero in this study (Figure 3.2b);  $\theta_b$  is the baseline strip angle before annealing and after completely releasing the strip from the punch and die (Figure 3.2d), which averages as  $39.9^\circ$  in this case;  $\theta_a$  is the strip angle after the annealing process and unloading the clamps, which varies with annealing temperature and time. The springback angle is  $\theta_b - \theta_i$ , or  $\theta_a - \theta_i$ . The springback angle reduction after the annealing process is then  $\theta_b - \theta_a$ . Therefore, a larger value of the shape recovery index indicates that a larger springback reduction is achieved by the annealing process.

The shape retentions under different annealing conditions are plotted in Figure 3.3, grouped by annealing temperatures. From the results, the springback reduction of the strips increases with the increase of the annealing temperature and the annealing time. In the following study, annealing temperature and annealing time pairs 250 °C and 1 *hr* (shape retention 80%), 350 °C and 1 *hr* (shape retention 99%) were selected to broaden the range of the study while achieving satisfactory springback reduction.

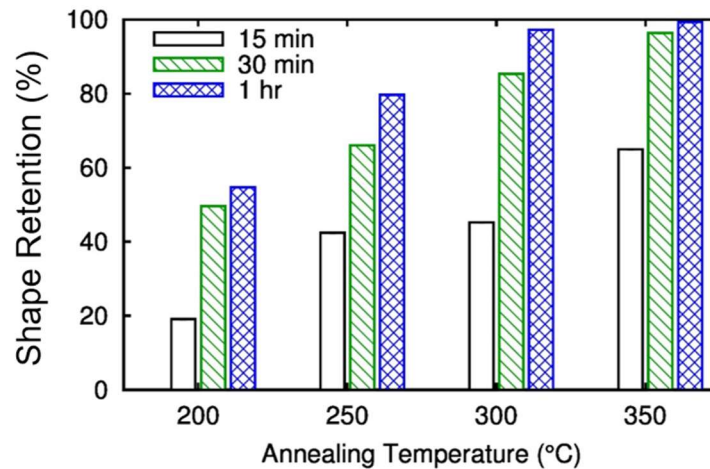


Figure 3.3 Shape retention of the strips after different annealing processes

### 3.4 Reducing springback in the unclamping process

Using the devices for constraining the geometry of the parts and the annealing parameters described in the preceding sections, the proposed post-forming annealing method is evaluated in this section. It will be shown that this new annealing method can reduce the deviations in the unclamping stage from over 5 *mm* to under 0.5 *mm*.

### 3.4.1 Experimental setup

The sheet material used in this work was  $0.5\text{ mm}$  thick aluminum alloy AA2024-T3, with its mechanical properties listed in Table 2.

The experiments were performed using the DISF machine system (Figure 2.4) at Northwestern University. A pyramidal geometry and an axisymmetric conical geometry (Figure 3.4) were designed for evaluation purposes, termed as “pyramid” and “cone” parts, respectively. The aluminum sheet material was cut to  $310\text{ mm} \times 310\text{ mm}$ , where material outside of the forming area was fully constrained by mechanical clamps. Fillets with radii of  $6\text{ mm}$  were added to the edges on both geometries.

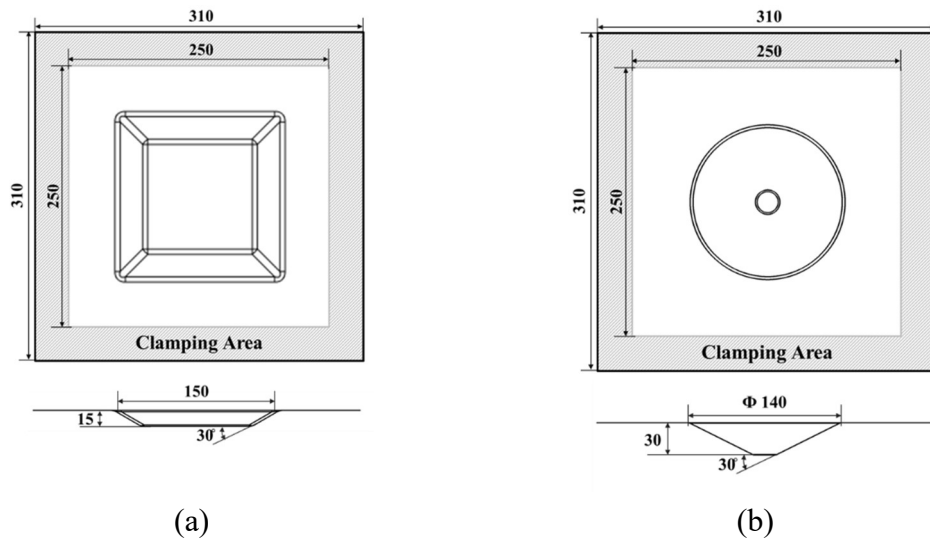


Figure 3.4 Draft of desired geometries (unit:  $mm$ ): (a) pyramid; (b) cone

The parts were formed by Single Point Incremental Forming (SPIF). In SPIF, a peripherally-clamped sheet metal is locally deformed by a single hemispherical ended tool moving along a pre-programmed toolpath. A spiral toolpath with an incremental depth, or pitch, of  $0.1\text{ mm}$  was selected to define the motion of the forming tool which was made of A2 tool steel. A tool speed and tool

diameter of 10 mm/s and 10 mm, respectively, were chosen for all SPIF experiments. No backing plate was used.

The formed parts after unclamping are shown in Figure 3.5. Undesired distortion can be observed in both the pyramid and cone parts due to springback after unclamping. This further supports the necessity of reducing the potential springback that occurs after the parts are released from the clamps.



Figure 3.5 Formed parts after releasing from the clamps: (a) pyramid; (b) cone

### ***3.4.2 Springback evaluation method for the unclamping process***

To evaluate the annealing method, springback during the unclamping process needs to be quantified. Springback was determined based on the deviations of the annealed parts from the clamped geometry. Since the part will be in different states, i.e., unclamping, reassembly, annealing, and another unclamping, during the annealing process, these conditions may result in different geometries. To differentiate between them, surface conditions were defined in the part's respective state. There are four states of the formed part in the proposed annealing process:

- 1) *Original geometry within the clamp.* The part formed by SPIF and still constrained by either the clamps on the ISF machine system or the portable clamping device is shown in Figure 4. Assuming that springback has only elastic deformation during the unclamping and re-clamping processes, the geometry of the part clamped in the machine will be

assumed to be the same as the geometry of the same part taken out from the machine and re-clamped in the portable clamp.

- 2) *Freestanding original geometry*. The clamps are removed from the formed part.
- 3) *Annealed geometry within the clamp*. The formed part has been annealed and is still fixed by the portable clamping devices.
- 4) *Freestanding annealed geometry*. The clamps are removed from the formed and annealed part.

The inner surfaces of the formed parts in Stages 1, 2 and 4 were scanned using a Romer Absolute Arm with an integrated laser scanner. Then, commercial software was used to generate a surface fit of the point cloud. In the current study, springback was evaluated by the geometric deviation of the freestanding geometry (Stage 2 or 4) from the original geometry within the clamp (Stage 1). Two geometric deviations were defined. The geometric deviation  $\Delta_{I2}$  was defined as the normal distance between each point on the geometry in Stage 1 to the corresponding point on the surface in Stage 2 (Figure 3.6a). Similarly,  $\Delta_{I4}$  represents the geometric deviation between the surface in Stage 1 and the surface in Stage 4 (Figure 3.6b).

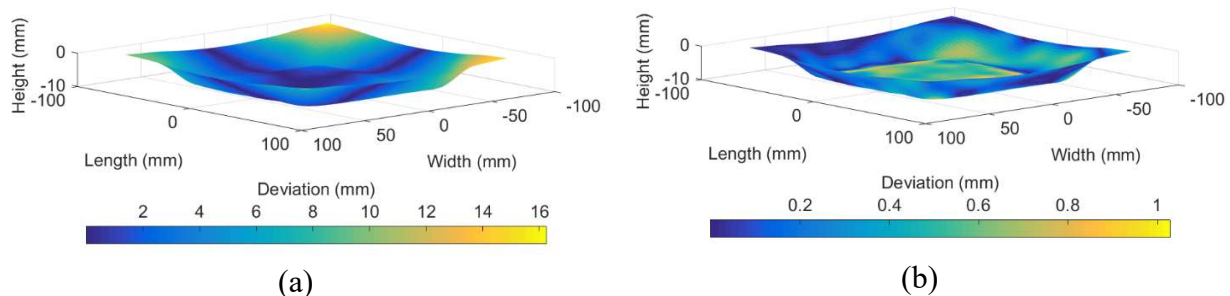


Figure 3.6 Sample 3D deviation map on the original pyramid surface within the clamp:

(a)  $\Delta_{I2}$ ; (b)  $\Delta_{I4}$

The root mean square (RMS) value of the deviations over a centered area of  $160 \text{ mm} \times 160 \text{ mm}$  was used as a criterion to compare the springback behaviors. Because two different clamping devices were utilized, the surface of the formed part in Stage 4 was compared to the surface in Stage 1 with the same clamping device.

### 3.4.3 Results

Two example photos of the freestanding annealed parts (Stage 4) are shown in Figure 3.7, which demonstrates that a significant amount of springback reduction is achieved by the proposed stress-relief annealing method when compared to the original geometries (Stage 2) given in Figure 3.4. During stress-relief annealing, the residual stresses are relieved, and this decreases the energy stored as elastic strains.

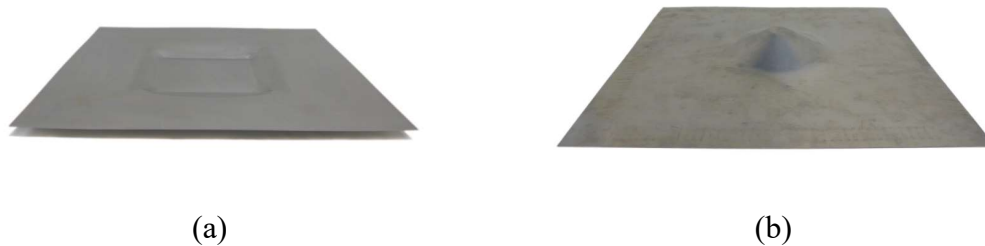


Figure 3.7 Examples of freestanding annealed parts: (a) a pyramid part annealed with the fixed clamp at  $250^\circ\text{C}$  for 1 *hr*; (b) a cone part annealed with the roller clamp at  $250^\circ\text{C}$  for 1 *hr*

The springback behaviors after the annealing process using different clamping devices in terms of the freestanding annealed geometry deviation ( $\Delta_{I4}$ ) RMS are plotted in Figure 3.8 and Figure 3.9, grouped by different annealing temperatures. The horizontal dashed line in the figure represents the deviation RMS of the freestanding original part without the annealing treatment

( $\Delta_{12}$ ). The difference between  $\Delta_{12}$  RMS and  $\Delta_{14}$  RMS demonstrates the springback reduction due to the annealing process.

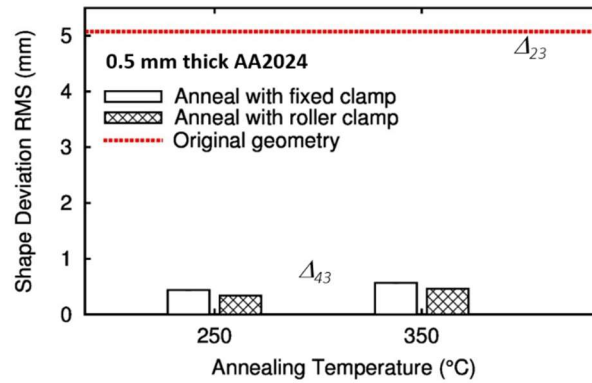


Figure 3.8 Shape deviation RMS between the freestanding pyramid part and the original part within the clamp

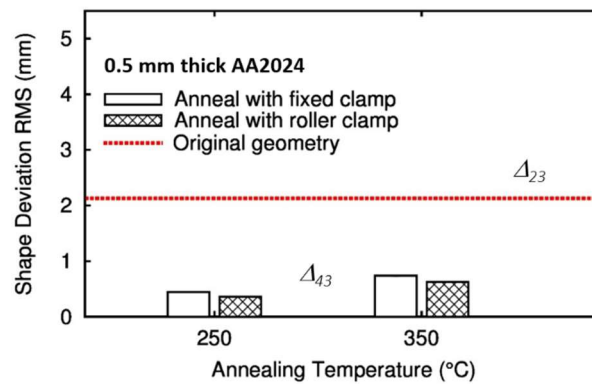


Figure 3.9 Shape deviation RMS between the freestanding cone part and the original part within the clamp

Note that significant reduction of springback was achieved in all cases by stress-relief annealing, achieving a sub-millimeter level. Springback was reduced by approximately 90% in the pyramid part and 80% in the cone part after the stress-relief annealing process (250 °C, 1 hr) using the roller clamp.



The roller clamp slightly outperformed the fixed clamp for both geometries regardless of the annealing temperature. Comparing the two dashed horizontal lines in Figure 3.8 and Figure 3.9, springback in Stage 2 was more severe in the pyramid part (5.07 mm) than the cone part (2.13 mm) due to its nonaxisymmetric nature.

It is also revealed that a high temperature of 350°C worsened the springback reduction effects. One of the possible factors is the undesired plastic deformation due to the difference in the thermal expansion between the clamp and the formed part. Material internal stresses may be generated due to the nonuniform cooling rate between regions within the clamps and the one directly exposed to the air. These effects increase with the increase of the change of the temperature. Another possible factor may be due to the softening of this material at a high temperature such as 350°C (Genevois et al., 2006) increasing the likelihood of distortion. The positive springback reduction effects of the annealing process, the predominant factor in this study, together with the negative effects determine the final shape of the part. Therefore, a future work on identifying and resolving the negative factors in the annealing process needs to be conducted to further reduce the shape deviation.

This simple annealing process is an effective method to predictably reduce springback without significant efforts requiring complex setups or using compensation algorithms. Note that the process is able to retain the geometry as it is prior to the removal of the clamps. Therefore, the enhanced in-process geometric accuracy achieved through other methods will also be preserved. Combining both in-process forming strategies for improving geometric accuracy and the annealing process provide a valid means for addressing the geometric accuracy challenge in ISF. The

integration of the clamping device with the forming machine to avoid the unclamping-and-clamping process is also possible.

It is suggested that the material of the clamping devices need to be carefully selected according to its thermal behavior and stiffness. The rolling condition of the roller clamp does provide a slightly better springback reduction, however, not significantly more. Considering the complexity in manufacturing and maintaining the roller clamp and its need for frequent maintenance, the fixed clamp design can be selected in most cases. Furthermore, this annealing method could be optimized in the future to be more energy efficient.

### **3.5 Reducing springback in the trimming process**

In some cases, the freestanding parts are not the final designed parts. They may be designed as a portion of the formed parts. Therefore, trimming may be needed after the forming process. Depending on the trim path a significant amount of springback may occur in this process. This section extends the annealing process developed in the previous section to reduce springback during trimming. The sequence of annealing steps is examined on strips that are trimmed from pyramid parts. Strips cut from the center of the pyramidal parts are selected for comparison purpose due to their large initial springback. It is suggested that the annealing process needs to be performed before the trimming process to obtain the best springback reduction.

Springback that occurs in the trimming process is often more severer and more complicated than that which occurs during the forming process or the unclamping process. The in-process deviations and the deviations from the unclamping process are summarized in Table 4. They were measured based on the evaluation method described in Section 3.4.2, using the pyramid and cone

designed in the previous section. The in-process deviation represents the geometric deviation between the surface in Stage 1 and the surface of the designed part, while the deviation in the unclamping process refers to  $\Delta_{12}$ . From the table, the amount of springback in these two processes are both in millimeters. However, the amount of deviation in the trimming stage can rise to centimeters even when a smaller pyramid was formed (Figure 3.10).

Table 4 Geometric deviation in different stages (unit: *mm*)

Deviation Source	Pyramid		Cone	
	RMS	Max	RMS	Max
Inaccuracy before the unclamping stage	5.16	8.26	2.28	4.24
Inaccuracy during the unclamping stage	5.07	16.23	2.13	4.48

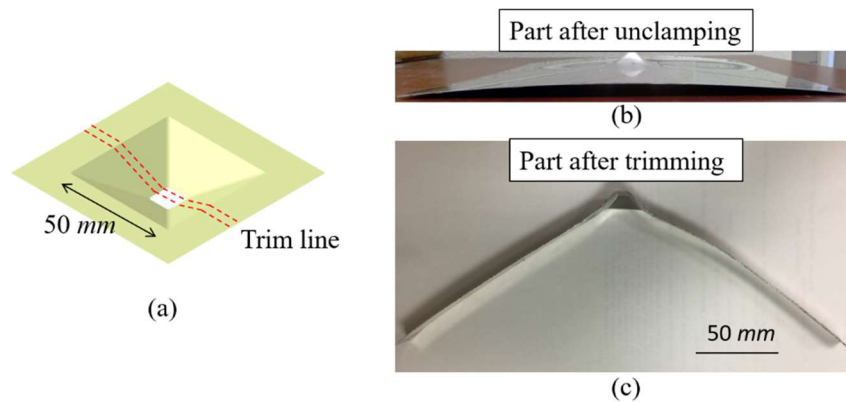


Figure 3.10 The geometry of the part from: (a) design; (b) unclamping; (c) trimming

Springback reduction in the trimming process through toolpath modification is difficult because the amounts of springback vary with the trimming path. Although previous research has shown the effectiveness of stress-relief annealing for increasing geometric accuracy in trimming

processes (Bambach et al., 2009), millimeter scale deviations still exist due to the lack of geometric constraints during the annealing process. Their work does not describe and explain the applied annealing process. Additionally, only one set of annealing parameters was examined in their work. Therefore, this section expands the annealing process proposed in the previous section towards springback reduction of the final trimmed parts. With the geometric constraints provided by the clamping system designed in Section 3.2 and the annealing parameters provided by the selection method developed in Section 3.3, a significant springback reduction (up to 95%) has been achieved in this section.

Two different methods are evaluated here based on the sequence of the annealing and trimming processes. In Method 1 (M1) the formed part undergoes the annealing process with the portable clamping system before trimming. Method 2 (M2) trims the part first, followed by the annealing process of the trimmed part which is constrained by the clamps.

### ***3.5.1 Experimental setup***

The same forming procedures and materials were utilized as described in Section 3.4.1. A small pyramid (Figure 3.10a) was used to evaluate the proposed annealing processes. A 15 mm strip was cut from the pyramid along the trim line. To better constrain the geometry during the annealing process, only the fixed clamp was utilized in this section. Annealing temperature and annealing time pairs 250°C and 1 hr, 350°C and 1 hr were selected to broaden the range of the study while achieving satisfactory springback reduction.

### 3.5.2 Springback evaluation method for the trimming process

Since the trimmed part had a small width with huge distortions, it was difficult to place the parts at a proper angle for the laser scanner to take non-destructive measurements. Therefore, a springback evaluation method similar to that described in Section 3.3 was utilized.

The shape recovery is given by Eq. 2, where  $\theta_i$  is the strip angle before the unclamping process, which equals to  $180^\circ$  in this section;  $\theta_b$  is the freestanding baseline strip angle after the trimming process but without any heat treatment, which averages  $128.3^\circ$  in this case (Figure 3.11);  $\theta_a$  is the freestanding strip angle after the annealing process, which varies with the annealing parameters and the annealing methods used. The springback angle reduction after the annealing process is  $\theta_b - \theta_a$ . Again, a larger value of the shape recovery indicates that a larger springback reduction is achieved by the annealing process. Note that the final shape is compared directly to the shape before unclamping because the annealing process has an impact on the springback that occurs in both unclamping and trimming processes.

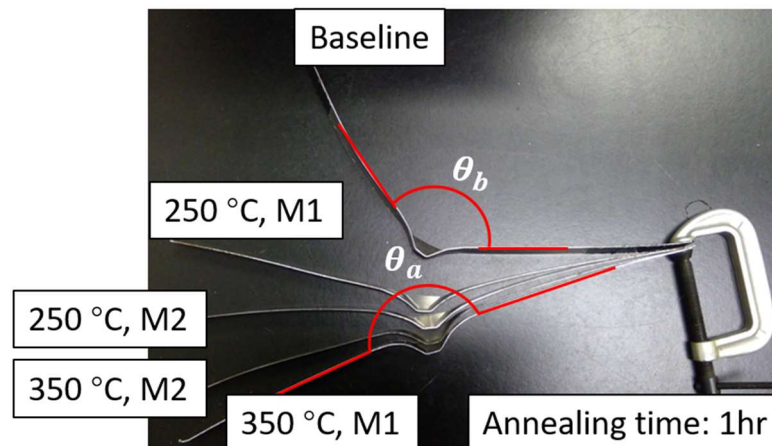


Figure 3.11 Definition of the angles utilized to evaluate the annealing processes for reducing springback after trimming processes

### ***3.5.3 Results***

The shape retentions under different annealing conditions are plotted in Figure 3.12, grouped by annealing temperatures. From the results, M1 outperforms M2 when using the same annealing temperature and time. This is because the parts have a 3D geometry. The shape is not only constrained by the peripheral clamps but also by the entire piece of the sheet metal itself. When a strip is trimmed from the formed part before the annealing process, it loses the geometric constraints provided by the surrounding material. Even when the trimmed strip is re-clamped in M2 before annealing, the shape differs from that before the initial formed part was unclamped. Therefore, to achieve an ideal springback reduction, a formed part needs to be annealed with portable clamps before the trimming process. Since the stress-relief annealing processes for reducing springback during both unclamping and trimming need to be applied right after the forming process, a single annealing process is sufficient to achieve increased geometric accuracy in both post-forming stages. When the formed part is annealed at  $350^{\circ}\text{C}$  for 1 *hr*, a 95% total springback reduction can be achieved in the trimming process. Additionally, the shape retention of the trimmed part using M1 coincides with the annealing parameter selection results derived in Section 3.3. The selection method is, therefore, proven to be practical and effective.

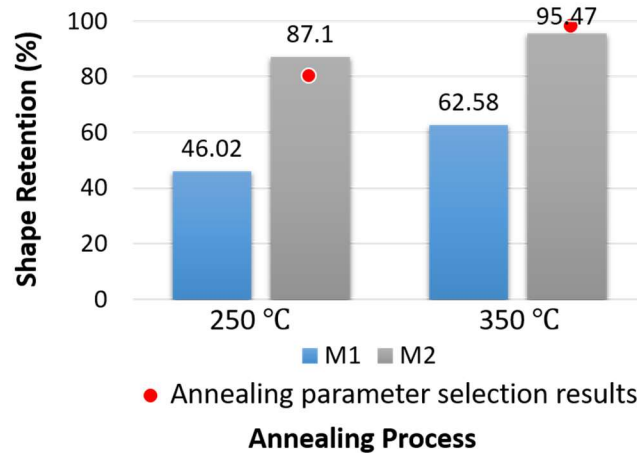


Figure 3.12 Shape retention of the trimmed parts by different annealing methods

### 3.6 Mechanisms of stress-relief annealing

This section discusses the mechanisms behind the annealing process developed in the earlier sections by first introducing residual stresses which cause springback and then the annealing mechanisms.

#### 3.6.1 Residual stresses

Springback is generally referred to as the shape change of a part that occurs upon removal of constraints after forming. It can be considered a dimensional change which happens during unloading, primarily due to the elastic recovery of the part. Springback occurs after forming, trimming and flanging due to unbalanced residual stresses in the component (Levy, 1984). The effect of springback may cause the part geometry to deviate from the designed shape. Residual stresses have a critical role in generating springback because their integral over the thickness yields a non-zero bending moment and thus a shape change (Ungar, 1960).

Residual stresses can be defined as self-equilibrating stresses which remain in a stationary solid body when no external forces are applied (Noyan and Cohen, 2013). Residual stresses can arise in materials in almost every step of processing. The origins of residual stresses in a component may be categorized as: mechanical, thermal, and chemical. Mechanically generated residual stresses are often a result of manufacturing processes that produce non-uniform plastic deformation. On a macroscopic level, thermally generated residual stresses are often the consequence of non-uniform heating or cooling operations. Coupled with the material constraints in the bulk of a large component this can lead to severe thermal gradients and the development of large internal stresses. Chemically generated stresses can be developed due to volume changes that are associated with chemical reactions, precipitation, or phase transformation (Kandil et al., 2001). In local electro-thermo-mechanical processes, non-uniform plastic deformation and heating are commonly encountered.

Residual stresses are commonly categorized as macrostresses (Type I) and microstresses (Type II and Type III). Type I stresses self-equilibrate over a length which is comparable to the macroscopic dimension of the structure or component in question. These stresses are typically the consequence of macroscopic plastic deformation or quenching of a hot sample. Type II stresses self-equilibrate over a length scale that is comparable to that of the grain structure. They are caused by differential thermal contraction. Type III stresses self-equilibrate over a length scale smaller than the grain size. They are due to coherency at interfaces and dislocation stress field (Hutchings et al., 2005).



### ***3.6.2 The recovery stage of annealing***

Annealing is heating of a metal after it has been cold worked. A small percent of the energy expended in cold work is stored in the form of elastic strain and lattice defects (dislocations and vacancies), while the rest is released as heat during deformation. Metals and alloys are in a state far from thermodynamic equilibrium in the process of plastic deformation (Kolupaeva and Semenov, 2015). In order of increasing time and temperature, there are three stages of annealing: (1) recovery, (2) recrystallization, and (3) grain growth.

The stress-relief annealing refers to the recovery stage. During recovery, enough creep occurs to reduce elastic strains. The number of point defects greatly decreases as they diffuse to edge dislocations and grain boundaries. In addition, dislocations rearrange themselves into lower configurations leading to the formation of subgrains. These result in a reduction of residual stresses, some softening, but no changes of microstructure (Hosford, 2005). This process can only reduce macrostresses (Type I stresses), while microstresses (Type II and Type III) can be reduced during recrystallization.

This section intends to utilize the recovery stage of annealing due to its effectiveness in springback reduction and the retention of the material's hardness and microstructures. With the increase of the annealing time and temperature, recrystallization will take place. In this stage, a new grain size and a new grain shape will be generated which will cause a major hardness decrease. To validate that the annealing parameters used in this section are within the recovery stage, the microstructures of the as-received and of the annealed material were measured and compared. The materials were polished and etched by the Keller's reagent. The microstructures were observed by a microscope and illustrated in Figure 3.13. From the results, the grain size and grain shape of the

annealed material are not changed compared to the as-received material. Therefore, the annealing process for increasing the post-forming geometric accuracy utilized the recovery stage of annealing.

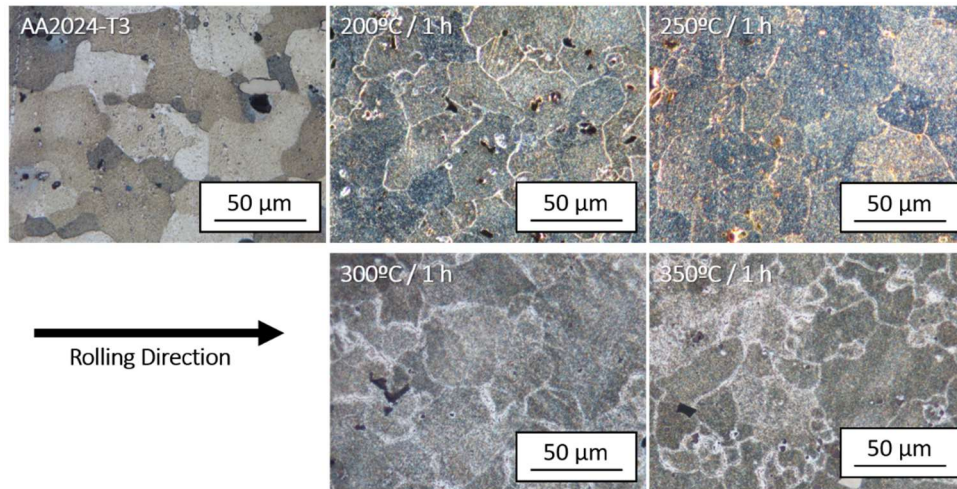


Figure 3.13 Microstructures of the as-received and annealed materials

### 3.7 Summary

A considerable amount of springback has been observed after the parts formed by ISF are released from the clamp in the forming machine and trimmed. Springback that occurs in the post-forming stages has been significantly reduced (up to 95%) after the parts were annealed under the constraint of the previously discussed portable clamping device. The proposed annealing method for reducing post-forming springback is a simple and robust method that does not require geometry-specific algorithms. It has been proven that a single stress-relief annealing process right after the forming process is sufficient for reducing springback in both post-forming stages, i.e., unclamping and trimming, regardless of a different annealing procedure for each stage. Therefore, reduced energy consumption as well as reduced processing time can be achieved through this method. The compatibility of this post-forming annealing procedure with other strategies performed before the unclamping stage preserves the improved in-process geometric accuracy from earlier stages. Future works should involve more in-depth studies of the residual stress distribution in the formed parts, which can then lead to further improvements of the annealing process.

## **Chapter 4: Electrically-assisted Double-sided Incremental Forming (EA-DSIF) methods for hard-to-form materials**

The work presented in the previous two chapters has significantly improved the geometric accuracy of the parts and the process efficiency formed by the flexible sheet forming methods. Building on these improvements, this chapter describes how DSIF, ADSIF, and MDSIF can be advanced with the capability to form a larger variety of materials, especially those that are difficult to deform at room temperature. This chapter then proposes a novel flexible electro-thermo-mechanical forming process based on the MDSIF process developed in Chapter 2, which maintains constant contact between the tools and the metal sheet to build secure electric circuits and avoid damaging electric arcs throughout the forming process. Using this method, the forming depth has been increased by 293% compared to the one formed at room temperature, and by 115% compared to the one formed with conventional electrically-assisted DSIF. A Ti6Al4V hipbone cup was successfully formed at the end.

### **4.1 Literature review of electrically-assisted (EA) manufacturing processes**

The use of lightweight materials is important for reducing energy consumption, relieving environmental concerns, and fulfilling special material behavior demands. For example, titanium and its alloys have been widely used for many different applications in the aerospace and biomedical industries due to their high strength-to-weight ratio, elevated corrosion resistance and excellent biocompatibility (Ezugwu and Wang, 1997). However, these materials are usually difficult to form at room temperature. To achieve better formability and reduced forming forces,

high-temperature forming is often utilized. Due to the softening of the material upon heating a reduction in stiffness and strength, and improved plastic flow during forming is achieved (Lin and Chen, 2011). In a typical hot stamping process (Figure 4.1), a blank is heated up in a furnace, transferred to the press and subsequently quenched in the closed tool (Karbasian and Tekkaya, 2010). A variation for forming hard-to-form materials is through superplastic forming where the metal sheet is heated and deformed at a slow strain rate (Sieniawski and Motyka, 2007). However, these processes require high investment costs associated with heat-resistant tooling and strain rate control systems.

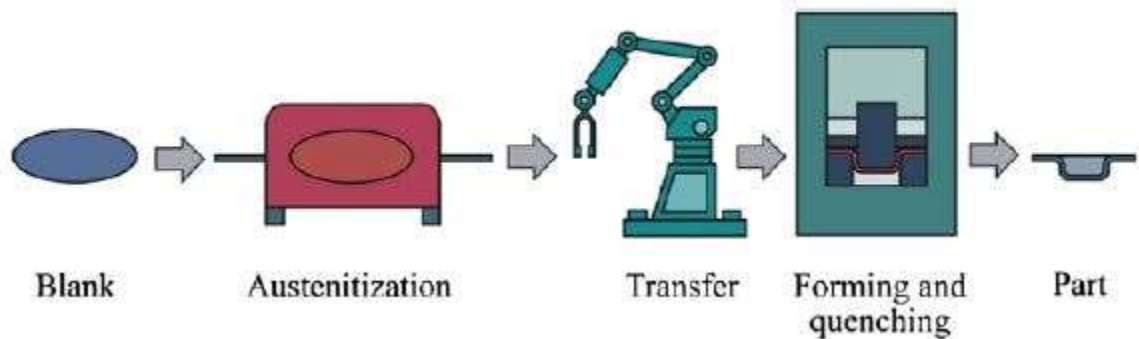


Figure 4.1 Hot stamping process chain (Karbasian and Tekkaya, 2010)

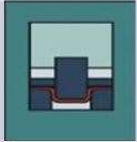
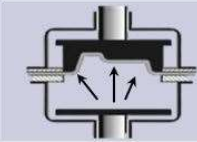

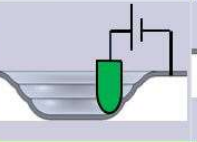
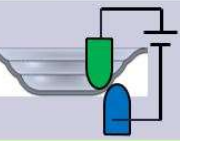
Alternative methods of heating the blanks have been established in order to address high energy losses due to the furnace and the blank transferring processes, including laser heating (Du and Hsuing, 2011), induction heating (Rudnev et al., 2008) and electric heating. The drawbacks of laser-assisted forming and induction heating are the complexity of the integration setup and the alignment procedures which limit process flexibility (Duflou et al., 2007, Karbasian and Tekkaya, 2010). Electrically-assisted (EA) forming utilizes the temperature rise caused by the Joule heating effect when a high level of continuous or pulsed electric current passes through the workpiece.

Due to the low cycle times and high energy efficiency, a few processes have been integrated with electricity, including forging (Bunget et al., 2010), friction stir welding (Santos et al., 2014), rolling (Ng et al., 2014), stamping (Mori et al., 2005), etc. Electric current pulses can further reduce the flow stress and alter overall ductility (Ye et al., 2014). They also provide evidence of the existence of athermal effects. The athermal effects of an electric current on the mechanical properties of metals under deformation are often referred to as electroplasticity. It has been reported that electroplasticity of a metal affects the recrystallization, surface hardness, ductility, strength, elongation, and residual stress. This will be discussed in Chapter 5.

Investigations related to high-temperature ISF have been performed by some researchers. Apart from the increased material formability that can be achieved through high-temperature ISF processes, reduced forming forces, reduced springback and increased geometric accuracy are also reported. For instance, Duflou et al. (Duflou et al., 2007) and Göttmann et al. (Göttmann et al., 2011) improved the geometric accuracy of formed parts by laser-assisted incremental forming, where the material was locally heated by a laser beam. Ortiz et al. (Ortiz et al., 2014) heated the material globally during the incremental forming process by placing a furnace below the sheet metal. Al-Obaidi et al. (Al-Obaidi et al., 2015) combined induction heating with the incremental sheet forming process. Electrically-assisted incremental sheet forming (EA-ISF) has shown similar capabilities for formability improvement and springback reduction (Ambrogio et al., 2012, Fan et al., 2010, Meier and Magnus, 2013). These heat-assisted incremental forming processes all exhibited increased material formability. Considering the strict alignment requirement in induction heating, or the integration of costly in-situ lasers, which may increase the complexity of the process setup and control, or the low energy efficiency of furnace heating, EA-ISF is more cost-effective,

energy-efficient, and flexible. Selective forms of hot-forming processes are listed in Table 5. Electrically-assisted double-sided incremental forming (EA-DSIF) shows great potential in low volume hot forming production as it is cost-effective, time-saving, flexible, and relatively accurate.

Table 5 Comparison of hot-forming processes

	Hot Stamping	Superplastic Forming	Laser-Assisted SPIF	Electrically-Assisted SPIF	Electrically-Assisted DSIF
					
Tooling Cost	High	High	Medium	Low	Low
Design-to-Production	8-15 weeks	8-15 weeks	< 1 week	< 1 week	< 1 week
Equipment Complexity	High	High	Medium	Low	Low
Tooling Storage	Yes	Yes	No	No	No
Part Complexity	High	High	Low	Low	High
Geometric Accuracy	High	High	Low	Low	High
Rapid Heating	No	No	Yes	Yes	Yes

Titanium and its alloys have been widely used for different applications in the aerospace and biomedical industries due to their high strength-to-weight ratio, elevated corrosion resistance and excellent biocompatibility. In particular, Ti6Al4V is the most commonly used titanium alloy for the production of biomedical implants. Current manufacturing processes for low-volume forming of Ti6Al4V, such as heat-assisted stamping and superplastic forming, require complex equipment, utilize expensive tooling, and lack local process control. EA-DSIF methods are a group of novel and hybrid ISF methods where electricity is applied to the sheet metal through the top and bottom

tools. Therefore, these methods include Electrically-assisted Accumulative Double-sided Incremental Forming (EA-ADSIF), Electrically-assisted Mixed Double-sided Incremental Forming (EA-MDSIF), and Electrically-assisted Conventional Double-sided Incremental Forming. (This chapter will refer to Electrically-assisted Conventional Double-sided Incremental Forming as EA-cDSIF to differentiate it from the category of EA-DSIF methods.)

Although EA-cDSIF has been realized to overcome the limited achievable geometric accuracy and formability (Meier and Magnus, 2013), sparks, which causes damage to the sheet and the tool, occur during the forming process due to the lack of contact between the bottom tool and the sheet metal. Loss of contact has been frequently observed in conventional DSIF, thus complicated equipment and compensation algorithm have been realized to address this issue (Moser et al., 2016b).

To advance ISF with the capability to form a larger variety of materials and to overcome the issue of the sparking phenomenon inherent to EA-cDSIF, this chapter proposes two spark-free approaches based on ADSIF technology combined with a tool-gap compensation algorithm developed to avoid loss of contact in Chapter 2. Note that in ADSIF, the tools always form virgin material. Therefore, contact between the tools and the sheet is guaranteed, which eliminates the problem of electric arcs. Specifically, the two proposed methods are EA-ADSIF and EA-MDSIF. In this chapter, a study of EA-cDSIF is first performed. The two spark-free forming methodologies are then elaborated in Section 4.3 and Section 4.4. A novel on-site EA post-forming annealing treatment is proposed in Section 4.5. Finally, discussions on the results and potential applications will be presented in Section 4.6.



## 4.2 Electrically-assisted Conventional Double-sided Incremental Forming (EA-cDSIF)

Although sparking phenomena have been reported as a major issue in EA-cDSIF that limit the process capability and affect the products' surface quality, other undiscovered problems that hinder its performance may also exist. To better understand and further improve this process, EA-cDSIF is studied in this section. It is discovered that even with secured contact in EA-cDSIF, the forming depth cannot be further improved by increased electrical current intensity. Additionally, the forming forces do not decrease with the increase in current intensity, as it would be expected. This section will reveal that apart from the sparking effects, large forming forces caused by global bending outside the forming/heating area limit the capability of deforming hard-to-form materials.

### 4.2.1 Experimental setup

To equip the conventional DSIF process with electricity, a continuous current power supplier (Dynatronix, model LFP12-300) was integrated to the DSIF machine, as depicted in Figure 4.2, creating a closed electrical circuit. The material used in this chapter was 0.5 mm thick Ti6Al4V annealed sheet. Its microstructure in the as-received condition consists of equiaxed  $\alpha + \beta$ , as shown in Figure 4.3. The metal sheets (320 mm x 320 mm) were electrically isolated from the DSIF machine with electrical tape. Two hemispherical-ended tools made of tungsten carbide (WC) with a diameter of 5 mm were used as top and bottom tools to locally deform and heat the material. The same tools acted as electrodes in the closed circuit to electrically heat the material in the tool-sheet contact region. To avoid electric arcs at the start, electricity was applied after the initial tool-sheet contact in all experiments, while polymeric parts were used to electrically isolate the DSIF machine from the circuit. The operation tutorial is provided in Appendix C.

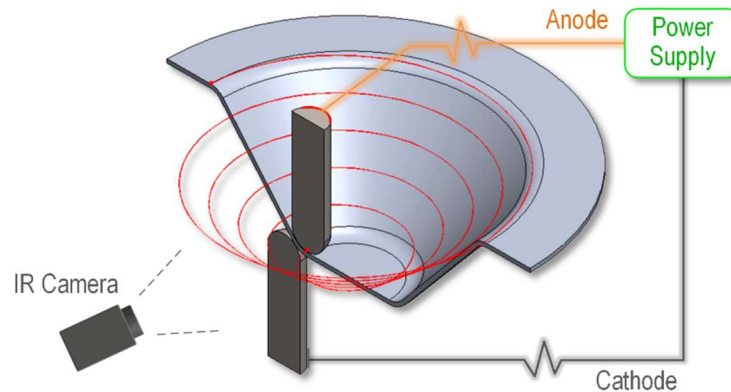


Figure 4.2 Configuration of the experimental set-up of EA-cDSIF

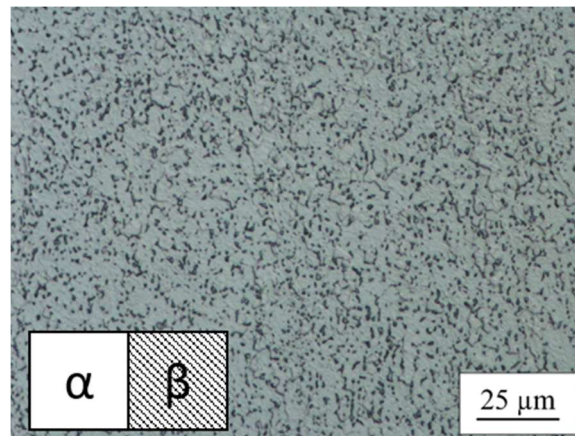


Figure 4.3 Microstructure of the as-received Ti6Al4V material

In the conventional DSIF, the squeeze factor,  $s$ , represents the magnitude of the squeeze between the tools within the local area. In this section,  $s$  was set to 0.8 because this value was able to ensure contact between the bottom tool and the sheet metal. The tools travelled along a pre-defined spiral toolpath at a speed of 10  $mm/s$ , with an incremental depth,  $\Delta Z$  (or pitch size), of 0.1  $mm$ .

To analyze how the electricity affects the material's formability, geometric accuracy, working temperature, and forming force, experiments were first carried out without electricity at room

temperature (“baseline”), and then with different current intensities, ranging from 50 *A* to 100 *A* (50 *A*, 75 *A*, 87.5 *A* and 100 *A*) in the EA-cDSIF cases.

To reduce friction and tool wear during the forming process, lubricant was utilized. When the temperature is over 500°C, liquid lubricants, such as mineral and machine oils, will decompose and do not serve the purpose well. Solid lubricants are usually employed under certain working conditions where grease and oil lubricants cannot be applied, for instance, at high or extremely low temperatures, or in high vacuum environments. Therefore, solid lubricant MoS<sub>2</sub> powder was utilized for lubrication in this chapter.

The forming temperature was measured using an infrared (IR) camera (Micro-Epsilon, model TIM160 Imager) with a temperature range from -20 °C to 900 °C. The Ti6Al4V emissivity under the testing conditions was set at 0.75 after a calibration process, which concluded in the comparison between the temperature values recorded by the IR camera and the ones measured with a K-type thermocouple placed on the sheet covered by MoS<sub>2</sub> powder.

The forming process stopped as soon as a fracture (spark) occurred. Then the formed parts were taken out from the clamps and their geometries were digitized and measured using the Romer Absolute Arm with an integrated laser scanner. The deepest position, namely the total depth of each formed part was recorded and compared to evaluate the process capability under different current intensities.

The desired geometry of the tested parts in this work was a part with a total depth of 20 *mm* and a double curvature with wall angles of 20° and 50°, respectively, as shown in Figure 4.4. The double-curvature shape was chosen because it is a characteristic of the acetabular cups used in hip replacement.

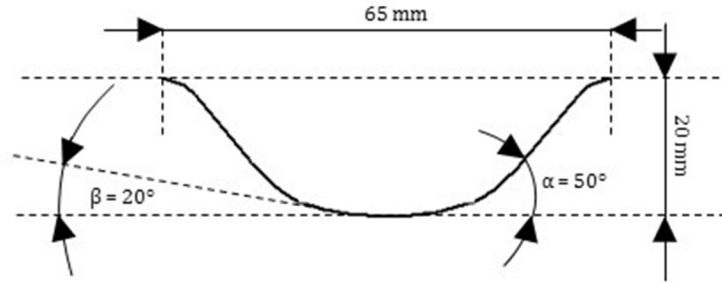


Figure 4.4 CAD drawing of the desired geometry of an acetabular cup used in hip replacement

#### 4.2.2 Results

The cross-sections of the parts formed by EA-cDSIF are plotted in Figure 4.5. From the results, the forming depth increases with the increase of the electric current. The baseline experiment fractured at the very beginning of the process. When the current intensity increased from 0 A to 87.5 A, failure occurred at a higher depth. Therefore, the addition of electricity realizes ISF with the capability to deform Ti6Al4V which is difficult to form at room temperature. However, when the current increased further from 87.5 A to 100 A, the improvement of the forming depth was slight. This was due to the large forming forces due to global bending, which will be discussed later in this section, and the stress-dependent fracture mechanisms, which will be discussed in Section 6.1. Spark occurred when fracture happened due to the cracks which deteriorate the electric circuit.

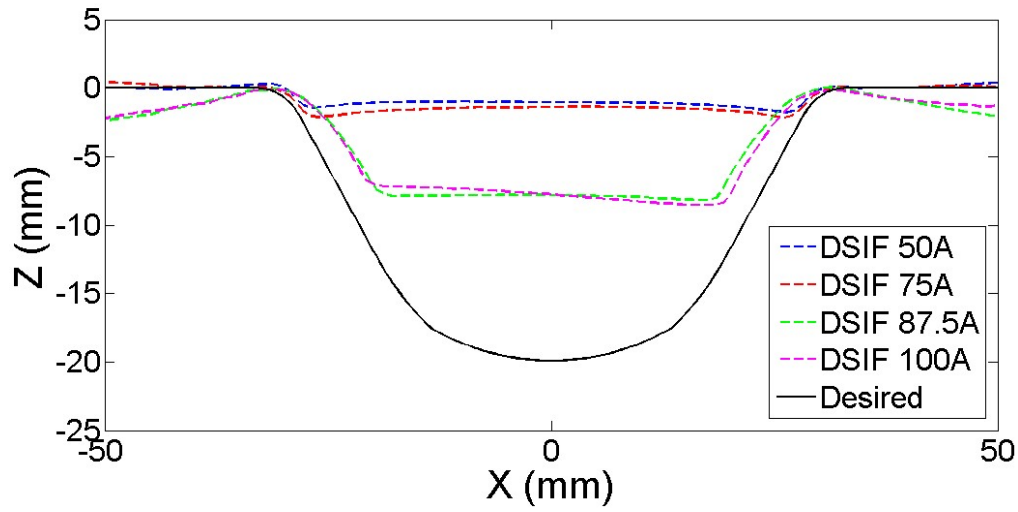


Figure 4.5 Cross-sections of the parts formed by EA-cDSIF

Since only a small area within the tool-sheet contact zone of the material is heated during the process, the closer the measurement area is to the tool tip, the higher the temperature will be and the closer the measurement temperature will be to the real forming temperature. Therefore, the forming temperature at a given moment is determined as the maximum temperature in the measurement window of the IR camera at that time frame (Figure 4.6). An example of the forming temperature history of the EA-cDSIF 87.5 A case is plotted in Figure 4.7. During the EA-cDSIF process, the forming temperature gradually increases with the forming time (or depth). This is because the tool-sheet contact area between the bottom tool and the sheet gradually decreases when the material thins during the process. The sudden temperature rise at the end of the process was due to the electric arc at the failure point. Except for the sudden temperature peak at the end, the forming temperatures of all the EA-cDSIF experiments changed gently. Therefore, the average temperature over the entire process of each current intensity case is given in Figure 4.8. From the

results, temperature increases as the electrical current increases. The maximum forming depth was achieved when the forming temperature was above 200 °C.

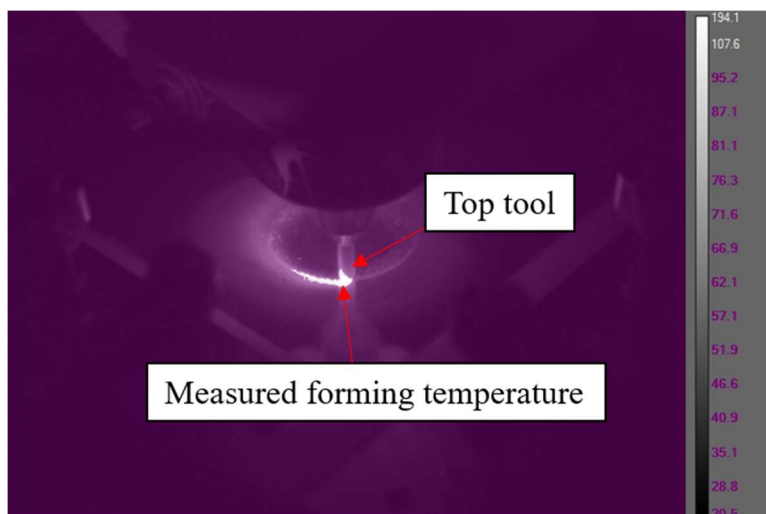


Figure 4.6 View of the IR camera during the measurement of the EA-DSIF processes

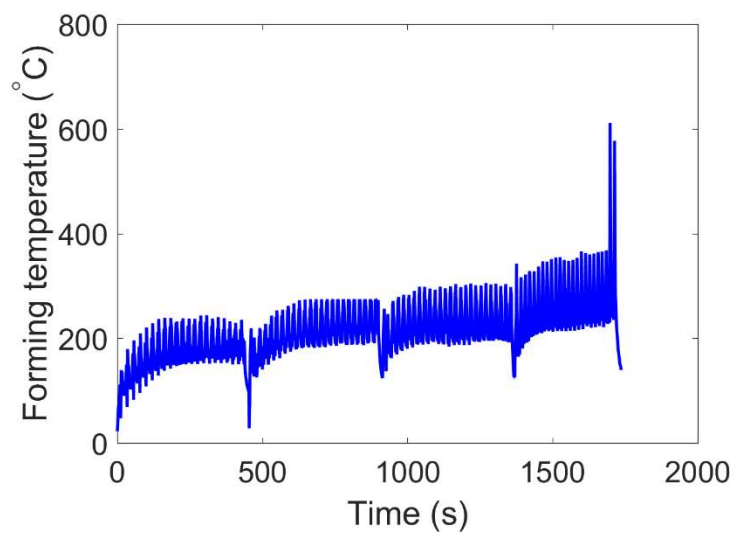


Figure 4.7 Forming temperature history of EA-cDSIF at 87.5 A

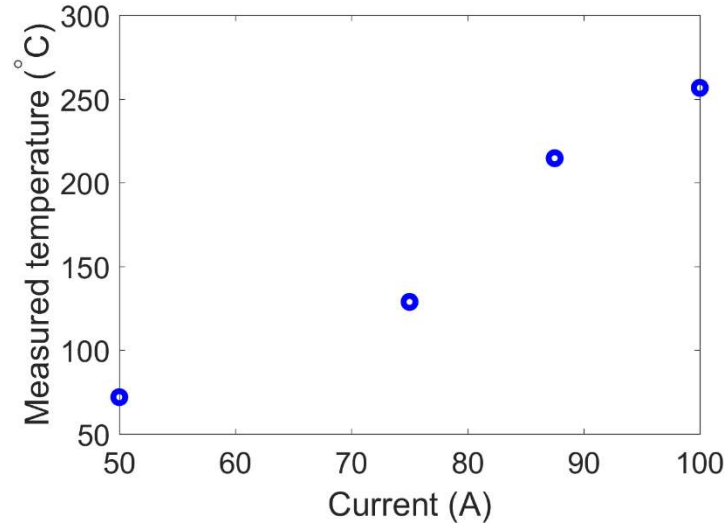


Figure 4.8 Average forming temperature measured in EA-cDSIF

The forming forces of the top and bottom tools along the x, y and z direction, named  $F_x$ ,  $F_y$  and  $F_z$  respectively, were elaborated to calculate an average resultant force for each tool by using the following equation:

$$F_T = \frac{1}{T} \int_0^T \sqrt{F_x^2 + F_y^2 + F_z^2} \cdot dt \quad \text{Eq. (3)}$$

where  $F_T$  is the average resultant forming force and  $T$  is the period of time of the forming process.

The resultant forming force history of the EA-cDSIF 87.5 A process that was measured by the attached load cells is plotted in Figure 4.9a. The force of the bottom tool decreases with the increase of the forming time due to the thinning mentioned above, which correlates well with the increase in the forming temperature. The average resultant forming forces at different currents are plotted in Figure 4.10. From the results, it is found that the average resultant forces in EA-cDSIF depend more on the forming depth than the current intensity due to global bending. It is, therefore,

concluded that besides the sparking effects, the global bending effects inherent in EA-cDSIF also hinder its capability of deforming hard-to-form materials.

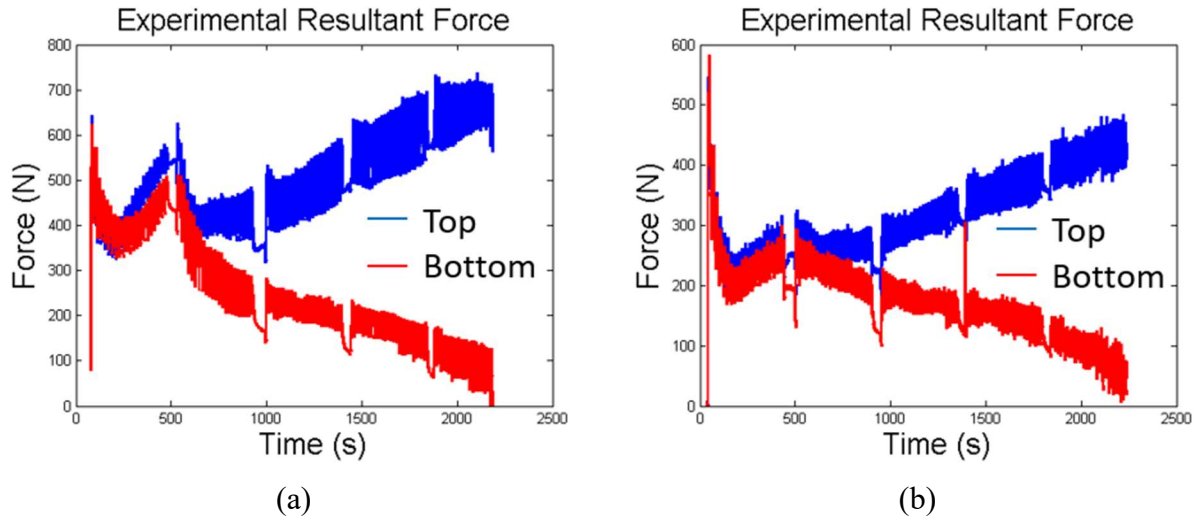


Figure 4.9 Measured resultant force histories of: (a) EA-cDSIF at 87.5 A; (b) D-stage of the EA-MDSIF at 87.5 A

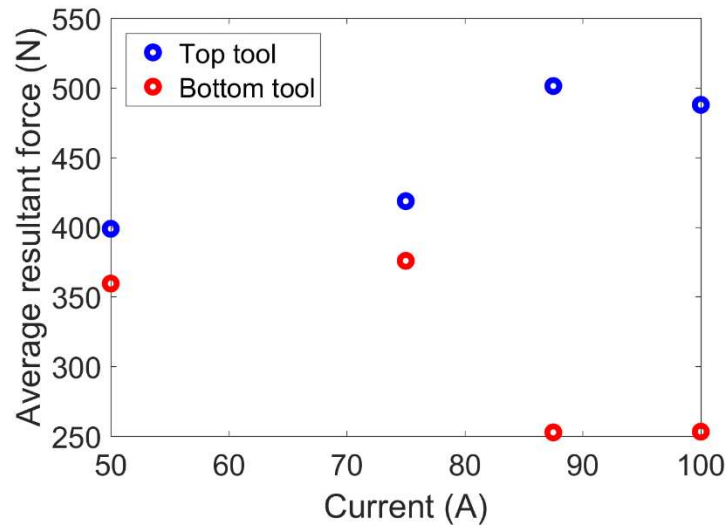


Figure 4.10 Average resultant forces measured in EA-cDSIF



### **4.3 Development of Electrically-assisted Accumulative Double-sided Incremental Forming (EA-ADSIF)**

The ability to deform hard-to-form materials has been realized by the addition of electricity. However, only a limited forming depth has been achieved by EA-cDSIF due to the large forming forces on the top tool which cannot be reduced by electricity due to the predominant global bending, as revealed in the previous section. In this section, utilizing the fact that ADSIF always deforms virgin material on the same horizontal plane at a small depth, EA-ADSIF is developed to avoid both the sparking and global bending effects. It is found that the forming force decreases as the current increases, and that the forming depth increased by 43% compared to the best achievable depth in EA-cDSIF. Additionally, to overcome difficulties associated with the measurement of the actual forming temperatures in EA-DSIF, reported by other researchers as a technical challenge due to the blockage of the view by the IR camera and the forming tools, a novel temperature measurement method and a simple temperature estimation model have been developed to facilitate future temperature control in EA processes.

#### ***4.3.1 Methodology***

The same physical experimental platform as presented in the previous section was used in this section. Two hemispherical tools made of tool steel (60 HRC) with a diameter of 5 mm were used as the top tool and bottom tool. The  $D$  and  $S$  parameters, which define the position of the bottom tool with respect to the top tool during the forming process were set at 2.5 mm and 0.43 mm, respectively, as illustrated in Figure 4.11. The tools moved along spiral toolpaths with a constant

incremental depth of 0.1 mm. The tool speed was set as 600 mm/min. The forming forces were recorded by two multi-axis load cells.

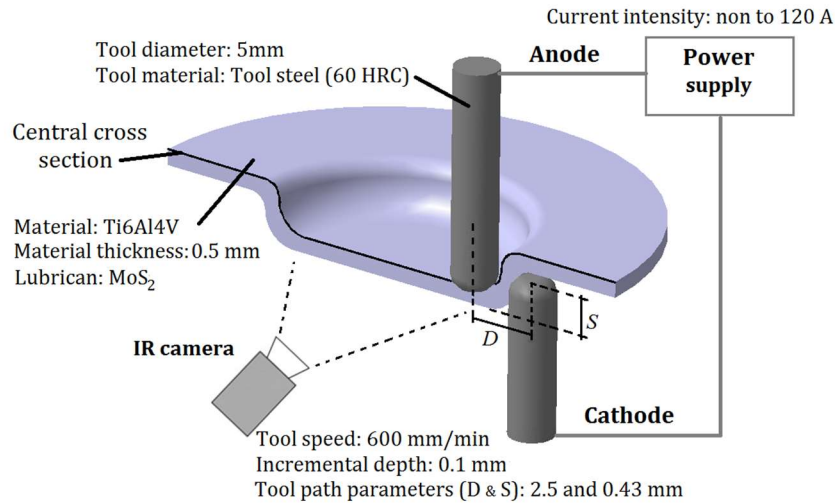


Figure 4.11 Configuration of the experimental set-up of EA-ADSIF

Baseline experiments were carried out without electricity at room temperature first, and then with different current intensities, ranging from 40 A to 120 A in the EA-ADSIF cases. To reduce friction during the forming phase, conductive MoS<sub>2</sub> powder was used as lubricant at the tool-sheet interfaces.

The geometric accuracy was evaluated by comparing the resulting geometries of the formed parts, measured with a non-contact 3D laser scanner (Minolta, model VIVID 900), with respect to the desired one.

### 4.3.2 Results

The cross-sections of the formed parts are compared with the desired one in Figure 4.12, while

Table 6 reports the values of the parameters used to characterize the geometric accuracy. It was evaluated by the resulting two wall angles, the achieved depth and the fracture occurrence. In

contrast to our expectations, the geometric accuracy did not increase linearly with the increase of the current intensity. The progressive wear of the tools, linked to the rise of temperature resulting from the increase of the current intensity, develops a negative effect on the material. Figure 4.12 shows that the best geometrical approximation, compared to the desired shape, was achieved when a current intensity of 50 A was applied in EA-ADSIF.

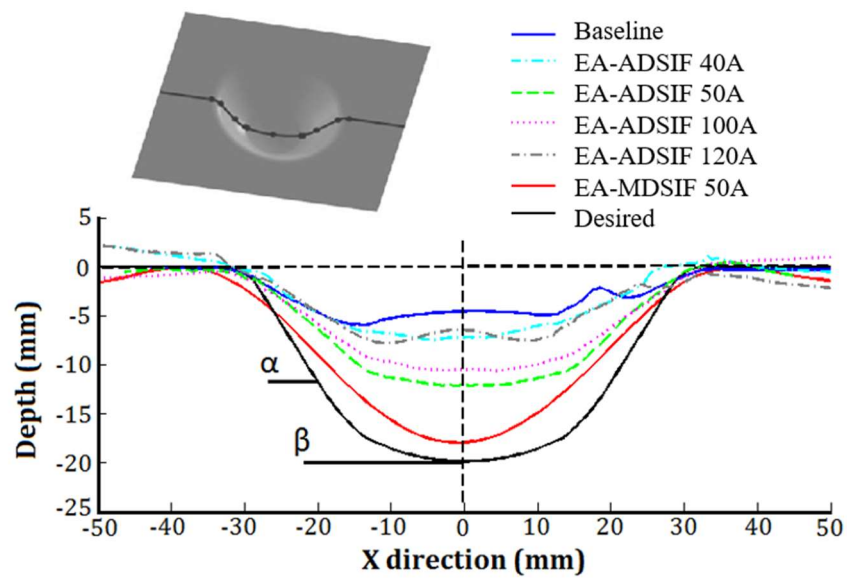


Figure 4.12 Cross-sections of the parts formed by EA-ADSIF and EA-MDSIF

Table 6 Quantified geometry of the parts formed by EA-ADSIF and EA-MDSIF

Part	I [A]	Depth [mm]	$\alpha$ [°]	$\beta$ [°]	Fracture
Desired	-	20	50	20	-
Baseline	-	4.58	20.45	-	Yes
E-ADSIF	40	7.20	24.44	3.27	Yes
	50	12.02	35.88	10.84	No
	60	7.88	19.13	2.73	No
	100	10.58	29.48	8.33	No
	120	6.48	24.72	-	Yes
E-MDSIF	50	18.02	36.80	11.9	No

The forming force histories for all the EA-ADSIF processes showed similar trends. A sample force history of EA-ADSIF performed at 100 A is plotted in Figure 4.13 to demonstrate the trend. The forming force gradually increases in the beginning, stabilizes in the middle, and decreases at the end. Note that in ADSIF, the tools start from the center and move outwards during the process. Based on the designed geometry, the wall angle increases from 0° to 20° and then to 50° in Phase A. In Phase B, the wall angle is constant at 50°. The wall angle decreases to 0° in Phase C due to the design of a fillet. Since the contact area increases with the increase of the wall angle, the forming force shows an increase at the beginning and a decrease at the end.

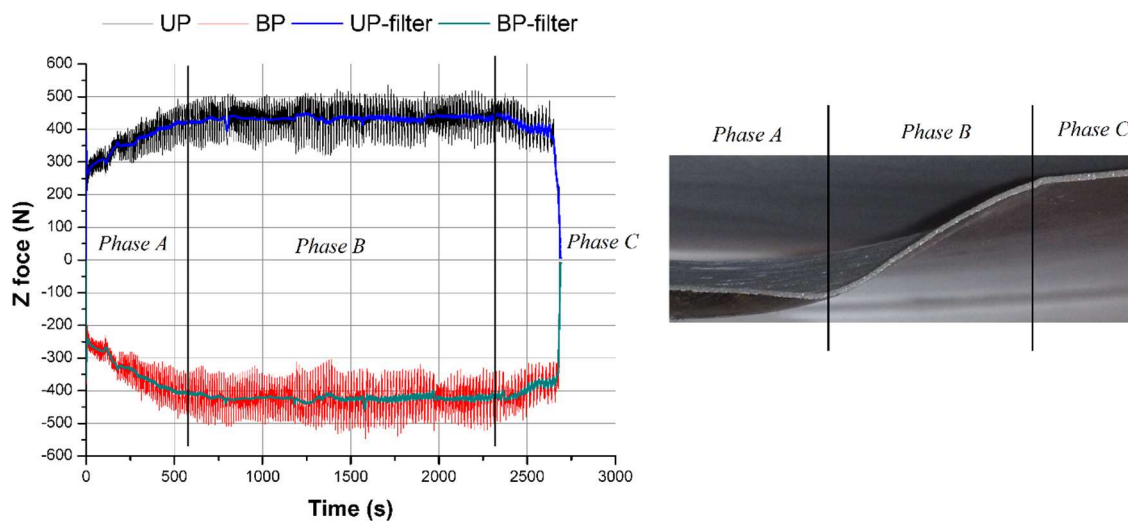


Figure 4.13 Z-direction force history in EA-ADSIF at 100 A

In order to estimate how the electricity influences the forming forces, a normalized forming force,  $F_N$ , is calculated by dividing the average resultant forming forces,  $F_T$ , of the EA-ADSIF with the ones acquired during the “baseline” experiment. The values of  $F_N$  for both the bottom and the top tool are reported in Figure 4.14. These results indicate that the EA-ADSIF process decreases the forces needed to deform the material. The maximum decrease of forming forces was

calculated when a current intensity of 100  $A$  was applied and was found equal to 14.5% of the force in the baseline test, while the minimum, namely 3%, was observed at 40  $A$ . Nevertheless, a decrease of about 8% was found when the process was assisted with 120  $A$ . Therefore, it seems that above 100  $A$  the temperature becomes a drawback for further reduction of forming forces. This could be explained by the significant wear of the tools observed due to the resulting high temperature when higher current intensities were applied. Material oxidation at that temperature value can also be a factor in the increase of the forming force.

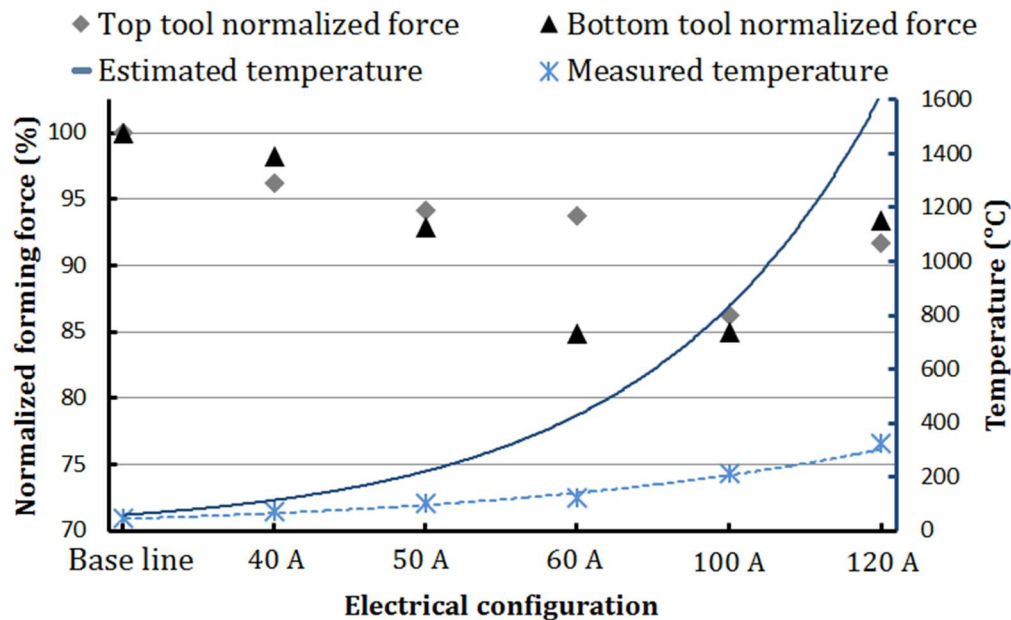


Figure 4.14 Top and bottom tool normalized resultant forces and associated measured and estimated temperatures in EA-ADSIF

The measured temperature history of the baseline test and EA-ADSIF at 100  $A$  are plotted in Figure 4.15 and Figure 4.16. Each EA-ADSIF experiments consists of 7 steps. The representative steps are plotted. Even the baseline experiments, where the tests were performed at room

temperature, reveal that there is a temperature increase due to friction. In this case, the temperature increases up to a maximum of 67 °C in the first forming step. In the following forming steps, the temperature stabilized at about 50 °C. On the other hand, when electricity is added to the process, the forming temperature decreases in the beginning and increases at the end. This is because the curvature of the formed part influences the contact area, which affects the current density and hence the forming temperature. The contact area increases with the increase of the wall angle. During the EA-ADSIF process, the wall angle increases from 0° to 20° and then to 50° in the first forming step (Phase A in Figure 4.13). In step 2 to 6 (Phase B), the wall angle is constant at 50°. The wall angle decreases to 0° in the final step (Phase C) due to the design of a fillet.

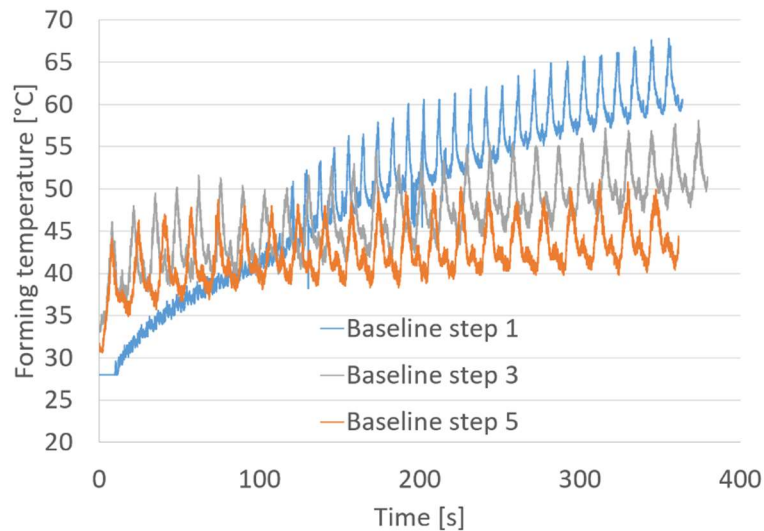


Figure 4.15 Forming temperature history of the EA-ADSIF baseline

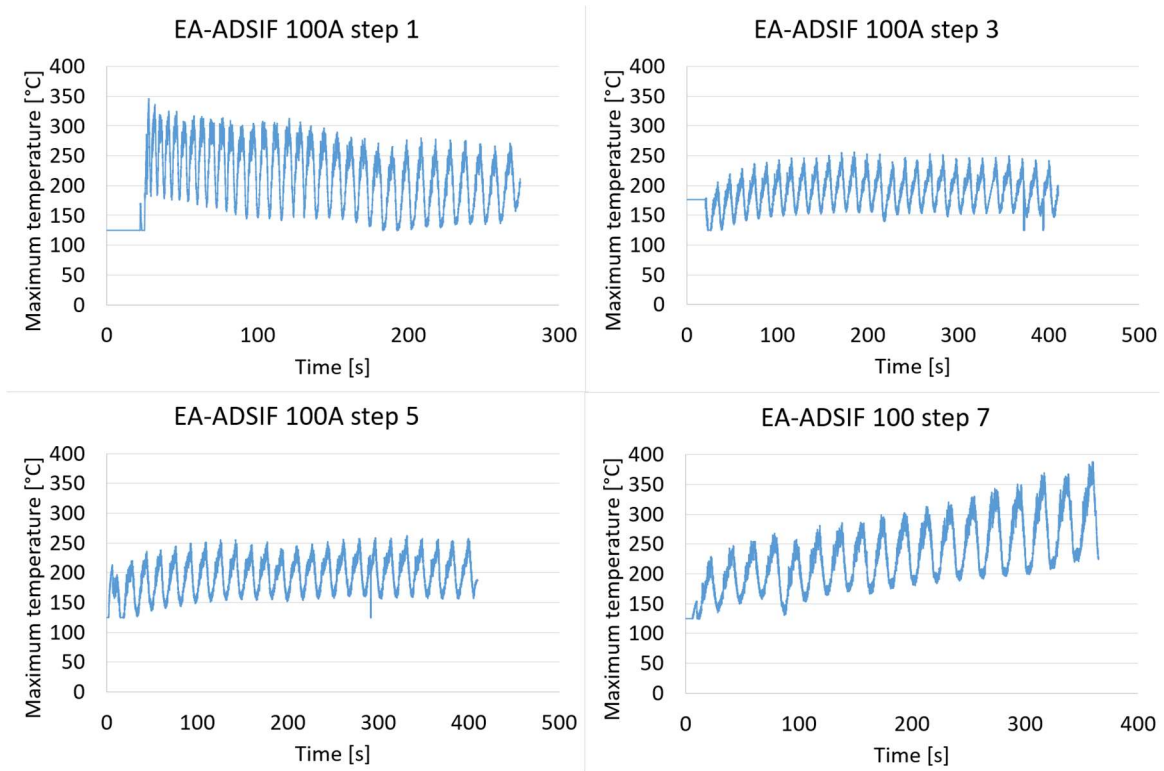


Figure 4.16 Forming temperature history of the EA-ADSIF 100 *A*

To estimate the temperature right under the sheet-tool contact area, an approach similar to the one used in (Egea et al., 2016) was applied. This instantaneous temperature was roughly estimated assuming an adiabatic condition and a circular cross section of the contact area with a radius of  $0.25 \text{ mm}$ , as determined from experimental observations. The contact area was validated by Finite Element Analysis (FEA) presented in the next section. Therefore, the instantaneous rise of temperature by the Joule effect at the sheet-tool contact is estimated to be:

$$\Delta T = (c \cdot \rho)^{-1} \cdot \gamma \cdot \left(\frac{I}{\pi \cdot r^2}\right)^2 \cdot t \quad \text{Eq. (4)}$$

where  $I$  is the current intensity,  $r$  the radius of the cross sectional area,  $t$  the time ( $0.05 \text{ s}$ , estimated from the applied tool speed),  $\gamma$  ( $1.78 \cdot 10^{-7} \Omega \text{ m}$ ),  $c$  ( $526 \text{ J/(kg}\cdot\text{°C)}$ ) and  $\rho$  ( $4.43 \cdot 10^3 \text{ kg/m}^3$ ) are

the electrical resistivity, specific heat and density, respectively. Comparing the estimated temperature and the average forming temperature measured in Phase B, as shown in Figure 4.14, for current intensities lower than 60 A, the estimated and measured temperatures have the same order of magnitude. However, at 100 A, the order of magnitude of the estimated temperature is roughly 10 times higher than the measured value. Although heat loss was not considered in the temperature estimation, the difference would not be 10 times more. Therefore, it is clear that the temperature at the sheet-tool contact area is much higher than the measured values of the surroundings (Ambrogio et al., 2013). A new method for determining the actual forming temperature is presented in the next section.

#### ***4.3.3 Determination of the actual forming temperature***

To determine the actual forming temperature in the tool-sheet contact area which is not measurable by the IR camera, a qualitative comparison between the sheet colours was applied, identifying the chromatic analogies between the samples deformed in the EA-ADSIF and tensile experiments, as reported in Figure 4.17. The tensile tests were performed using a universal 5t MTS™ testing machine, housed at the University of Padova, which was equipped with an induction heating system shown in Figure 6.1b. During the tests, the samples were heated up to the testing temperature, which was controlled through a K-type thermocouple spot-welded on their central area, and, after a soaking time of 30 s, they were strained at a constant temperature of the gauge area. After the tensile tests, the fractured samples were left to cool in calm air. From the temperature histories of EA-DSIF (Figure 4.7) and EA-ADSIF (Figure 4.16), the temperatures oscillate in the range of 100 °C. Therefore, heated tensile tests were performed every 100 °C starting from 100 °C to 900 °C. The amperage equal to 50 A was related to 200 °C since none of



the samples presented any colour differences as compared to the as-received condition; on the other hand, the amperage equal to 87.5 A, where a brown colour with few light blue hints was found on the sheet because of the higher temperature, was linked to 600 °C. Finally, the amperage of 100 A was associated with the highest temperature, 800 °C, in both cases, the sheet was brown with a wide blue area. The results are plotted in Figure 4.18.



Figure 4.17 Color comparison between the samples obtained from the tensile and EA-ADSIF tests. The red box represents the area heated by the induction heating system during the tensile tests.

Estimated temperatures are calculated based on Eq. (4). Figure 4.18 demonstrates the estimated temperatures calculated with different contact area ranging from  $0.2 \text{ mm}^2$ , which is the observed contact area, and  $0.24 \text{ mm}^2$  which is the simulated contact area (Figure 4.19). The simulation model was established in ABAQUS using the explicit integration method with sub-modeling technology. The simulation was carried out in collaboration with Huaqing Ren. In the global model, the sheet ( $250 \times 250 \times 0.5$ , units:  $\text{mm}$ ) was modeled by 5-layer solid elements with reduced integration to accurately capture the bending and compression mechanics. The top tool and the bottom tool, whose diameters are  $5 \text{ mm}$ , are modeled using rigid shell elements. In total, the model contains

320,000 elements. The mass scaling method is used and the tool speed is increased from  $5 \text{ mm/s}$  used in experiments to  $750 \text{ mm/s}$  in the simulations to speed up the simulation process. Artificial damping was added to eliminate the dynamic effect since ADSIF is a quasi-static process. It was assumed in this context that the contact area does not depend on the material, hence, AA5754-O was used in the simulations. The sheet material, aluminum alloy AA5754-O, was modeled by the von-Mises yield criterion and the voce hardening law. After completion of the global simulation, the boundary condition was retrieved and imposed on a sub model, which was essentially a section cut from the global model. In this setup, the sub model size was  $5.0 \times 5.0 \times 0.5 \text{ mm}^3$ , with a  $0.05 \text{ mm}$  element size with 100,000 solid elements. The same mass scaling, tool speed, and material properties were applied in the submodel. The global simulation was finished within 24 hours while the fine-meshed submodel simulation was also finished within 48 hours.

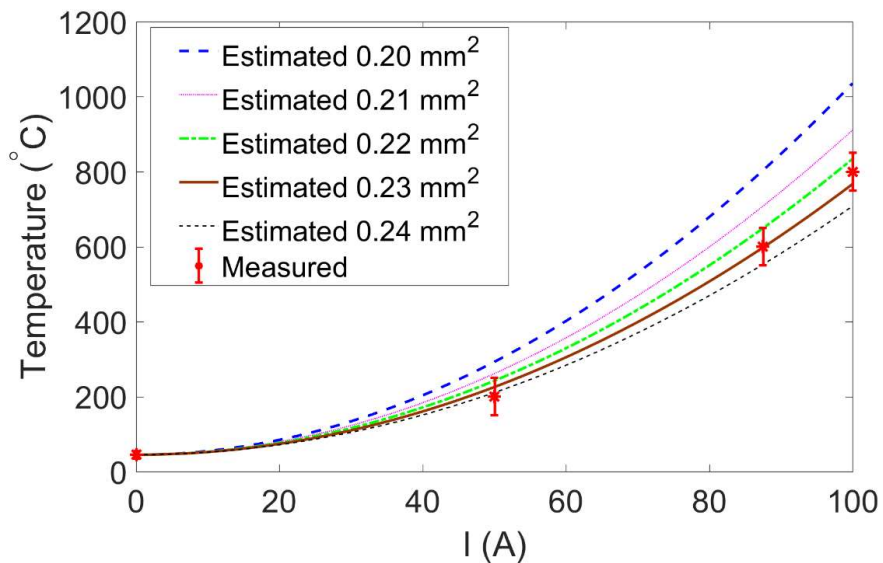


Figure 4.18 Measured temperature via color comparison and estimated temperature using different contact areas

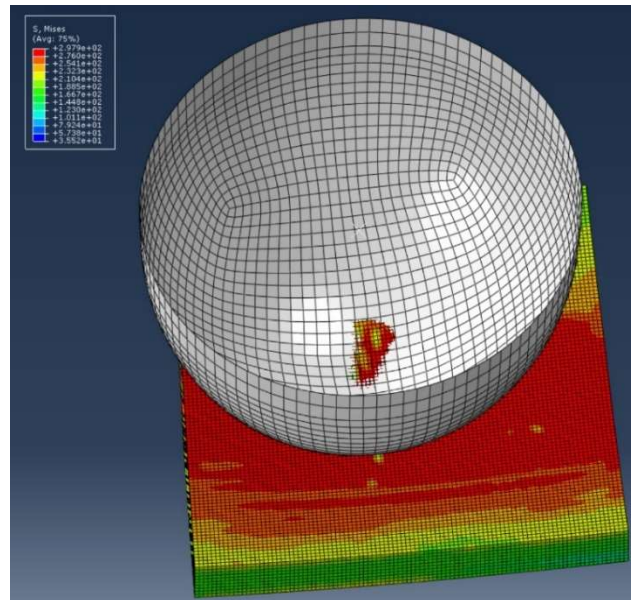


Figure 4.19 Contact area calculated through FEA simulation

Comparing the estimated with the measured temperatures, the actual forming temperature is much closer to the estimated temperature than the forming temperature measured with the IR camera. The contact area can also be estimated to be  $0.21 \text{ mm}^2$  to  $0.24 \text{ mm}^2$ . Therefore, this new temperature determination method is an effective way to measure the actual forming temperature for the EA-DSIF processes.

#### 4.4 Development of Electrically-assisted Mixed Double-sided Incremental Forming (EA-MDSIF)

Although fracture has been postponed and even eliminated in EA-ADSIF with a 43% increase in forming depth (Section 4.3) compared to the best achievable depth in the EA-cDSIF process, a limited forming depth and geometric accuracy was still generated due to the indirect control of the geometry by the tools. Additionally, it was discovered in Section 4.2 that electrical current has a limited effect on reducing forming forces in EA-cDSIF. Given that the forming force reduces in

the D-stage compared to DSIF, as discussed in Chapter 2, and that DSIF has a direct control on geometry, EA-cDSIF is proposed to act as the second forming pass after EA-ADSIF to fine-tune the geometry and further increase the forming depth. Therefore, EA-MDSIF is developed in this section. This work was carried out in collaboration with Beatrice Valoppi from University of Padova and Antonio J. Sánchez Egea from Universitat Politècnica de Catalunya. Using the EA-MDSIF method, it will be shown that a better forming depth than in EA-cDSIF can be achieved. Furthermore, several additional desirable material properties achieved through this method, will be presented in Chapter 6.

#### ***4.4.1 Experimental setup***

The basic idea of the hybrid EA-MDSIF is performing EA-ADSIF followed by EA-DSIF, joining the material deformation mechanisms and the advantages of the two opposite toolpath strategies (ADISF and DSIF), which is similar to the development of MDSIF in Chapter 2. The physical platform and the process parameters were the same as in the previous section. The EA-MDSIF process was performed using 50 *A* for both the A-stage and D-stage, which was the electrical current value that resulted in the best geometric accuracy among the EA-ADSIF cases.

Besides the confirmation of the electricity's effect on the increase of the material's formability and decrease of forming forces, the research shows that, compared to the EADSIF process, the hybrid mixed strategy (EA-MDSIF) allows obtaining a remarkably accurate geometry.

#### ***4.4.2 Results***

According to Figure 4.12 and Table 6, EA-MDSIF significantly outperforms all the EA-ADSIF cases, reaching the highest values of total depth and wall angles. The formed part is shown in

Figure 4.20. This could be attributed to the fact that the material is first moved from the inner to the outer circumference in the A-stage and then redistributed during the D-stage. Additionally, the reduced forming forces in the D-stage compared to those in EA-cDSIF (Figure 4.9) with the same amperage helped the process to form a deeper geometry. The fracture mechanics of EA-cDSIF will be discussed in Section 6.1. The process can be applied for the production of other parts characterized by a different geometry as well, as Figure 4.21 shows.

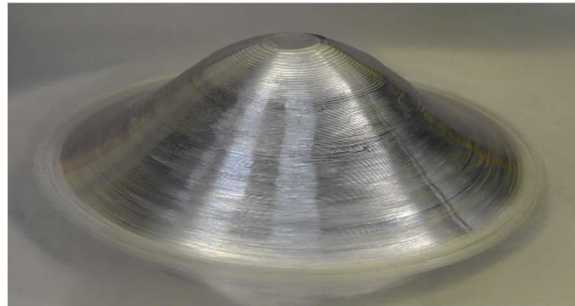


Figure 4.20 Ti6Al4V acetabular cup obtained with EA-MDSIF 50 *A*



(a)



(b)

Figure 4.21 Ti6Al4V pyramid part using EA-MDSIF 50 *A*: (a) desired part; (b) formed part

## **4.5 Implementation of Electrically-assisted post-forming annealing treatment**

In the previous sections electricity has been utilized to enhance process capability in deforming hard-to-form materials. Since elevated temperatures can be achieved through electricity, a novel on-site annealing platform is developed and tested in this section to eliminate redundant post-forming processes, i.e., part removal, re-assembly, or transportation before the annealing process to further improve process efficiency.

### ***4.5.1 Experimental setup***

Our work in Chapter 3 focused on springback removal using an off-site annealing method with additional portable clamping devices in a heated furnace (Zhang et al., 2016). This work has found that springback reduction increases as the annealing temperature and time increase. To reduce springback in a more efficient way, without part removal, re-assembly, or transportation after forming, this section develops an electrically-assisted on-site annealing method that generates elevated temperatures within the workpiece for meeting different requirements. This process is relatively easy to be implemented by passing an electrical current through the workpiece from the edges of the sheet.

As illustrated in Figure 4.22, the sheet metal was first electrically insulated from the machine using electrical tape in the clamping area. Holes were drilled on both side of the formed geometry to assemble the terminals of the power supply. The terminals were made from copper strips to provide uniformly distributed electrical current through the part. Black paint was applied to the part to avoid reflection when measuring the annealing temperature by the IR camera. A continuous current power supply (Dynatronix, model LFP12-300) was utilized to provide electrical current

through the part. To test the concept, the same material and geometry as presented in Section 3.5 were used. The maximum current of the power supply 300 A was applied during the annealing process.

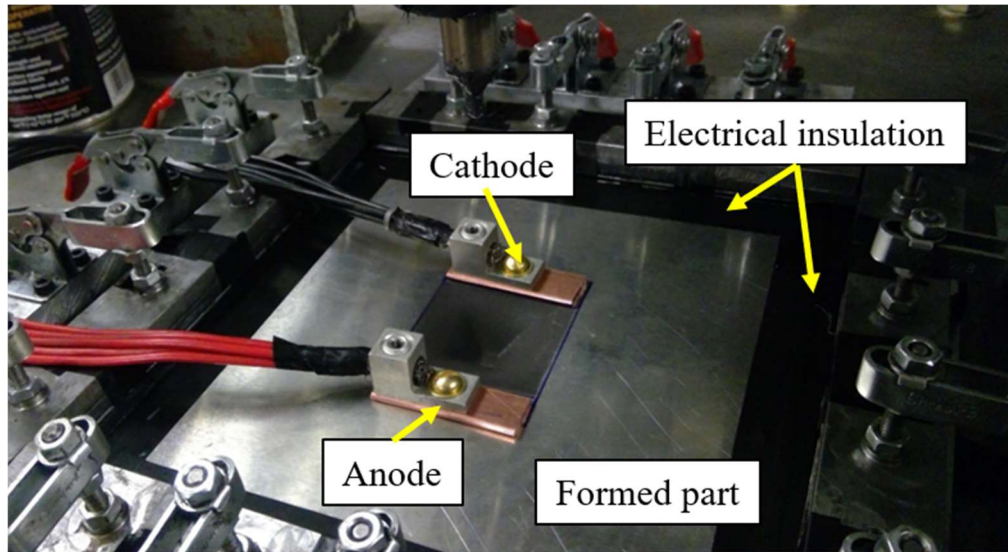


Figure 4.22 Experimental setup for electrically-assisted on-site annealing

#### 4.5.2 Results

A maximum temperature of 80 °C was achieved, and the part was annealed for half hour. Limited springback reduction was obtained due to the low temperature. Note that this on-site annealing setup was directly exposed to the room temperature environment.

According to the first law of thermodynamics, in Eq. (5), the capacitively stored heat rate  $P_{store}$  in the workpiece should be the sum of the generated heat rate  $P_{gen}$ , entering heat rate  $P_{in}$  and the heat loss rate  $P_{out}$  due to heat transfer.

$$P_{store} = P_{gen} + P_{in} - P_{out} \quad \text{Eq. (5)}$$

Therefore, to increase the temperature (or  $P_{store}$ ) in the workpiece, there are three possibilities:

(1) generating heat within the workpiece; (2) inducing external heat; and (3) decreasing heat loss.

In this case,

$$P_{store} = c\rho_m x_0 z_0 \Delta y \frac{\partial T}{\partial t} \quad \text{Eq. (6)}$$

$$P_{gen} = P_{Joule} = \rho_e x_0 z_0 \Delta y J^2 \quad \text{Eq. (7)}$$

$$P_{out} = P_{cond} + P_{conv} + P_{rad} = 2kx_0 z_0 \left| \frac{\partial T}{\partial y} \right| + 2h(x_0 + z_0) \Delta y (T - T_R) + 2\sigma x_0 y_0 (T^4 - T_R^4) \quad \text{Eq. (8)}$$

Note that,  $c$ ,  $\rho_m$  in Eq. (6),  $\rho_e$  in Eq. (7),  $k$ ,  $h$  and  $\sigma$  in Eq. (8) are the specific heat capacity, the mass density, the electrical resistivity, the thermal conductivity, the heat transfer coefficient under natural convection of the studied material, and Stefan-Boltzmann constant respectively,  $J$  ( $A/mm^2$ ) the current density,  $T$  the relative temperature ( $^{\circ}C$ ),  $T_R$  the room temperature,  $t$  the time.  $x_0$  is the width of applied current,  $y_0$  the length of current applied and  $z_0$  is the thickness of the sheet (Wang et al., 2016). To approximate heat loss, a static state in which  $P_{store}$  ( $W$ ) equals to zero is assumed. Moreover, the temperature variations in the direction of the electrical current are also assumed to be zero such that the conduction term is neglected.

From the ASM material data sheet of AA2024-T3,  $\rho_e$  is given as  $5.82 \times 10^{-8} \Omega \cdot m$ , both width  $x_0$  and length  $y_0$  are  $50 \text{ mm}$  in this case, thickness  $z_0$  is  $0.5 \text{ mm}$ ,  $h$  was determined by our previous experiments as  $h(T) = 2.9 \ln(T - T_R) + 1.987$ , and the current intensity is  $300 \text{ A}$  which corresponds to a  $J$  of  $12 \text{ A/mm}^2$ . Equation (5) returns a temperature of  $112 \text{ }^{\circ}C$ , which is close to



the measured temperature of 80 °C. It can also be determined that a significant heat loss of 10.5  $W$  occurs in the current setup where the sheet is exposed to the lab environment.

Since  $P_{gen} = P_{joule} \propto \rho_e J^2$ , where  $\rho_e$  is the electrical resistivity of the sheet metal and  $J$  is the current density. It is noted that this process is material-dependent. For the same current density  $J$ , stainless steel can generate almost 30 times more heat than aluminum can, making it harder to raise the temperature of aluminum sheets. Additionally, significant heat loss limited the increase of the annealing temperature. Therefore, future work could include thin plates with a reflective surface facing the sheet metal that could slide in during the annealing process to reduce heat loss and further increase the temperature of the formed parts through direct resistance heating.

## 4.6 Summary

This chapter has combined electricity with the DSIF, ADSIF and MDSIF processes and successfully achieved a double-curvature Ti6Al4V cup designed for hip replacements, which cannot be achieved under room temperature conditions. The forming forces were reduced in EA-ADSIF and EA-MDSIF: higher current intensities decrease the forming forces when the current is under 120 A. In EA-cDSIF, the forming forces depend more on the forming depth than the current intensity due to global bending outside the forming area.

The EA-MDSIF process, which is a hybrid process that applies electrical currents to MDSIF, has been proved to be an effective strategy for improving material formability and geometric accuracy of patient-specific Ti6Al4V biomedical products. Electric sparks (arcs), which often occur during EA-cDSIF due to contact problems, are eliminated. This chapter also describes a method to determine the actual forming temperature in the tool-sheet contact area, which is difficult to detect using IR cameras. Additionally, this chapter has tested a platform for electrically-assisted on-site annealing. Future work should include a design of a chamber to reduce heat loss for the on-site annealing process.

The ability to deform hard-to-form materials, as proposed in this chapter, will unlock an entirely new design domain in product development for strong, lightweight parts in manufacturing industries. As a result, current technologies can be further optimized with the added benefit of increased energy savings prior and during service life. Although titanium alloys were the focus of this chapter, the underlying principles of EA-DSIF will be applicable to most sheet metal material systems, thereby influencing countless products.

## **Chapter 5: Discovery of the mechanisms of electro-thermo-mechanical processes**

The hybrid processes of electrically-assisted DSIF (including EA-cDSIF, EA-ADSIF, and EA-MDSIF) presented in the last chapter have facilitated ISF with the capability to deform hard-to-form materials. While improved formability and reduced forming forces have been achieved, the dominant deformation mechanisms behind electro-thermo-mechanical deformation processes are still debated among researchers. This chapter establishes a new setup for *in situ* microstructural characterization under macroscopic electro-thermo-mechanical loading. By combining the material's macroscopic tensile behavior with the observed microstructural evolution, this chapter finds that pure thermo-mechanical effects dominate the electro-thermo-mechanical deformation process in Ti6Al4V, regardless of the different patterns of electricity applied (pulsed or continuous).

### **5.1 Literature review of the mechanisms of electro-thermo-mechanical loading processes**

Electroplasticity is an athermal material softening phenomenon induced by high density electrical currents during plastic deformation. It was reported that apart from the inevitable electrical resistance heating, the moving electrons themselves could dynamically reduce the material deformation resistance without substantial temperature increase (Ross et al., 2009). The electrical current was provided either continuously (Mai et al., 2011) or in the form of high-density pulses (Sprecher and Conrad, 1989). Previously published literature indicates that electrical currents could facilitate dislocation motion (Okazaki et al., 1978), influence dynamic

recrystallization (Xu et al., 2010), and accelerate phase transformation (Zhang et al., 2012). Fan et al. discussed that high density electrical currents are able to heat up local strengthening sites, such as the grain boundaries (Fan et al., 2013), due to their higher electrical resistance compared to the other parts of the material. The local temperature elevation at these strengthening sites assists dislocations to pass these locations regardless of the same temperature increase of the global bulk material.

Whether the governing mechanisms of the observed behaviors described above are due to electroplasticity is still a debatable topic in the research community. Magargee et al. conducted electrically-assisted tensile tests on pure titanium utilizing air-cooling which brought the sample temperature from 435 °C down to 27 °C (close to room temperature) and found similar tension behavior with that obtained from pure tensile tests without electricity at room temperature (Magargee et al., 2013b). Kinsey et al. also found that the flow stress strongly depends on temperature when current was applied in high strain rate tension tests (Kinsey et al., 2013). These findings bring into questions the existence or the significance of the electroplastic effect. Moreover, temperature-dependent models can well predict the stress drop behavior when electric current is applied. A temperature dependent viscoplasticity model (Bilyk et al., 2005) has successfully predicted the stress reduction observed by (Okazaki et al., 1978) when high current density pulses were applied. Unger et al. utilized a thermoelastic-viscoplastic model and found that the stress drop observed in the electrically-assisted tensile tests could be well explained by thermal expansion rather than the electroplastic effects (Unger et al., 2006). An inclusive model has been established under the consideration of thermal softening, solute-dislocation interaction and electron wind, which found that Joule heating is the major factor to affect the deformation

behavior (Wang et al., 2016). A summary of selected existing models on electro-mechanical behavior is shown in Table 8.

The mechanics of electrically-assisted deformation remains a controversial field with limitations at each side of the theory (Magargee, 2014). Therefore, it is important to perform an in-depth analysis on the deformation mechanisms to explain the material's behavior when subjected to electrically-assisted loading.

The fundamental difficulty in the study of electro-thermo-mechanical processes is that the underlying physical phenomena are mutually related. The interactions between the mechanical, thermal, electrical, and microstructural phenomena are illustrated in Figure 5.1. The particular phenomena referenced to by numbers in the figure are identified on the right. Depending on mechanical deformation, temperature history and the electrical effects, different phases and phase mixtures evolve. On the other hand, the mixture of the micro constituent determines the mechanical, thermal, and electrical properties of the material. Therefore, a realistic model for the process should consider the interactions between the mechanical, thermal, electrical, and microstructural fields. However, in general electro-thermo-mechanical numerical models, interaction numbers 1, 2, 8, 9, and 10 (marked green in Figure 5.1) are accounted for without the consideration of the microstructural field or the possible electro-mechanical interaction 7 (Nielsen et al., 2012), which are marked orange in Figure 5.1. In some realistic finite element models for thermo-mechanical processes such as conventional hot stamping processes without the involvement of the electricity, interaction numbers 1a, 2a, 3, 4ab and 5abc have been implemented for process simulation (Bergman, 1999) to capture the interactions between the mechanical, thermal and microstructural effects. Thanks to the transfer of microstructural evolution data within

the process simulation, final properties, such as hardness and tensile strength, can then be properly modeled (Jeswiet et al., 2008). Hence, it is important to understand and include the interactions between the four fields into the study of the electro-thermo-mechanical deformation processes.

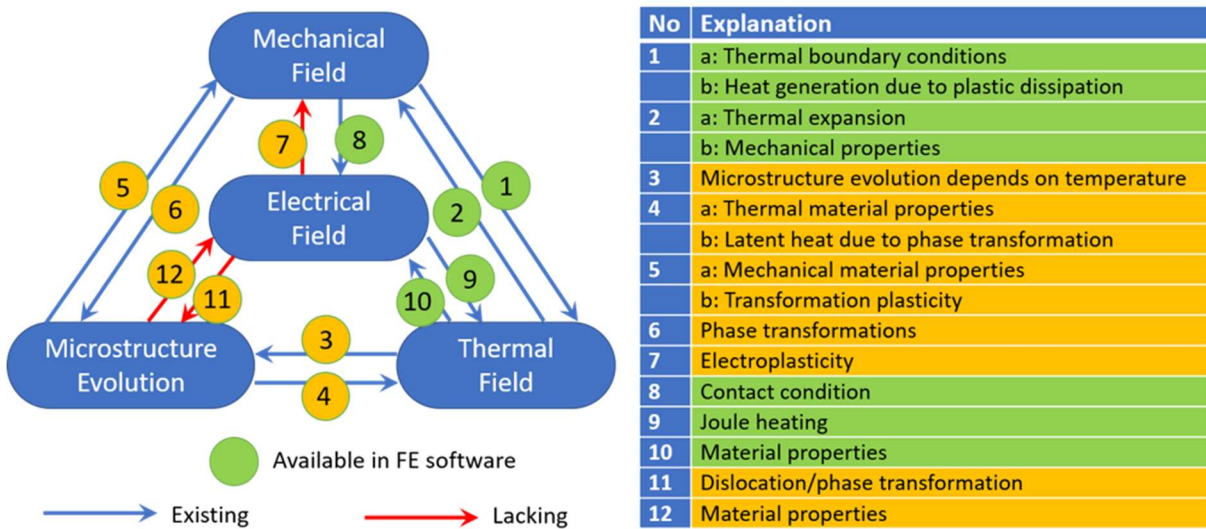


Figure 5.1 Interactions between mechanical, thermal, electrical, and microstructural phenomena

The development of hybrid processes requires the understanding of the microstructure evolution and the interactions between electrical, thermal and mechanical fields. However, the dominant mechanisms behind the electro-thermo-mechanical loadings, especially the red-arrowed items in Figure 5.1 have not yet been fully studied. Some researchers only analyzed the macroscopic tensile behavior when the material was subjected to electrically-assisted tensile tests (Lee et al., 2017, Okazaki et al., 1978, Wang et al., 2016), without direct investigation on microstructures. Some did microstructural examination after the material was processed (Fan et al., 2013). Some researchers investigated the *in situ* microstructural evolution when the electricity passed through a downsized specimen for TEM without mechanical loading (Conrad, 2000). A

brief survey of these factors, key findings and limitations are summarized in Table 7. The problems in the existing studies lie in the omission of *in situ* examinations of the real microstructural evolution when the material is subjected to macroscopic electro-thermo-mechanical loading. Considering the above-stated shortcomings in the understanding of the underlying interactions between the aforementioned physical processes, the “lacking” items in Figure 5.1 are investigated by *in situ* X-ray diffraction (XRD) experiments in this chapter.

Direct comparison among pure thermal heating, continuous current and pulsed current is missing. Some researchers stated that high-energy electrical pulses accelerate the phase transformation of the material due to electroplasticity (Zhang et al., 2012). However, the conclusion was drawn from ex-situ XRD measurements without any direct comparison between the electropulsing case and continuous current case or pure thermal heating case. Therefore, this chapter proposes direct comparisons among the three heating cases to substantiate this theory. At each temperature group, three sets of tensile tests are conducted with: 1) pure thermal heating, 2) pulsed current, and 3) continuous current, respectively.

The material used in this study is Ti6Al4V, the same material studied in the previous chapter. It is a lightweight high-strength structural material with high corrosion resistance and high biocompatibility which has been widely used in the automotive, aerospace, civilian, and medical industries (Li et al., 2014). It is difficult to form at room temperature, so heated forming methods are often used. Constitutive models that describe the flow stress of Ti6Al4V at elevated temperatures are listed in Table 9

Ti6Al4V is a two-phase ( $\alpha+\beta$  phase) alloy with its microstructure strongly sensitive to processing parameters. The  $\alpha$  phase has an hcp structure which is harder than the  $\beta$  phase which

has a bcc structure. The mechanical behaviors are different in the two phases and the phase composition to a great extent controls the mechanical response. The identification of the two phases is crucial for understanding the macroscopic mechanical response of this material.

In the following sections, the experimental setup of the *in/ex situ* material characterization to measure the phase fraction evolution under electro-thermo-mechanical uni-axial loading is introduced. The comparison between the effects of pulsed currents and continuous currents assists the identification of the athermal effects in Section 5.4. Moreover, the results are expected to settle the controversy about the existence of electroplasticity.



Table 7 Key findings and limitations regarding electro-thermo-mechanical deformation

Reference	Material	Current Pattern	Temperature (°C)	Loading Method	Characterization Method	Findings	Limitations
(Okazaki et al., 1978)	Ti, Pb, Fe, Sn	Pulsed	Small change of 20	Macro-scale tensile	Macroscopic stress-strain curves	Electroplastic effect reflects electron-dislocation interaction	No microstructural evidence
(Salandro et al., 2012)	Ti, Ti6Al4V	Continuous	392 450	Macro-scale compression	Macroscopic stress-strain modeling	Quantified electroplastic effect coefficient	No microstructural evidence for the model
(Fan et al., 2013)	70/30 Brass	Continuous	350	Macro-scale tensile	<i>Ex situ</i> SEM	Local grain boundary heating	No direct <i>in situ</i> evidence
(Ye et al., 2014)	Ti6Al4V	Pulsed	450-684	No loading	<i>Ex situ</i> XRD	Electroplasticity accelerates phase transformation	No direct <i>in situ</i> evidence
(Kang et al., 2016)	Single crystal copper	Continuous	No change	Micro-scale tensile	<i>In situ</i> TEM	No electron-dislocation interplay (electroplasticity)	Not extendable to macro-scale loadings and samples
(Wang et al., 2016)	AZ31 magnesium alloy	Continuous	58-240	Macro-scale tensile	Macroscopic stress-strain modeling	Thermal softening dominates force reduction	No microstructural evidence for the model
(Lee et al., 2017)	Ti	Single pulse	100-210	Macro-scale tensile	Macroscopic stress-strain modeling	Thermal softening, thermal expansion, and dynamic strain aging affect force reductions	No microstructural evidence for the model

Table 8 Electro-mechanical models

Reference	Expression	Theory
(Conrad, 2002)	$\ln\left(\frac{\dot{\epsilon}_{ed}}{\dot{\epsilon}_l}\right) = \ln\left(\frac{\dot{\epsilon}_{0ed}}{\dot{\epsilon}_0}\right) - \frac{\Delta H_{ed}^* - \Delta H^*}{kT} + \frac{(v_{ed}^* - v^*)\sigma^*}{kT} + \frac{v_{ed}^*\sigma_{ew}}{kT}$	Thermally-activated dislocation motion
<p>The subscript <i>ed</i> indicates that the values are associated with the current pulse; <math>\dot{\epsilon}_l</math> is the strain rate prior to the application of a current pulse; <math>\dot{\epsilon}_0</math> is the pre-exponential factor; <math>\Delta H^*</math> is the Gibbs free enthalpy of activation; <math>v^*</math> is the activation volume; <math>\sigma^*</math> is the effective stress; <math>\sigma_{ew}</math> is the additional stress acting on dislocations due to the force exerted by drift electrons; <math>k</math> is the boltzmann constant</p>		
(Molotskii, 2000)	$\Delta\sigma = \sigma^* \frac{J^2}{J^2 + J_0^2}; J_0 = \frac{2H_0}{r}$	Dislocation depinning from paramagnetic obstacles
<p><math>\sigma^*</math> is the effective stress; <math>J</math> is current density; <math>J_0</math> is a characteristic current density; <math>H_0</math> is the characteristic value of the magnetic field at which efficient depinning of the dislocations from paramagnetic obstacles takes place; <math>r</math> is the radius of the wire</p>		
(Li and Yu, 2011)	$\dot{\epsilon}_e = \dot{\epsilon} \exp\left[\ln\left(\frac{\dot{\epsilon}_{0e}}{\dot{\epsilon}_0}\right) + \left(\frac{\chi t}{n\gamma kT} J^2\right)\right]$	Free-electron theory
<p><math>\dot{\epsilon}_e</math> is the plastic strain rate with electricity applied; <math>\dot{\epsilon}</math> is the plastic strain rate without electricity applied; <math>\dot{\epsilon}_{0e}</math> is the pre-exponential factor with electricity applied; <math>\dot{\epsilon}_0</math> is the pre-exponential factor without electricity applied; <math>\chi</math> is the average number of metallic ions forming a dislocation; <math>t</math> is the acting time of the electric current; <math>n</math> is the free electron number of a unit volume of metal; <math>\gamma</math> is electrical conductivity; <math>k</math> is the boltzmann constant; <math>J</math> is the current density</p>		
(Bunget et al., 2010)	$J^* = F\dot{u} + \xi VI = C\bar{\epsilon}^n \dot{\epsilon}^m \left(1 + \frac{2\mu r_0}{3h}\right) \pi r^2$	Energy balance

<p><math>J^*</math> is the upper bound on power; <math>F</math> is the forming load; <math>\dot{\mathbf{u}}</math> is the velocity of the compressive die; <math>\xi</math> is the electroplastic effect coefficient; <math>V</math> and <math>I</math> are voltage and current intensity; <math>r</math> and <math>h</math> are the instantaneous radius and height of workpiece</p>		
(Bilyk et al., 2005)	$\dot{\bar{\epsilon}} = \frac{\epsilon_1 \dot{\epsilon}_2}{\epsilon_1 + \epsilon_2}, \quad \epsilon_1 = \dot{\epsilon}_0 \left[ \frac{\bar{T}}{g(\bar{\epsilon}, \theta)} \right]^m, \quad \epsilon_2 = \dot{\epsilon}_m \exp \left[ -\frac{ag(\bar{\epsilon}, \theta)}{\bar{T}} \right], \quad g(\bar{\epsilon}, \theta) = T_0(1 + \bar{\epsilon}/\epsilon_0)^N \{1 - \beta[(\theta/\theta_0)^\kappa - 1]\}$	Thermo-viscoplasticity
<p><math>\bar{\epsilon}</math> is the equivalent plastic strain; <math>\dot{\epsilon}_0</math> is a reference strain rate; <math>m</math> and <math>a</math> are the rate-sensitivity parameters; <math>T_0</math> is a reference stress; <math>N</math> is the strain hardening exponent; <math>\theta_0</math> is a reference temperature; <math>\beta</math> and <math>\kappa</math> are thermal-softening parameters; <math>g(\bar{\epsilon}, \theta)</math> represents the stress-strain relation at a quasi-static strain rate <math>\dot{\epsilon}_0</math></p>		
(Magargee et al., 2013a)	$\sigma = B\epsilon^n \left[ 1 + C \ln \left( \frac{\dot{\epsilon}}{\dot{\epsilon}_0} \right) \right] f(\bar{T}); \quad f(\bar{T}) = \alpha \exp(\beta \bar{T}); \quad \bar{T} = (T_m - T)/(T_m - T_R)$	Thermal softening
<p><math>\alpha, \beta</math> are material constants; <math>T_m</math> is the melting temperature; <math>T_R</math> is the reference temperature</p>		
(Lee et al., 2017)	$\dot{\epsilon}_{DSA} = D\theta b\rho_m l / (a^*)^2$	Dynamic strain aging
<p><math>D</math> is the diffusion coefficient; <math>\theta</math> is the orientation factor of metallic crystal; <math>b</math> is the Burgers vector magnitude for the dislocation; <math>\rho_m</math> is the dislocation density; <math>l</math> is the average distance between two obstacles; <math>a^*</math> is the average activation distance for dislocations</p>		

Table 9 Constitutive models for Ti6Al4V at elevated temperature

Model	Form	Parameters	Type
Johnson-Cook (JC)	$\sigma_f = (A + B\varepsilon^n) \left[ 1 + C \ln\left(\frac{\dot{\varepsilon}}{\dot{\varepsilon}_0}\right) \right] \left[ 1 - \left(\frac{T - T_0}{T_m - T_0}\right)^m \right]$	$A, B, C, n, m$	Phenomenological
Modified JC (m-JC)	$\sigma_f = (A_1 + B_1\varepsilon + B_2\varepsilon^2) \left[ 1 + C_1 \ln\left(\frac{\dot{\varepsilon}}{\dot{\varepsilon}_0}\right) \right] \exp\left\{ \left[ \lambda_1 + \lambda_2 \ln\left(\frac{\dot{\varepsilon}}{\dot{\varepsilon}_0}\right) \right] (T - T_0) \right\}$	$A_1, B_1, B_2, C_1, \lambda_1, \lambda_2$	Phenomenological
Modified Arrhenius (m-Arr)	$\sigma_f = \frac{\beta_0}{\alpha} \varepsilon^{\beta_1} \exp(\beta_2 \varepsilon) \ln \left\{ \left(\frac{Z}{A}\right)^{1/n} + \left[ \left(\frac{Z}{A}\right)^{2/n} + 1 \right]^{1/2} \right\};$ $Z = \dot{\varepsilon} \exp\left(\frac{Q}{RT}\right); \beta_i = A_i \ln Z + B_i$	$A, \alpha, n, Q, A_0, B_0, A_1, B_1, A_2, B_2$	Phenomenological
Modified Zerilli-Armstrong (m-ZA)	$\sigma_f = (C_1 + C_2\varepsilon^n) \exp\left\{ -(C_3 + C_4\varepsilon)(T - T_0) + [C_5 + C_6(T - T_0)] \ln\left(\frac{\dot{\varepsilon}}{\dot{\varepsilon}_0}\right) \right\}$	$C_1, C_2, C_3, C_4, C_5, C_6, n$	Physical-based
Rusinek-Klepaczko (RK)	$\sigma_f = \frac{E(T)}{E_0} [\sigma_\mu + \sigma^*] \quad ; \quad E(T) = E_0 \left\{ 1 - \left[ \left(\frac{T}{T_m}\right) \exp\left[\theta^* \left(1 - \frac{T_m}{T}\right)\right] \right] \right\} \quad ; \quad \sigma_\mu =$ $B_0 \left[ \left(\frac{T}{T_m}\right) \log\left(\frac{\varepsilon_{max}}{\dot{\varepsilon}}\right) \right]^{-\nu} (\varepsilon_0 + \varepsilon_p)^n \quad ; \quad n = n_0 \left[ 1 - D_2 \left(\frac{T}{T_m}\right) \log\left(\frac{\varepsilon_p}{\varepsilon_{min}}\right) \right]; \quad \sigma^* = \sigma_0^* \left[ 1 -$ $D_1 \frac{T}{T_m} \log\left(\frac{\varepsilon_{max}}{\dot{\varepsilon}}\right) \right]^m$	$B_0, \nu, n_0, D_2, \sigma_0^*, m, D_1$	Physical-based
Picu-Majorell (PM)	$\sigma = (1 - C_\beta(T))^w (\sigma_\alpha^* + \sigma_{\mu\alpha}) + C_\beta(T)^w \sigma_\beta; \quad \sigma_\alpha^* = \sigma_\alpha^0 \left[ 1 - \left(\frac{kT}{\Delta G_\alpha} \ln \frac{\dot{\varepsilon}_{\alpha 0}}{\dot{\varepsilon}}\right)^{1/q_\alpha} \right]^{1/p_\alpha}; \quad \sigma_{\mu\alpha} = a\mu(T)b\sqrt{\rho} + \kappa d^{-1/2}; \quad \mu(T) = \mu_0 - \frac{e}{\exp\left(\frac{T_r}{T}\right) - 1}$ $\sigma_\beta = \sigma_\beta^0 \left[ 1 - \left(\frac{kT}{\Delta G_\beta} \ln \frac{\dot{\varepsilon}_{\beta 0}}{\dot{\varepsilon}}\right)^{1/q_\beta} \right]^{1/p_\beta}$	$w, \sigma_\alpha^0, \Delta G_\alpha, \dot{\varepsilon}_{\alpha 0}, \sigma_\beta^0, \Delta G_\beta, \dot{\varepsilon}_{\beta 0}, q_\alpha, q_\beta, p_\alpha, p_\beta$	Physical-based

## 5.2 *In/ex situ* X-ray diffraction study

The commonly used Digital Image Correlation (DIC) technique measures the gross or bulk sample deformation (often called macrostrain) and is relatively insensitive to the actual mechanisms of material deformation. This prevents a direct understanding of mechanical responses since the material can respond to an external load by several different pathways simultaneously. Hence, in this chapter, a synchrotron-based X-ray technique (Bronfenbrenner et al., 2010) to directly measure the actual micro-strain response of a material during macroscopic loading will be introduced to unveil the major deformation mechanisms behind electro-thermo-mechanical loading.

Both *in situ* and *ex situ* XRD experiments were conducted at Sector 11 at the Advanced Photon Source (APS) at Argonne National Laboratory (ANL). The utilization of high-energy X-rays (105.592 keV) allows for probing thick samples due to the deep penetration depth compared to the conventional lab-based X-ray sources. The XRD measurement system has three major components (Figure 5.2): high-energy X-ray source, 6-axis sample stage and an area detector. The loading system consists of five parts: mechanical testing machine (SEMtester 1824LM), electric current supplies (Dynatronix CRS-LFP12-300 for continuous current and IXYS PCX-7500 for pulsed current), IR camera (FLIR 655sc), DIC system (Vic 2D), and nitrogen gas for both cooling and heating purposes. When performing the *in situ* X-ray measurements, the specimen was mounted on the tensile testing machine with the X-ray beam passing through the center of the specimen from its side. During the simultaneous electro-tensile loading, the macroscopic strain was measured by the DIC system, the temperature was monitored by the IR camera, the stress was

recorded by the load cell that was attached to the tensile testing machine. The nitrogen gas system could provide gas temperatures of  $-100^{\circ}\text{C} \sim 160^{\circ}\text{C}$ . The *ex situ* XRD measurements were carried out on the samples without using the loading system.

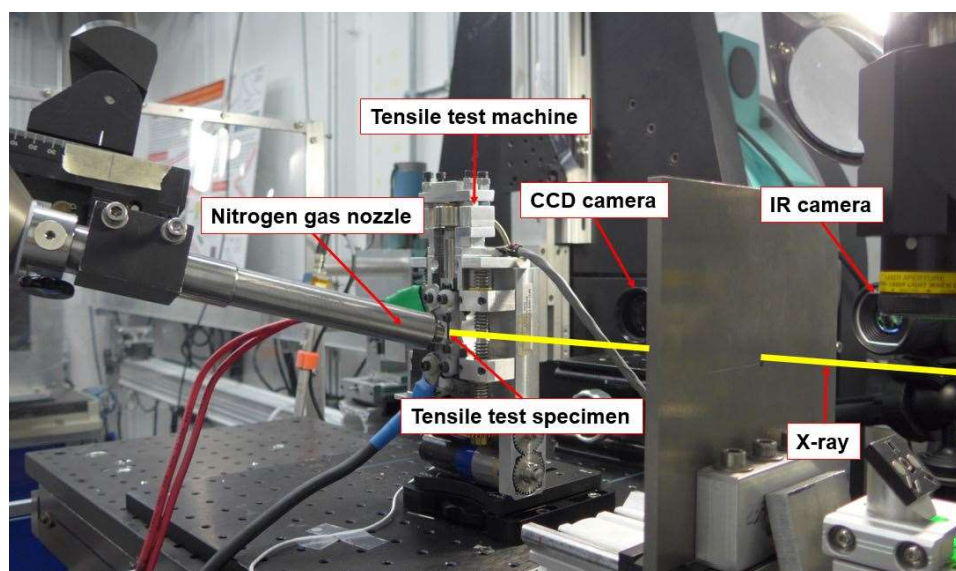


Figure 5.2 *In situ* high-energy XRD measurement setup. The yellow line (from right to left) indicates the X-ray path.

To determine the deformation mechanisms in the electro-thermo-mechanical loading system, *in situ* high-energy XRD measurements were used to study the following four tensile loading processes: 1) with continuous current, 2) with pulsed current, 3) with injecting hot gas but without electricity, 4) at room temperature without applying current or flowing gas. Time-evolved X-ray diffraction images were recorded by the 2D detector with a time interval of 10 s. X-ray dark images were also collected for the background removal.  $\text{CeO}_2$  powder standard was used to calibrate the beam center position, and the sample to detector distance. By using the extracted parameters, the pixel-array images can be converted into Q-space. Circular averaging was performed along each

individual X-ray diffraction ring to generate the 1D line profiles. The  $\alpha$ - and  $\beta$ -Ti diffraction peaks were subsequently identified by comparing the entries in the ICSD database.

To compare the volume fractional changes of  $\alpha$ - and  $\beta$ -Ti phases from the extracted 1D line data shown in Figure 5.8, the fractions can be estimated from the measured peak areas under the  $\alpha$ - and  $\beta$ -Ti diffraction peaks. The intensity fractions  $C_{\beta XRD}$  and  $C_{\alpha XRD}$  are defined as the ratio of the sum of the measured peak area for each phase to the total peak area in a single XRD pattern:

$$C_{\beta XRD} = \frac{\int I_{\beta}(Q)dQ}{\int I(Q)dQ} \quad \text{Eq. (9)}$$

The volume fraction value of each phase was derived by adding a normalization factor determined between the metallographic measurement and the peak area measurement at a reference temperature, which is usually the room temperature (Palmer et al., 2002):

$$C_{\beta}(T) = C_{\beta XRD}(T) \frac{C_{\beta}(T_0)}{C_{\beta XRD}(T_0)} \quad \text{Eq. (10)}$$

$$C_{\alpha} = 1 - C_{\beta} \quad \text{Eq. (11)}$$

In this case, three representatives with strongest peaks, two  $\alpha$ -Ti peaks ( $Q \sim 2.82 \text{ \AA}^{-1}$  and  $Q \sim 2.68 \text{ \AA}^{-1}$ ) and one  $\beta$ -Ti peak ( $Q \sim 2.75 \text{ \AA}^{-1}$ ), were chosen and used for a simple estimation since other weak peaks have insignificant influence on the results of  $\beta$ -Ti phase fraction during the entire loading process. Note that the location of each peak moves with the loading process due to heat expansion. Each peak was searched and was fitted with a Gaussian function with a constant background. The area, position, and width of all three peaks were extracted and plotted as a function of time.

The results of this work, which are presented in the following sections are valuable as they provide the exact macroscopic tensile behavior and corresponding microstructural response while the material is under electro-thermo-mechanical loading. The interactions between the microstructural fields and the electrical, thermal, and mechanical fields can thereby be both qualitatively and quantitatively determined.

### **5.3 Electrically-assisted tensile tests**

#### ***5.2.1 Experimental setup***

The loading system has been introduced in the previous section. Specimens (Figure 5.3) were extracted from 0.5 mm thick Ti6Al4V sheet. Each group of the *in situ* measurements included three sets of tensile test experiments (with continuous current, with pulsed current, and with thermal heating) conducted at the same temperature. The parameters of both continuous current and pulsed current were selected so that the temperature outputs remain the same (No. 2 in Figure 5.4). Stress-strain curves were obtained from each test in parallel with *in situ* XRD data as described before. Then the athermal effects were evaluated based on the difference in the mechanical and microstructural outputs from different types of energy inputs. In this section, the macroscopic mechanical behaviors are discussed first.



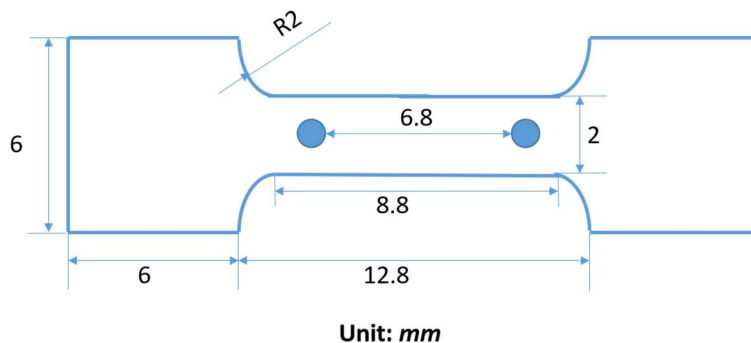


Figure 5.3 Dimension of the tensile test specimen

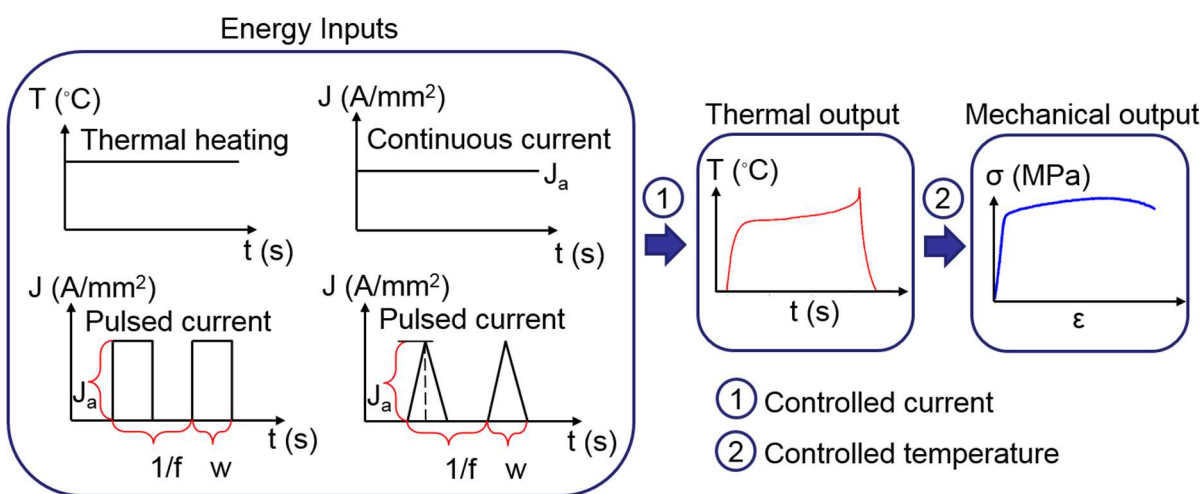
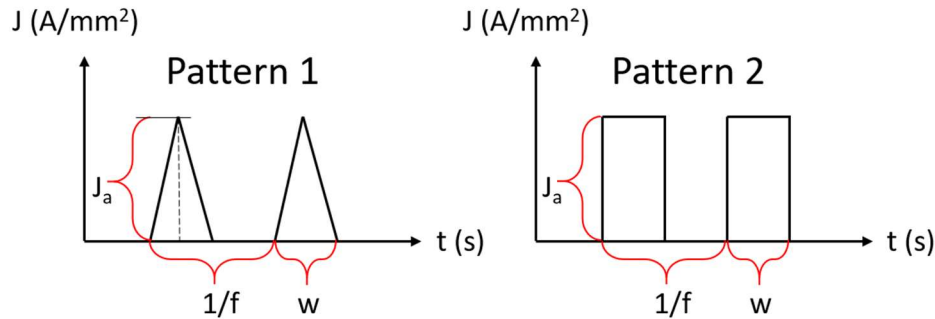


Figure 5.4 Relationships between energy inputs and outputs

Three temperature groups were selected to study the electro-thermo-mechanical loading processes. The temperature of the EA tensile tests was defined as the stabilized temperature before necking. Necking leads to a sudden temperature rise in the sample. These groups were the low temperature group with a temperature of 160 °C, medium temperature group with a temperature of 480 °C, and a high temperature group with 700 °C. The input parameters for the electrical currents investigated in this chapter are listed in Table 10. The strain rate for the tensile tests was at  $10^{-3} s^{-1}$ . Speckles for DIC analysis were prepared with black and white Rust-Oleum high heat paints.

Table 10 Experimental specifications of EA tensile tests



Temp (°C)	$J_a$ (A/mm <sup>2</sup> )	$w$ (μs)	$f$ (Hz)	Pattern
Low (160)	94	4	5200	1
Low (160)	13.1	40	5200	2
Low (160)	6	N/A	N/A	Continuous
Med (480)	233	4	5200	1
Med (480)	30	40	5200	2
Med (480)	13	N/A	N/A	Continuous
High (700)	258	4	5200	1
High (700)	35	40	5200	2
High (700)	17.5	N/A	N/A	Continuous

For the pure thermal tensile tests in the low temperature group, heated nitrogen gas was utilized to increase the temperature of the samples. Since the maximum temperature of the nitrogen gas system was 160 °C, a heat gun that was able to blow hot air ranging from room temperature to 500 °C was utilized for the pure thermal tensile tests in the medium temperature group. Thermo-mechanical loading at the high temperature was not available due to the lack of a pure thermal device providing high temperature convection or conduction that generates a comparable heating rate in the sample as electricity. The samples were first preloaded to about 30 N to avoid bending due to heat expansion in the beginning. Then, electricity and hot air were applied to the samples. Loading processes were initiated immediately afterwards.

### 5.2.2 Results

The macro-scale mechanical outputs for each temperature group together with the corresponding energy inputs and temperature histories are demonstrated below.

From the results in Figure 5.5, when temperature is retained at 160 °C before necking, similar mechanical behaviors are observed. An elevated temperature results in a 20% force reduction as compared to the room temperature tensile test. Comparing the pure thermal test (Air 160 °C) with other EA tensile tests, no difference in macroscopic mechanical behavior has been noticed. No further force drop occurs in pulsed current cases as compared to the continuous current case. Therefore, in the low temperature group, electro-thermo-mechanical behavior is the same as thermo-mechanical behavior, regardless of the different patterns of electricity applied.

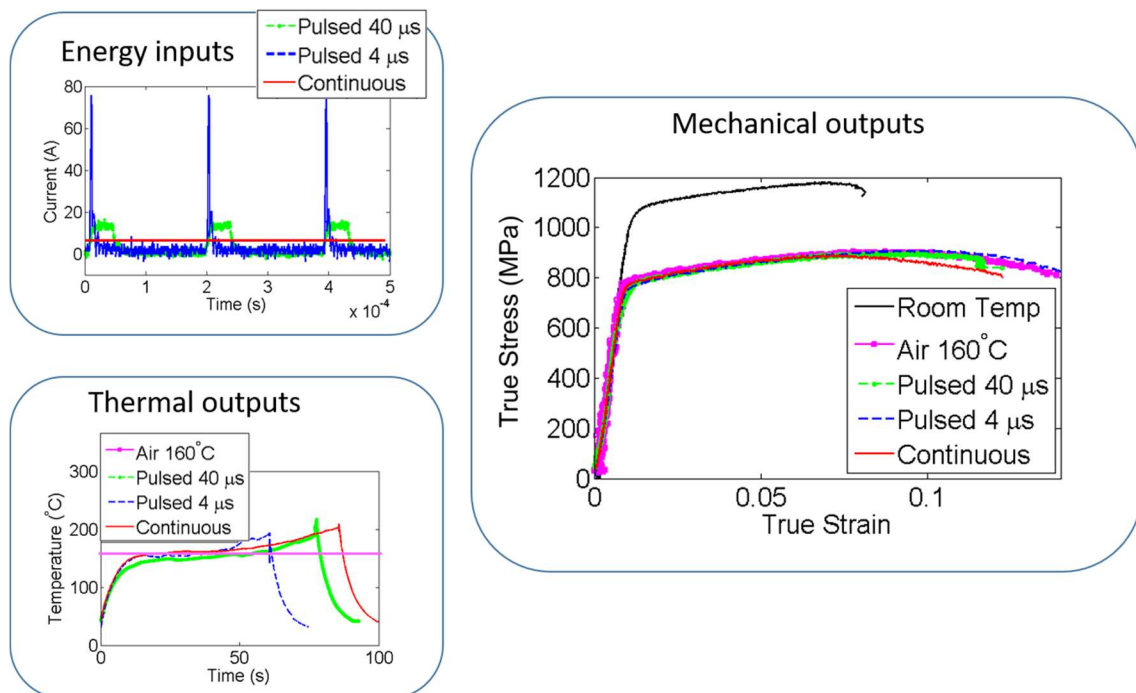


Figure 5.5 Energy inputs, temperature histories and macroscale tensile behaviors in the low temperature group

For the medium temperature group demonstrated in Figure 5.6, EA tensile tests present similar mechanical behavior as the pure thermal test. The oscillating temperature profile of the pure thermal test indicates that the heat gun cannot provide a temperature output as stable as the nitrogen gas system. In the EA tensile tests, temperature increased during necking causing further elongation of Ti6Al4V. The study has shown that Ti6Al4V exhibits superplastic behavior when loaded at  $10^{-3} s^{-1}$  and at temperature above 700 °C (Park et al., 2008). Therefore, the pure thermal tensile test fractured prior to the EA tensile tests due to the relatively lower temperature during necking. Apart from the superplastic behavior, in the medium temperature group, electro-thermo-mechanical behavior is also the same as thermo-mechanical behavior, regardless of the different patterns of electricity applied. No evidence of electroplastic effects has been found in macroscopic tensile behaviors.

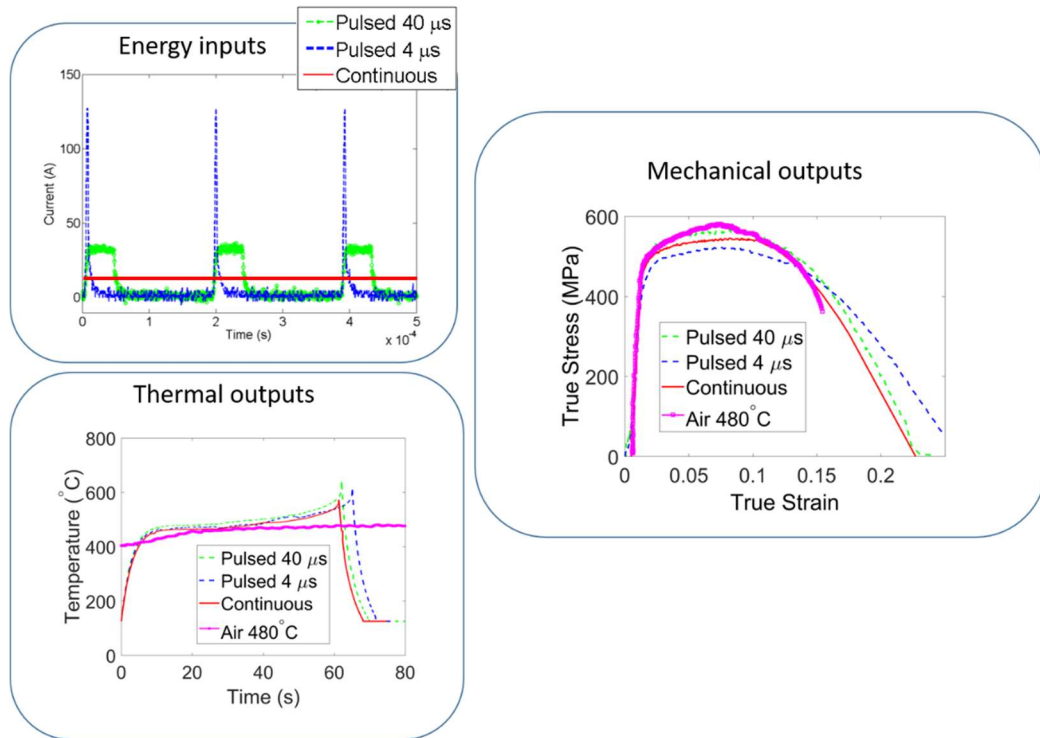


Figure 5.6 Energy inputs, temperature histories and macroscale tensile behaviors in the medium temperature group

For the high temperature group shown in Figure 5.7, strain information was not available due to the melt of the speckled paint for DIC analysis. Therefore, engineering stress with respect to loading time is plotted. Due to superplastic effects, samples kept elongating at a low stress level without fracture ( $30 \text{ MPa}$ ). Electricity was turned off when the force reached a low level. A small peak in stress appeared before the fracture of the sample due to hardening. Pure thermal tests were not performed because it was difficult to achieve a high temperature via convection in an open environment. Conclusions about the existence of electroplasticity at high temperature cannot be drawn due to the lack of strain information and lack of pure thermal tensile test data. Future work could include the design of a pure thermal heating device with high heating rates. Additionally, a laser extensometer could be utilized in the future for strain recording.

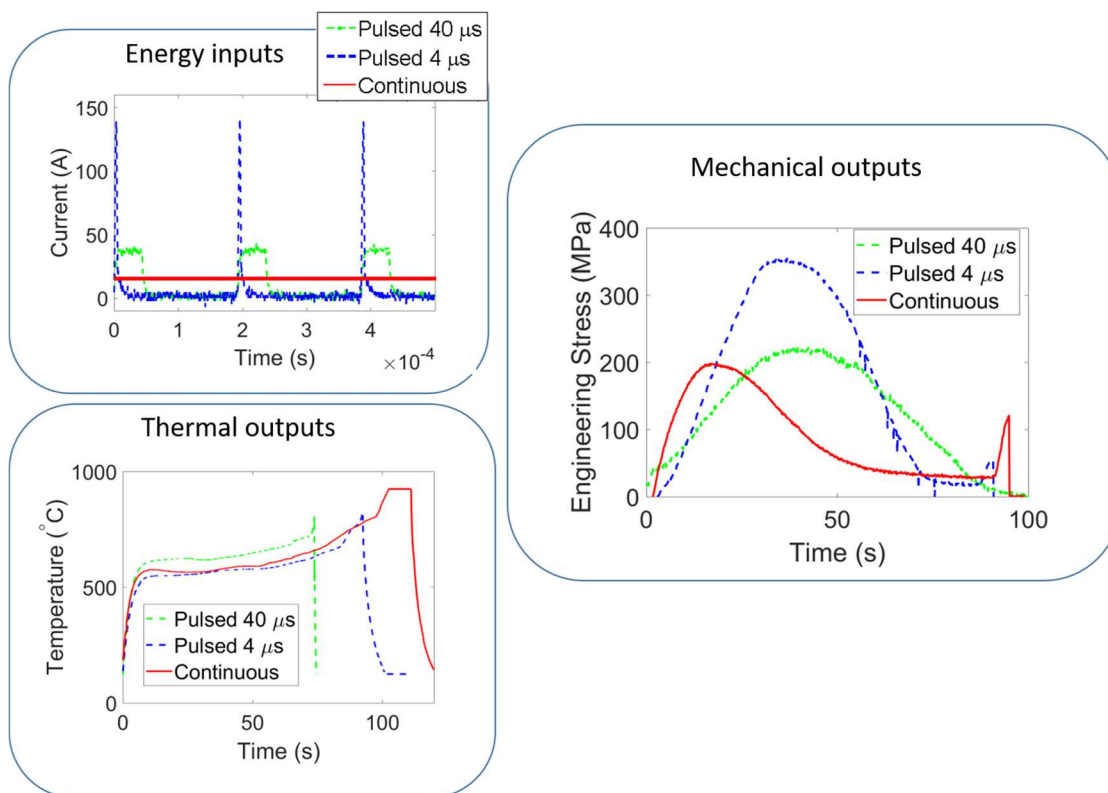


Figure 5.7 Energy inputs, temperature histories and macroscale tensile behaviors in the high temperature group

#### 5.4 Microstructural responses under electro-thermal-mechanical loading

In the previous section, it has been determined that the difference among 1) air heating (pure thermal effects), 2) pulsed current (potential existence of athermal effects) and 3) continuous current (potential existence of athermal effects) in tensile loadings is negligible at low (160 °C) and medium temperatures (480 °C). The microstructural responses measured in the *in situ* XRD study are presented in this section to further identify the existence of athermal effects during electro-thermo-mechanical loading.

The *in situ* XRD patterns at different time steps during the EA tensile loading under a continuous current density of  $17.5 \text{ A/mm}^2$  in the high temperature group are plotted in Figure 5.8. In this case, the  $\beta$  phase increased with time. In addition, since  $Q = 2\pi/d$  where  $Q$  is the value of the momentum difference between incoming and diffracted X-rays of a crystal,  $d$  is the lattice spacing, the lattice of both phases expanded with loading temperature.

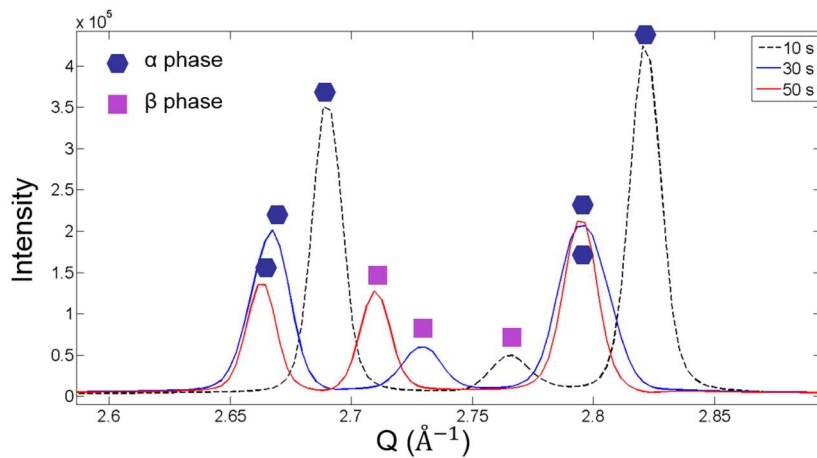
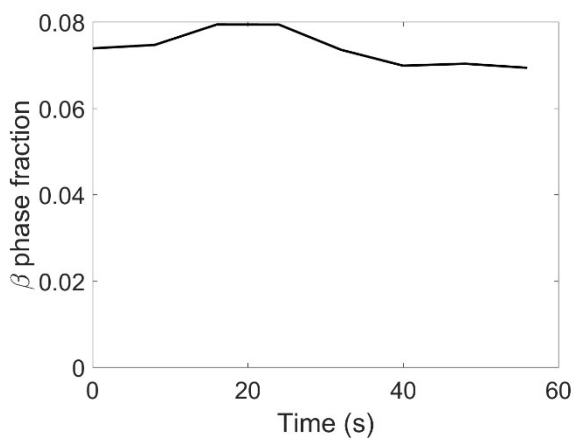


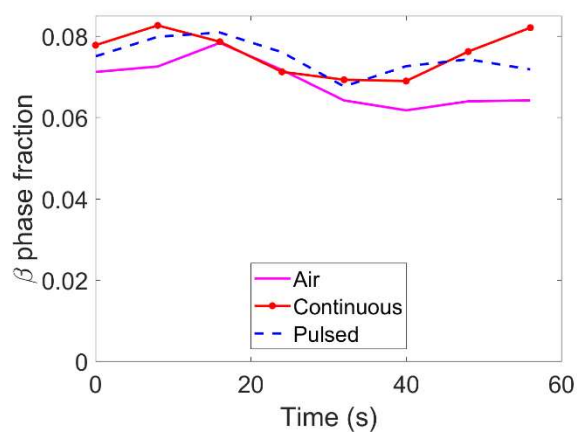
Figure 5.8 *In situ* high-energy XRD measurements for EA tensile tests under a continuous current density of  $17.5 \text{ A/mm}^2$

The  $\beta$  phase fractions measured during different loading processes in each temperature group are plotted in Figure 5.9. From Figure 5.9a and Figure 5.9b, the  $\beta$  phase fractions during tensile tests under both room temperature and low temperature conditions vary insignificantly and stay within the range of 0.065 and 0.085. Similarly, in the medium temperature group in Figure 5.9c, the difference in the evolutions of the  $\beta$  phase fraction before necking (40 s) between EA tensile tests using pulsed and continuous currents is negligible. The variation after 40 s may be due to the difference in progressive elongations. It can be noted that the fraction drops first then increases at the end. This is because the equilibrium state of the  $\beta$  phase fraction in this material at medium

temperature is lower than at the as-received level. When the temperatures rise above the threshold due to necking, which results in the increase of current density, the  $\beta$  phase increases back to the value at the corresponding elevated temperature. Therefore, unlike the microstructural responses in the low and medium temperature groups, where the  $\beta$  phase fraction undergoes a decreasing stage first, the fraction steadily increases in the high temperature group. Microstructural evolution under pure annealing conditions are studied in the next section. A slight difference is observed between the fraction evolutions under pulsed and continuous currents. Due to the superplastic behavior of Ti6Al4V, the samples underwent extensive deformation under a low stress level. It was difficult to control the deformation over time at high temperatures as shown in Figure 5.7. Therefore, a conclusion about the existence of electroplasticity at high temperatures cannot be drawn. Further studies in the high temperature case will be needed.



(a)



(b)



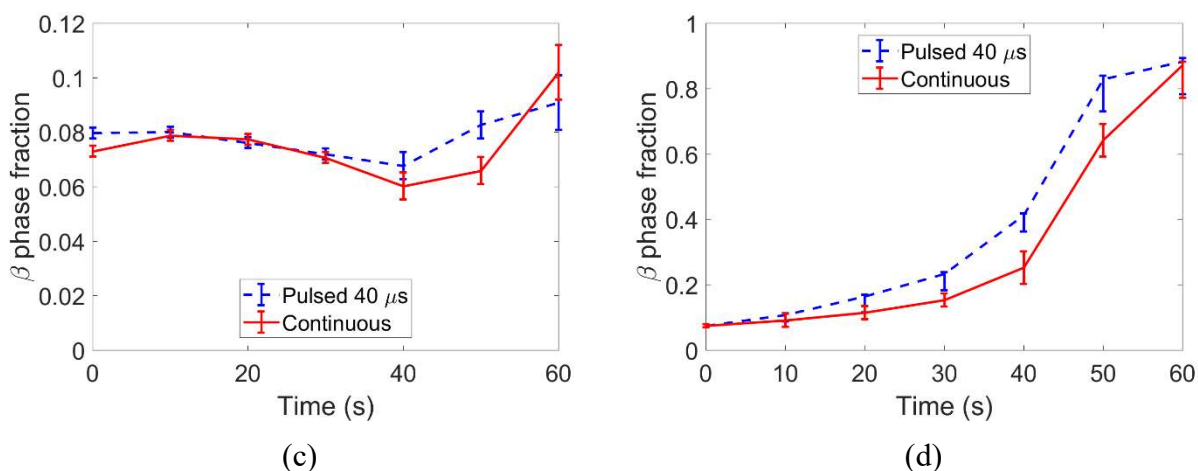


Figure 5.9 *In situ* measurements of  $\beta$  phase fraction evolution in: (a) room temperature; (b) low temperature group; (c) medium temperature group; (d) high temperature group

*Ex situ* XRD measurements have also been performed right after the fracture of the aforementioned *in situ* specimen. The 2D diffraction patterns at different locations are plotted in Figure 5.10. Varying patterns indicate that the material was non-uniform upon fracture. This was caused by the non-uniform temperature distribution. Therefore, the distribution of the microstructures in the fractured EA tensile samples varies at different location. It is not fair for the *ex situ* experiments to compare the microstructures at different locations with respect to the fracture location under different processes.

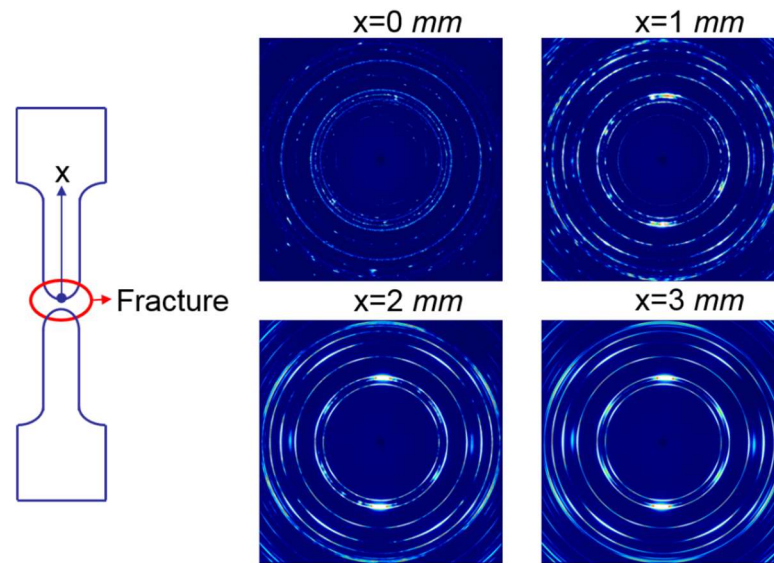


Figure 5.10 *Ex situ* XRD patterns for electrically-assisted tension specimen at different locations just after fracture (initial continuous current with density of  $17.5 \text{ A/mm}^2$ )

From the macroscopic mechanical outputs and microstructural evolution under electro-thermo-mechanical loading processes, no evidence of athermal effects of pulsed currents have been found in the low and medium temperature groups. In the high temperature group, more information on strain value is needed to draw a conclusion. Additionally, *ex situ* experiments need to be carefully examined to study the difference among different energy inputs.

## 5.5 Microstructure evolution under pure thermal condition

### 5.5.1 *In situ* XRD study in annealing conditions

A commercial Linkam heating stage (Figure 5.11) is used for this *in situ* X-ray diffraction study. Unlike the previous *in situ* XRD experiment, this section focuses on the microstructural changes under only thermal annealing conditions. The sample was machined to have a  $3 \text{ mm}$  by  $3 \text{ mm}$  size and placed in the center of the Linkam stage. The samples were gradually heated from

room temperature to 1,050 °C with 3 °C/min ramp rate in a constant N<sub>2</sub> flowing environment. An X-ray image was recorded every 1 min. Following the above method, the fitting was performed on the three representative peaks to extract the peak position, width and area.

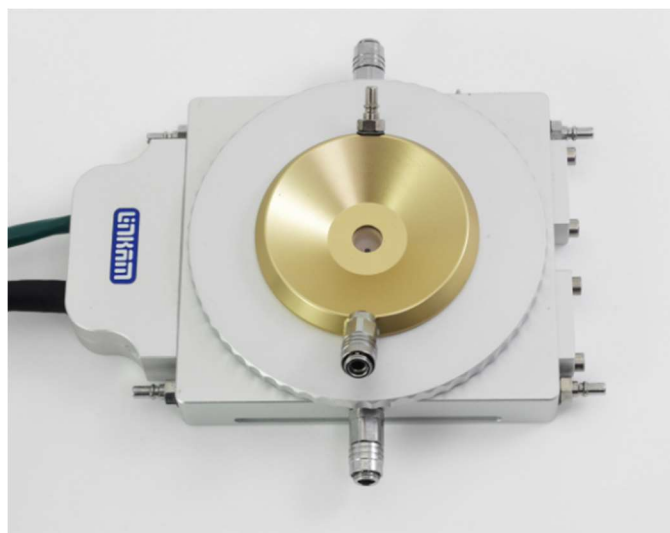


Figure 5.11 Linkam heating stage

The *in situ* XRD results together with fitted curves are plotted in Figure 5.12. During pure heating without deformation, the  $\beta$  phase fraction remains constant from room temperature to 480 °C. It rises drastically at higher temperatures. This correlates well with the *in situ* measurements under tensile loadings. In the low temperature group, the  $\beta$  phase fraction remains constant. Similarly, during the tensile tests in the medium temperature group, the  $\beta$  phase fraction remains unchanged before necking when the temperature is around 480 °C. As temperature increases after necking, the fraction of the  $\beta$  phase increases as well. Therefore, the temperature histories of the EA tensile tests using continuous currents in the medium temperature group and the high temperature group were substituted into the fitted curves. The measured  $\beta$  phase fractions in these EA tensile tests together with the predicted values predicted based on the annealing conditions are compared in Figure 5.13. From the results, it can be observed that the microstructural responses in

the electro-thermo-mechanical loading states differ from the annealing states under the same temperature history. Both the plastic deformation and the rapid heating rate in the EA tensile tests (regardless of different current patterns) may cause phase fractions to differ from the slow heating condition.

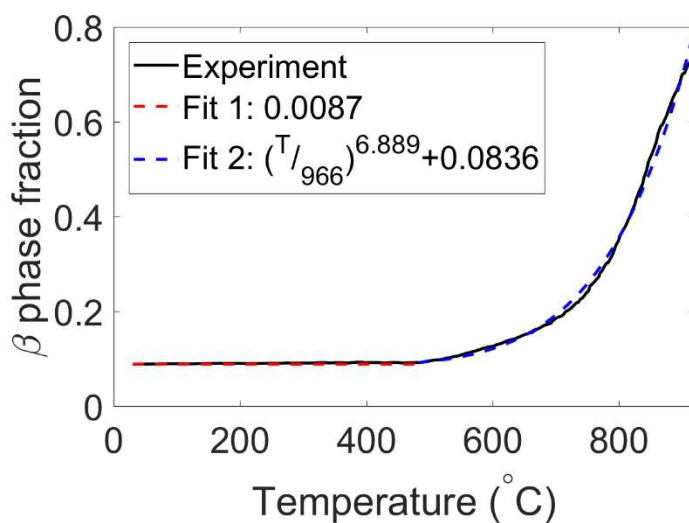


Figure 5.12 *In situ* XRD measurements of  $\beta$  phase fraction evolution during heating

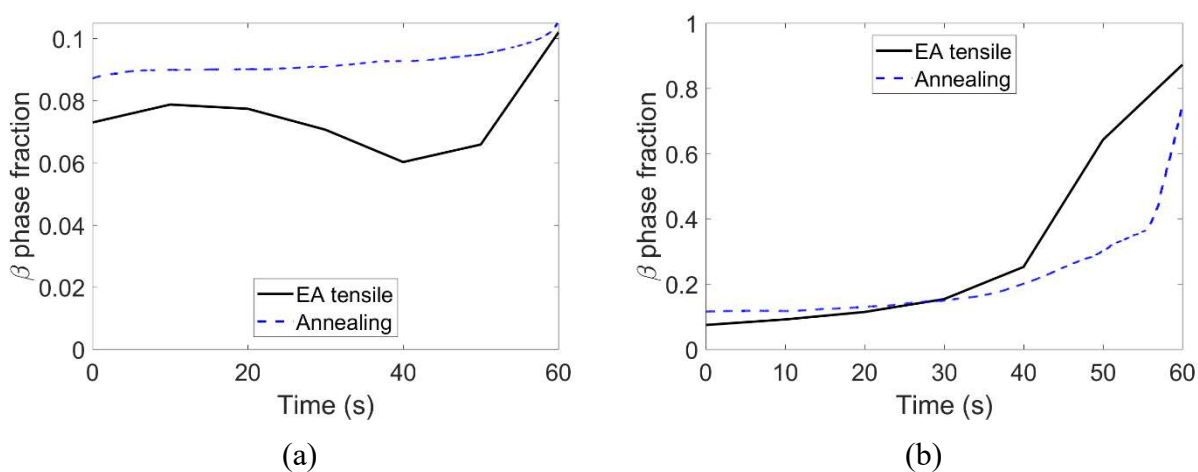


Figure 5.13 Fraction evolution of  $\beta$  phase measured in EA tensile tests and predicted based on annealing condition for: (a) medium temperature group; (b) high temperature group

### 5.5.2 Kinetic simulations for diffusion-based phase transformation

Kinetic simulations of the phase transformation were performed using DICTRA, the diffusion module in the Thermo-Calc software package, to further discuss the microstructural evolution in the rapid heating stage. The input temperature histories were the same as those measured in the EA tensile tests with continuous currents in both the medium and high temperature groups. This work was carried out in collaboration with Fuyao Yan.

The input parameters for the material were determined using energy-dispersive X-ray spectroscopy (EDS). The material was polished till using  $0.05 \mu\text{m}$  polisher. Then SEM 3400 was utilized to measure more than 10 sites on both the rolling-transverse and rolling-thickness planes. The backscattered SEM image of this material is illustrated in Figure 5.14. The black area represents the  $\alpha$  phase and the white area represents the  $\beta$  phase. With identified locations of both phases, the compositions of the entire material and of each phase were measured and listed in Table 11, Table 12, and Table 13.

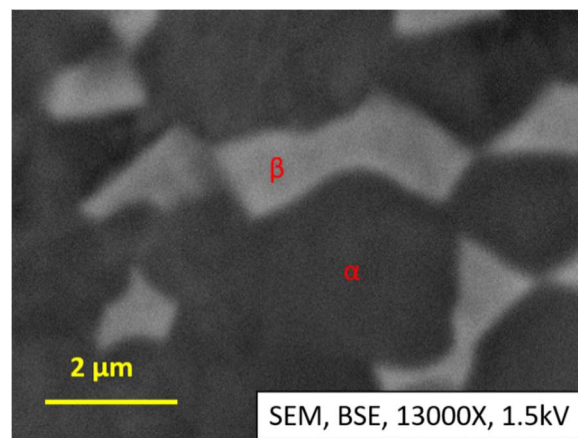


Figure 5.14 Backscattered SEM image of as-received Ti6Al4V

Table 11 Composition of as-received Ti6Al4V determined by EDS

Weight (%)				Atomic (%)			
Statistic	Al	Ti	V	Statistic	Al	Ti	V
Max	6.13	90.25	4.94	Max	10.41	86.35	4.46
Min	5.79	89.27	3.64	Min	9.87	85.67	3.28
Average	6.02	89.92	4.06	Average	10.23	86.11	3.66
Standard Deviation	0.14	0.31	0.41	Standard Deviation	0.22	0.24	0.38

Table 12 Composition of  $\beta$ -Ti determined by EDS

Weight (%)					Atomic (%)				
Statistic	Al	Ti	V	Fe	Statistic	Al	Ti	V	Fe
Max	4.46	84.12	16.32	2.64	Max	7.72	81.93	15.16	2.23
Min	3.28	77.96	10.14	1.28	Min	5.75	77.02	9.29	1.07
Average	3.76	80.49	13.68	2.07	Average	6.56	79.06	12.64	1.74
Standard Deviation	0.33	1.44	1.49	0.31	Standard Deviation	0.55	1.13	1.42	0.26

Table 13 Composition of  $\alpha$ -Ti determined by EDS

Weight (%)				Atomic (%)			
Statistic	Al	Ti	V	Statistic	Al	Ti	V
Max	6.87	91.37	3.32	Max	11.59	87.23	2.98
Min	5.94	90.4	2.15	Min	10.1	86.15	1.93
Average	6.4	90.93	2.67	Average	10.85	86.76	2.39
Standard Deviation	0.21	0.25	0.26	Standard Deviation	0.33	0.3	0.24

Using more than 10 different backscattered SEM images, the grain size of the  $\beta$  phase averaged at  $0.72 \mu\text{m}$  with a standard deviation of  $0.25 \mu\text{m}$  over the measured 150 sites. The average value

of the diffusion size was  $1.60 \mu\text{m}$  with a standard deviation of  $0.12 \mu\text{m}$ . The initial phase fraction was determined as 0.0828 with a standard deviation of 0.0108 when the total area of the  $\beta$  phase in the image was divided by the entire area of the image. It is identical with the value measured by XRD.

The simulation results are plotted in Figure 5.15. They both show a reduction in the  $\beta$  phase fraction before the end of the heating process. This is because the equilibrium value at that temperature is lower than the initial value. The heating process increases the mobility of the atoms and hence the boundary moves towards its equilibrium state. As temperature increases beyond the corresponding temperature of the current  $\beta$  phase fraction, the fraction increases back to match the equilibrium state at the elevated temperature. The kinetic simulation underpredicts the phase fraction compared to the values in the EA tensile tests. This could be explained by the omission of plastic deformations.

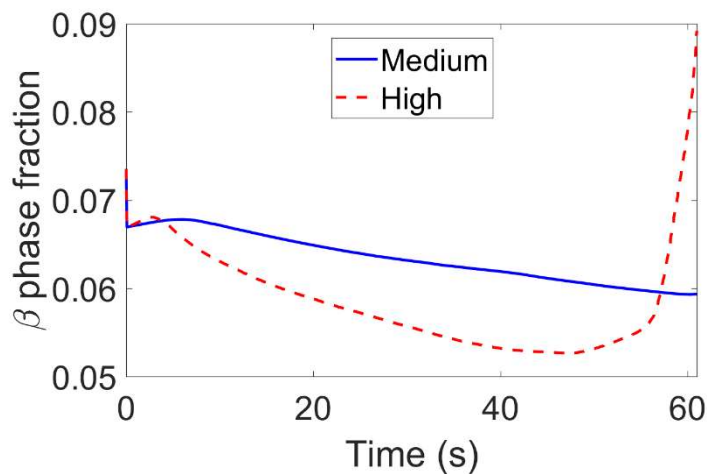


Figure 5.15 Simulated  $\beta$  phase fraction using DICTRA

## 5.6 Summary

This chapter presents *in situ* measurements of the microstructural responses under macroscopic electro-thermal-mechanical loadings. At the same temperature under 480 °C, it has been found that the EA tensile tests with pulsed and continuous currents show the same macroscopic tensile behavior and microstructural evolution. Therefore, the existence of electroplastic effects as part of the deformation mechanisms in the electro-thermo-mechanical processes has been denied. Additionally, the  $\beta$  phase fraction has been found to be not only dependent on temperature, but also on plastic strain and heating rate. Although the forming temperature in EA-DSIF processes does not reach the high temperature range, future studies of the deformation mechanisms in the high temperature range need to be carried out.

The results can be utilized to accurately predict the mechanical behavior of the material under coupled electro-thermo-mechanical loadings. They can be utilized to study any electrically-assisted manufacturing processes for Ti6Al4V. Although this study is for Ti6Al4V only, the methodology of identifying athermal effects can be extended to other materials as well.



## **Chapter 6: Enhancement of material properties through EA-DSIF processes**

Hybrid incremental sheet forming processes including MDSIF and EA-DSIF methods have been developed and studied in the first few chapters to achieve improved part geometry, process efficiency, and process capability to deform hard-to-form materials. The dominant deformation mechanisms in EA processes have been identified in the previous chapter. However, the microstructures and material properties of the deformed parts have not been examined yet. Therefore, this chapter discusses the effects of the electro-thermo-mechanical processes on the microstructural features and material properties of the formed parts. A microstructural investigation on the fracture surface is performed first to understand the fracture mechanisms. Then, micro-hardness tests are performed to study the competing softening and hardening effects within the process. Additionally, the surface topography is examined to assess the process. The combined factors of surface condition, tensile strength (which is indicated by hardness), and residual stresses determine the fatigue behavior of the processed material. Taking all these factors into account, the fatigue life of the processed material is analyzed.

### **6.1 Formability**

In this section, the characteristics of fractures in Ti6Al4V sheets deformed with EA-cDSIF are investigated and correlated to the stress state characteristics of the parts during the process. Due to the limited material formability of Ti6Al4V at room temperature, EA-cDSIF was performed under different current intensities, and the resulting fracture surfaces were investigated by means of Scanning Electron Microscopy (SEM) observations. To classify the fracture characteristics and

identify the corresponding stresses leading to failure in EA-cDSIF, tests with simpler stress states, i.e., uni-axial tensile and pure shear, were also carried out at different temperatures. The comparison of the related fracture surfaces demonstrates the prominent contribution of the shear effect in EA-cDSIF. Furthermore, the fracture mechanisms in EA-cDSIF were analysed, proving that Mode I (tearing) was responsible for the occurrence of fracture and that cracks start from the outer surface of the sheet.

### ***6.1.1 Investigation of fracture mechanics in EA-cDSIF***

The incremental and localized nature of the deformation process in EA-ISF, which depends on different factors, namely tool motion, material properties, lubrication and thermal effects, results in a complex material deformation behaviour (Fang et al., 2014), which was widely studied in the case of SPIF (Jackson and Allwood, 2009, Malhotra et al., 2012b, Smith et al., 2013), but in a limited manner for DSIF. Among these, Lu et al. (Lu et al., 2015a) developed an analytical model based on stress state analysis, evaluating experimentally the fracture mechanism as a function of two different forming parameters, i.e., the relative position of the forming and supporting tools and the supporting force. Moser et al. (Moser et al., 2016a) evaluated, through FEM simulations, the evolution of the triaxial state of deformation for an innovative part geometry, looking for qualitative relations between the process mechanics and the final geometric properties.

Since the deformation mechanics strongly influences the material's formability (Malhotra et al., 2012b), as demonstrated in the SPIF application cases, where damage accumulation was proven to be dominated by local bending and through-the-thickness shear (Jackson and Allwood, 2009), the current work aims at providing a deeper understanding of the fracture mechanisms in EA-cDSIF through fractographic observations. With this goal, the fracture surfaces of Ti6Al4V

parts were investigated through Scanning Electron Microscopy (SEM) and then examined to evaluate their dependence on the applied current intensity. The fracture characteristics were compared with the ones resulting from tests carried out under similar process conditions but with simpler stress states, namely uni-axial tensile and pure shear loading conditions. Furthermore, an accurate analysis of the stress state arising in the EA-cDSIF forming strategy was performed to identify the fracture mode controlling the fracture occurrence and its point of origin.

To investigate the effect of the stress mechanics on material failure behaviour, uni-axial tensile and pure shear tests were performed by straining the samples until fracture. The tensile tests as well as the pure shear tests were carried out on samples cut along the rolling direction with geometries illustrated in Figure 6.1a. Both tests were performed using a universal 5t MTS™ testing machine housed at the University of Padova, which was equipped with an induction heating system shown in Figure 6.1b. During the tests, the samples were heated up to the testing temperature, which was monitored through a K-type thermocouple spot-welded on their central area. After a soaking time of 30 s, they were strained maintaining the temperature of the gauge length constant. The samples were cooled in calm air after fracture. A summary of all the experiments, with the details of the process parameters, is reported in Table 14. This work was carried out in collaboration with Beatrice Valoppi from University of Padova.

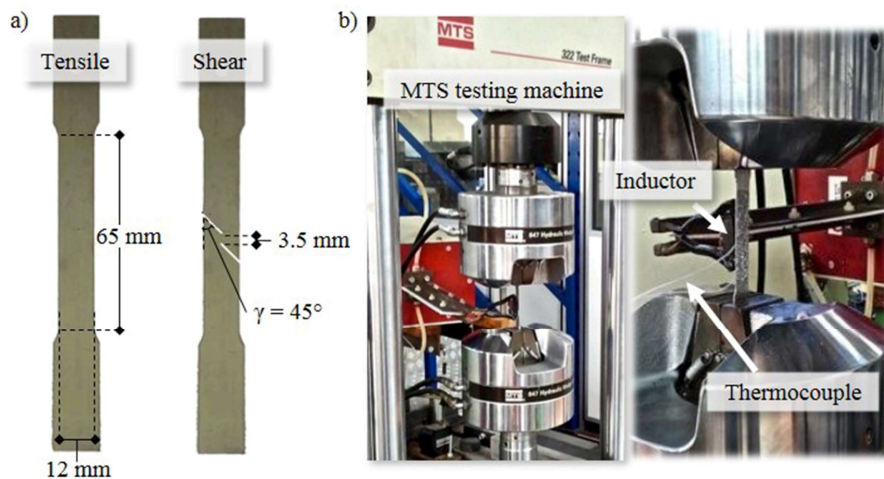


Figure 6.1 (a) Sample geometries for the uni-axial tensile and pure shear tests; (b) MTS™ testing machine and details of the induction heating system

Table 14 Summary of the experiments and process parameters

Test	I			Temperature			Strain rate	Strain
	[A]	[A]	[A]	[°C]	[°C]	[°C]		
E-DSIF	50	87.5	100	-				Fracture
Tensile	-			200	600	800	0.1	Fracture
Shear	-			200	600	800	0.1	Fracture

To carry out the fractographic analysis, the fracture surfaces of all samples were observed using SEM. During these analyses, the samples were placed in a manner to have the fracture area perpendicular to the SEM electron beam. The temperatures of the tensile and shear tests were determined using the colour comparison method described in Section 4.3.3.

### ***6.1.2 Results and discussion***

Figure 6.2 shows an overview of the fracture surfaces of the EA-cDSIF samples, obtained by using different current intensities. The first row shows the fracture surface of the sample deformed by applying the lowest current intensity, namely 50 A, which resulted in the smallest forming depth, as it can be observed in Figure 4.5. In the zoom of the green boxes, two different areas can be identified based on their features. One half of the fracture surface, related to the inner surface of the sheet, shows dimples similar to the ones of the ductile fracture under tensile stresses (Handbook, 2001), while the other half, close to the outer surface (the surface in contact with the bottom tool), presents small, partially formed dimples typical of shear conditions. At the inner side of the part, the top tool pushes the material downward making the tensile stress predominant, while, at the outer side, the circumferential movement of the bottom tool and the related shear effect generate the shear-type surface fracture.

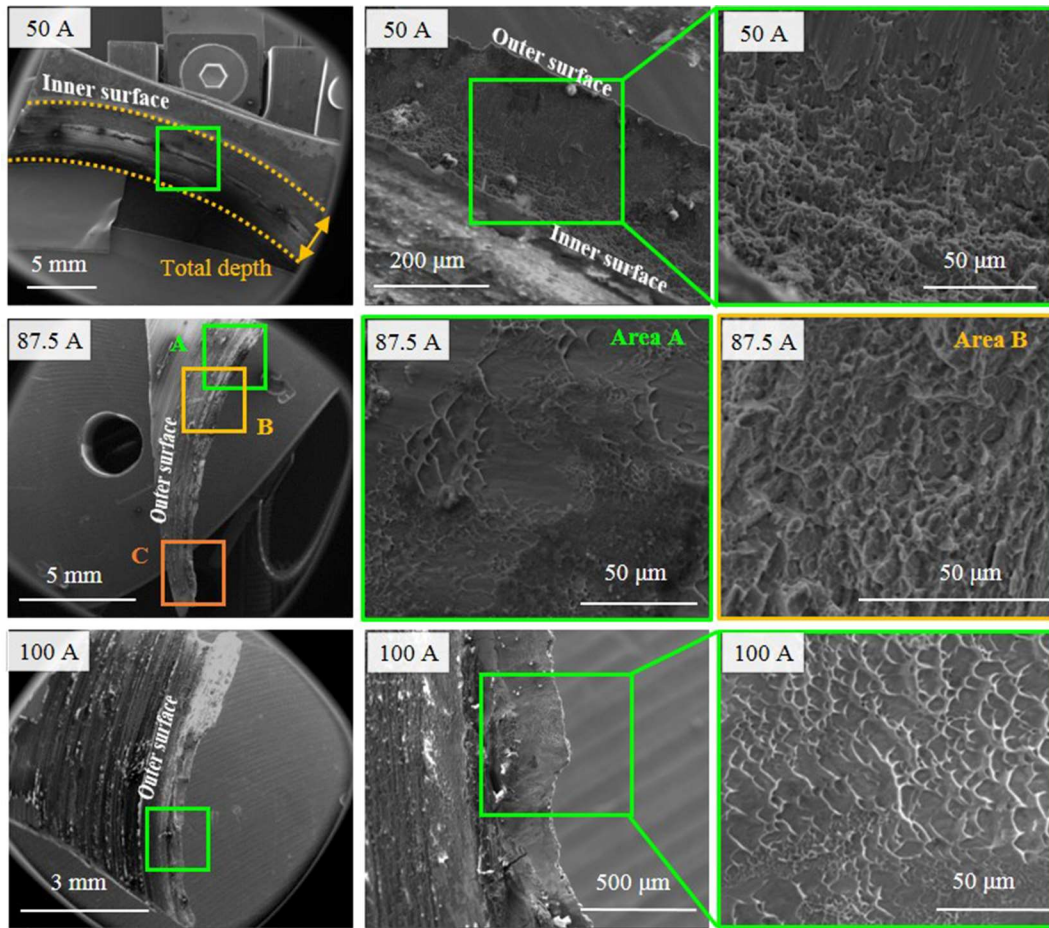


Figure 6.2 SEM images of the EA-cDSIF samples at 50 *A*, 87.5 *A*, and 100 *A*, specifying the inner and outer surfaces of the sheet, and some details of the fracture surfaces

Moving to the sample deformed by applying the medium amperage value of 87.5 *A*, which increases the part's achievable forming depth compared to the previous test, the analysis of the fracture surface reveals three areas, named A, B and C as reported in Figure 6.2, because different characteristics along the sample were identified. Indeed, as it can be seen in Area A which has an aspect typical of the shear ductile fracture (Handbook, 2001), where the partially formed dimples point towards the outer surface, Area B shows dimples similar to the ones of the ductile fracture under tensile stresses, while Area C shows a faceted surface, typical of brittle fracture. Considering

that the ductile-type and brittle fracture surfaces are placed one after the other in the circumferential direction, it can be stated that the fracture starts as ductile, and then propagates along the tool motion direction until the laceration of the sample, provoking a brittle fracture. This is in agreement with (Fang et al., 2014), where, in SPIF experiments, the fracture is first stretched due the meridional tensile stresses, which are operative also in the DSIF strategy (Lu et al., 2015a) because of the downward movement of the tool, and then expanded in the tool motion direction. It is worth to underline that the sample deformed by applying 50  $A$  does not present any brittle fracture, as the total forming depth was very low, namely fracture occurred very early to prevent any laceration of the sample.

Similar shear conditions characteristics in terms of small, partially formed dimples orientated towards the outer surface, were also found in the EA-cDSIF 100  $A$  sample (Figure 6.3). This analogy in the fracture surface features is associated with the fact that, compared to the EA-cDSIF test carried out at 50  $A$ , the increase of the total forming depth recorded for the test at 100  $A$  is similar to the one that resulted for the E-DSIF 87.5  $A$  sample.

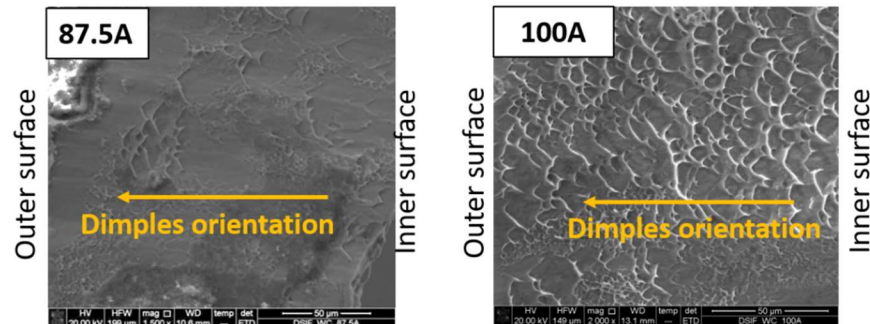


Figure 6.3 Partially formed dimples oriented towards the outer surfaces in EA-cDSIF at 87.5  $A$  and 100  $A$

The characteristics found in the EA-cDSIF fracture surfaces are also in agreement with the results obtained from the tensile and shear tests, which are reported in Figure 6.4, performed under different testing conditions (see Table 14). As it can be noticed, the fracture surfaces of the specimens subjected to the uni-axial tensile stress at 200 °C and 600 °C are characterized by essentially 100% dimpled rupture. The same result can also be identified at the highest temperature based on the characteristic dimples that can be observed on the fracture wall. This is because the fracture surface in this case becomes a fracture line at 800 °C due to the significant necking that occurred during the test. On the other hand, the fracture surfaces of the shear tests are characterized by dimples that, after being formed, are dragged because of the load applied during the tests. Under shear conditions, no significant differences can be noted at different testing temperatures.

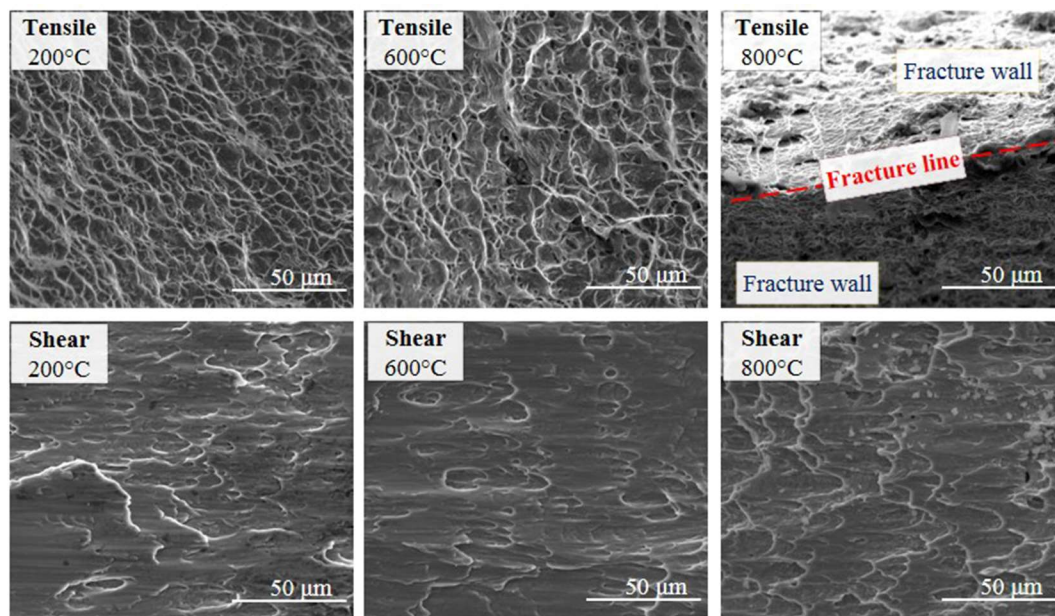


Figure 6.4 Fracture surfaces from heated tensile and shear tests

Based on the analytical model proposed by Lu et al. (Lu et al., 2015a) for the DSIF process, the deformation area in EA-cDSIF can be split into three zones, as represented in Figure 6.5a. Zone



I is the portion of the sheet that first comes into contact with the top tool; Zone II is the one that is squeezed between the two tools; Zone III is related to the part of the material that has been already formed by the two tools, but is still in contact with only the top tool. Therefore, Zone I and Zone III are characterized by tensile stresses in the meridional direction, since the material is in contact only with the top tool, without any squeezing effect from the bottom tool, while Zone II is a compressive area because of the pressure applied by the bottom tool in the radial direction.

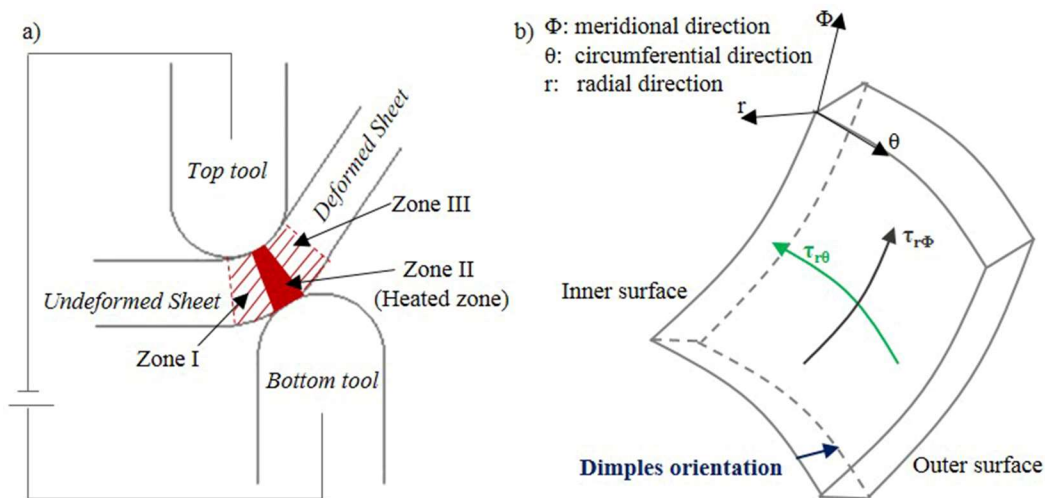


Figure 6.5 (a) Deformation zones in the E-DSIF process; (b) shear stress components in a small element through the thickness and detail of the dimple orientation

According to (Lu et al., 2015a), the pressure in Zone II postpones fracture occurrence due to the Drop Of Stress Triaxiality (DOST) phenomenon, meaning that fracture is not likely to initiate in this compressive area. Moreover, considering that in the EA-cDSIF process the tools-sheet contact area (Zone II) is heated through the Joule effect, which leads to an increase in the material's ductility as proven in (Valoppi et al., 2016), it is even less likely that fracture starts in Zone II. On this basis, it can be assumed that fracture starts in the area of the sheet that has been already formed

(Zone III in Figure 6.5a), which is characterized by a lower temperature and a reduced resistance section resulting from thinning in the radial direction. This is related to the negative strain in the radial direction that, considering volume conservation, results from the fact that convex shapes, such as the desired geometry in this study, lead to positive strain loading paths in the major ( $\epsilon_1$ ) vs. minor ( $\epsilon_2$ ) true strains space, as reported in (Soeiro et al., 2015). Based on the stress state analysis, thinning is caused by the tensile stress operating in the meridional direction.

Zone III, which is in contact only with the top tool as in SPIF (Malhotra et al., 2012b), beside the tensile stresses, is subjected also to bending around the tool, causing the material at the outer surface to stretch more as compared to the material at the inner surface, thus resulting in a higher plastic strain on the outer surface. In the same zone, friction at the tool-sheet contact along the meridional and circumferential directions results in  $\tau_{r\phi}$  and  $\tau_{r\theta}$  tangential stresses, respectively, as represented in Figure 6.5b, the latter being more significant because the tool moves mainly in the circumferential direction. Moreover, considering the EA-cDSIF process, friction is amplified by the increase of the current amperage, since the oxide layer triggered by the electrical heating hinders the movement of the top tool, leading to an increase of  $\tau_{r\theta}$ . Because this through-the-thickness shear was recognized as the mechanism that allows increasing the forming limits in incremental forming operations (Allwood et al., 2007), its effect on the inner surface leads to a lower ductility on the outer surface of the sheet, thus raising the damage accumulation on this side. Therefore, since both the local bending and through-the-thickness shear intensify the damage on the outer surface, it can be concluded that fracture starts from this side.

The above results explain the reason for better formability in EA-MDSIF as well. Since less force is needed in the D-stage (the second forming stage of the EA-ADSIF pre-formed part)

compared to the pure EA-cDSIF process, decreased tensile stress in the meridional direction is obtained, causing fracture to be postponed or inhibited.

Apart from fracture surface analysis, Computed Tomography (CT) scanning was performed to study the bulk material as well. From Figure 6.6, voids pile up close to the fracture surface, indicating a drastic propagation of the ductile fracture during the forming process.

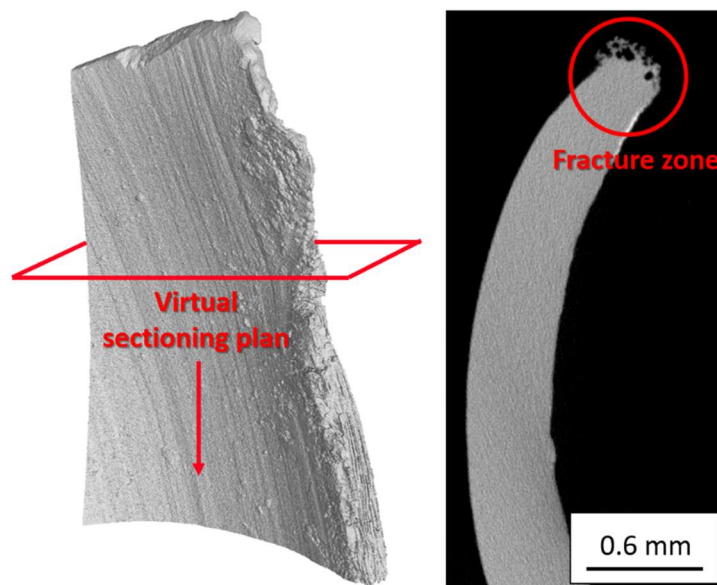


Figure 6.6 CT scan of the fractured EA-cDSIF 87.5 A part

Summarizing all the aforementioned aspects, it can be stated that fracture in EA-cDSIF occurs by progressive thinning of the sheet under tension, starting from the outer surface. Consequently, considering the conventional classification of fracture modes, fracture in EA-cDSIF can be classified as Mode I, or tearing. To note that tearing is considered as a conventional fracture mode also in SPIF (Madeira et al., 2015).

A further proof of fracture by tearing in EA-cDSIF is given by the orientation of the dimples. Indeed, as the dimples in the tearing fracture surfaces point towards the origin of fracture, the dimples in the EA-cDSIF fracture surfaces are orientated towards the outer side (Figure 6.3), which was demonstrated to be the starting point of fracture because of its higher damage.

In this study, the SEM analysis of the fracture surfaces enabled the characterization and identification of the fracture dependence on the applied current intensity. The mechanism and the origin of fracture in EA-cDSIF were also proposed on the basis of the stress states arising in the part during the EA-cDSIF process.

In summary, the following conclusions can be drawn:

- 1) Small, partially formed dimples characterizing the shear stress state can be observed on all the fracture surfaces of the EA-cDSIF parts. Moreover, the dimples point towards the outer surfaces at the higher current intensities. The related samples show similar fracture surfaces and comparable total forming depths.
- 2) The presence of ductile and brittle fracture surfaces along the sample in the horizontal direction suggests that fracture starts as a ductile crack and then propagates in the same direction until laceration of the sample occurs.
- 3) Fracture in EA-cDSIF is suggested to occur by progressive thinning of the sheet under tension in the part of the sheet already formed and in contact with the top tool, starting from the outer surface. Indeed, in this zone, the damage accumulation is higher on the outer surface because of the cumulative effect of local bending and through-the-thickness shear.

- 4) Fracture in EA-cDSIF is classified as Mode I, or tearing. As the dimples on the tearing fracture surfaces point towards the origin of fracture, the dimples on the EA-cDSIF fracture surfaces orientated towards the outer surface, further prove the aforementioned fracture mode and its point of origin.

On the basis of the aforementioned highlights, this section provides a starting point for the development and design of EA-cDSIF processes aimed at increasing formability. There are two future research topics: 1) lower the forming stress in the meridional direction such as performing EA-MDSIF process; and 2) improve the design of the supporting configuration (bottom tool) in order to increase the compressive stress in the zone just outside of the deformation zone or to expand the compressive area by, for example, adding an additional supporting tool.

## **6.2 Hardness**

During hybrid electro-thermo-mechanical forming processes, both hardening effects due to plastic strains and softening effects due to elevated temperatures coexist. Plastic strain is related to motion of dislocations, while hardening or softening is associated with interaction of dislocations. With the increase of dislocation density, the dislocations themselves get entangled and prevent further motion, which results in isotropic hardening. Recovery and recrystallization are two competing restoration mechanisms and they counteract the strain hardening (Babu and Lindgren, 2013). This section investigates the hardness of the material formed with the hybrid EA-ADSIF and EA-MDSIF processes.

To study the resulting hardness of EA-ADSIF and EA-MDSIF, the formed parts were cut at the central cross section to allow more characterization work, namely the surface roughness, the

microstructures and the micro-hardness. The micro-hardness tests were performed on a micro-durometer (Struers, model Duramin 5) and the reported results are the average values acquired along the thickness and far enough from the edges of the samples. The microstructures of the specimens revealed using the Kroll's reagent were analyzed along the thickness with an optical microscope (Nikon, model Optiphot-10). They were evaluated to examine any effect on the microstructural features that could be associated with the applied electric configurations.

The reported micro-hardness results (Figure 6.7) are the average values acquired along the thickness and at least 1 *mm* away from the edges of the samples. The increased hardness of the formed material in the baseline test (ADSIF formed without electricity) compared to the as-received material is mainly due to work hardening that occurs because during ADSIF repeated bending and unbending processes are taking place in a local area (Smith et al., 2013). The increased hardness between the EA-ADSIF 50 *A* and the baseline might be due to the secondary  $\alpha$  phase, which is harder than the primary  $\alpha$  phase, which was transformed from the  $\beta$  phase during cooling. The other factor for the increased hardness in EA-ADSIF 50 *A* may be the increased work hardening effects as the part is being formed with higher depth and wall angle as compared to the baseline case. Higher currents such as 100 *A* might have caused that the softening effects are more pronounced than the hardening effects. The annealing effect also explains why the micro-hardness drops in the case of 100 *A* after the initial increase from the as-received, to "Baseline", and to EA-ADSIF 50 *A*. Interestingly, comparing the EA-ADSIF to EA-MDSIF, both performed at 50 *A*, there exists a slightly positive increase of micro-hardness due to the two forming steps used in the MDSIF strategy.

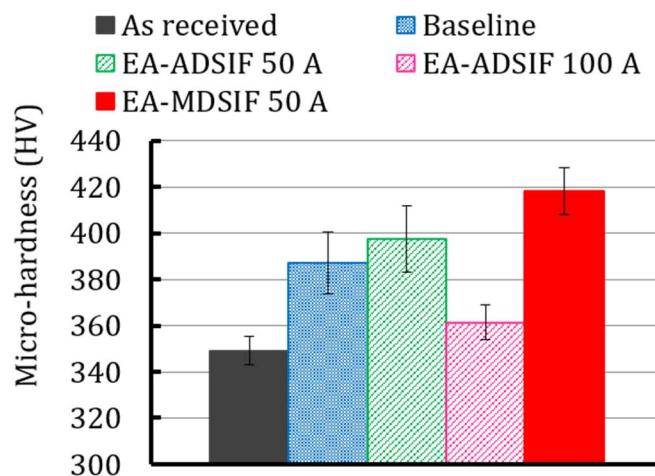


Figure 6.7 Material hardness of the formed parts

To further study the effects of increased electrical current intensity on the resulting microstructures and hardness, *ex situ* high-energy XRD measurements have been conducted to identify the phase fraction of the Ti6Al4V parts formed by EA-cDSIF. Selected results are shown in Figure 6.8. From the relative peak intensities of the two phases, the EA-cDSIF process reduced the composition of the  $\alpha$  phase and increased the composition of the  $\beta$  phase with an increase in the current intensity, which explains the reduced hardness in the 100 A case as compared to the 50 A case.

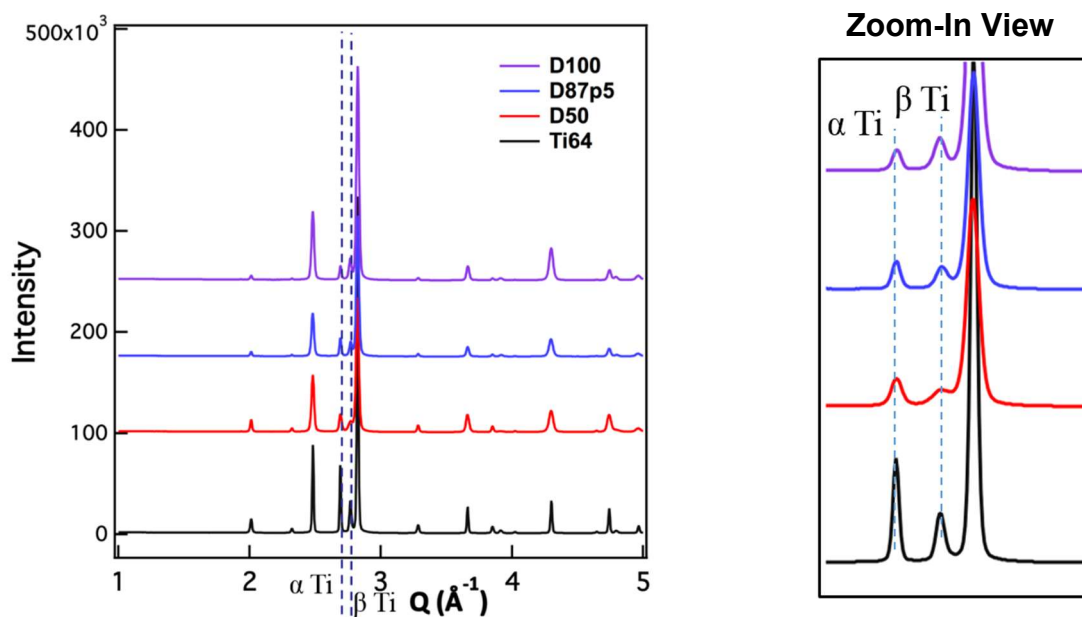


Figure 6.8 *Ex situ* high-energy XRD measurements of the EA-cDSIF samples

From the above study, it can be concluded that in order to achieve an optimal hardness of the formed material, the lowest current intensity capable of deforming the material to the desired depth is suggested.

### 6.3 Surface topography

Surface quality influences the final product in many aspects including appearance, interactions with other surfaces in contact, and other material properties. Since the surface condition, residual stresses, and the tensile strength have a significant effect on fatigue life of the materials (Hertzberg, 1989), it is worthwhile to examine the surface conditions of the ISF parts before evaluating the fatigue behavior of the formed parts. In this section, the effects of the material's initial states and strain levels under pure tension on surface topography are examined first to separate from the effects caused by process parameters. Then, surface appearance of the parts formed by different



ISF processes at room temperature is assessed through measured roughness and SEM observed topography. The impact of EA-related parameters including current intensity, toolpath strategy and tool material is discussed at the end.

### ***6.3.1 Effects of the material's initial states and strain levels***

The average surface roughness of the as-received material and of the formed parts,  $R_a$ , was measured with an optical surface profiler (Alicona, InfiniteFocus). The effects of the material's orientation with respect to the rolling direction and the strain level after pure tensile test were examined. The material was 1.64 mm thick AA 7075-O. Specimens were cut along both the rolling direction (RD) and transverse direction (TD). Uni-axial tensile tests were performed until excessive necking was observed before fracture. Due to necking, different strain levels within one sample were obtained. Strain increases with the decrease of its distance to the neck. The true strain levels at each location were estimated from the DIC measurement as shown in Figure 6.9. Surface roughness was determined by taking the average value of  $R_a$  measured with the Alicona optical microscope. Each measurement was repeated at least 3 times.

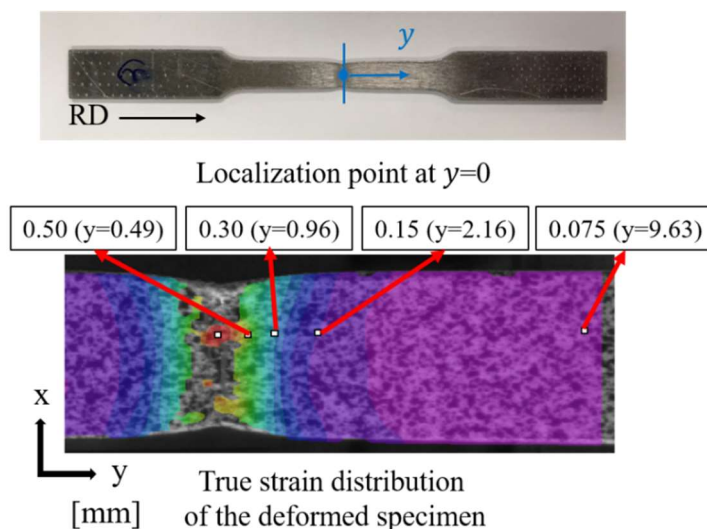


Figure 6.9 Identification of strain values in the pulled specimen

Note that waviness has been differentiated from roughness for the measurements. A surface may have irregularities at different scales. Waviness is a kind of roughness at a larger scale of observation. The resolution of the measurement instrument used for surface digitization and the parameters employed in the measurement determine the level of features to be observed. In the roughness measurement for both the as-received materials and ISF parts, filter length for roughness was set to be larger than  $\Delta Z/\sin\alpha$  to capture the effects of the forming process. The filter length for roughness in this section was set to be  $250\ \mu\text{m}$ .

Roughness measurement results are demonstrated in Figure 6.10. The roughness of the as-received material is plotted at zero true strain. All measurements were taken along the width direction as indicated by the red lines in Figure 6.10. Since roughness of the pulled specimen varies without a clear trend in the range of  $0.3\ \mu\text{m}$  to  $0.4\ \mu\text{m}$  regardless of orientation or strain level, it is found that the material roughness has little dependence on the orientation or the strain level. Therefore, the effects of the process parameters are investigated in the following sections.

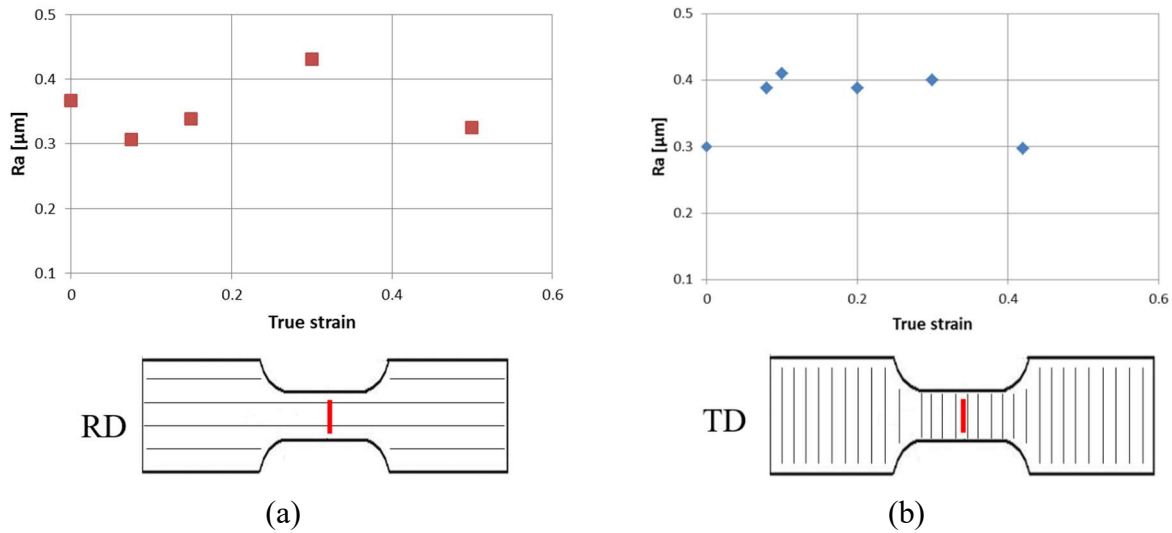


Figure 6.10 Roughness at different true strain values in tensile tests (redline indicates the direction of profile taken for roughness measurement)

### 6.3.2 Effects of toolpath strategy

To study the effects of toolpath strategy on the surface roughness of the formed parts, a B-shape geometry (left side in Figure 6.11) was formed by SPIF, DSIF, and ADSIF at room temperature. The material used in this case was 1.64 mm thick AA 7075-O, which is the same as that in the previous section. In SPIF, the top tool was set as the forming tool while the bottom tool moved along the circumference of the shape opening, performing as a backing plate. Other process parameters were kept the same in all three toolpath strategies. These parameters were set at tool diameter of 8 mm, contour tool path, incremental depth of 0.1 mm, tool speed of 5 mm/s, and zero additional squeeze ( $s = 1.0$ ). Forming forces were recorded during the forming processes. All roughness measurements were taken along the direction perpendicular to the tool marks to capture the effects of the forming process. The roughness of both the internal surface in contact with the

top tool and the external surface in contact with the bottom tool was measured. This work was conducted together with Dohyun Leem.

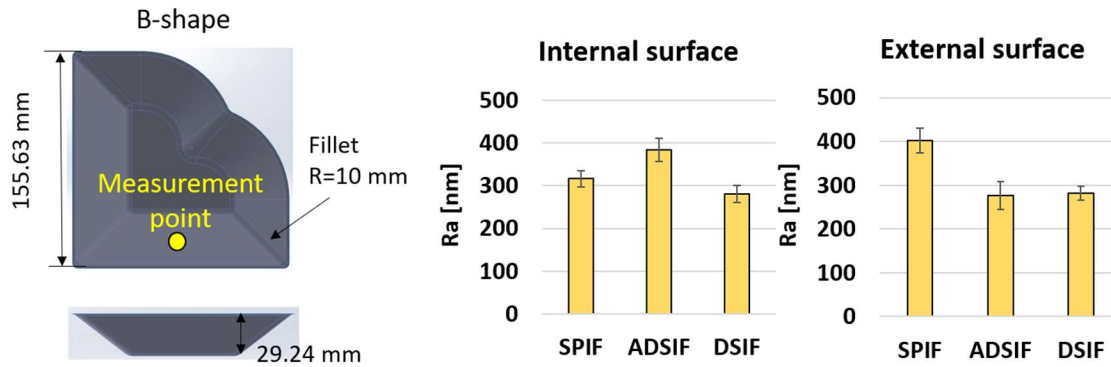


Figure 6.11 Roughness of parts formed with different toolpath strategies at room temperature

The measurement results are demonstrated in Figure 6.11. Comparing the roughness of the formed part with that of as-received material in Figure 6.10, no significant improvement or deterioration of the surface roughness has been found after the processes. However, the roughness value varies with different toolpath strategies. For the internal surface, ADSIF generates the roughest surface followed by SPIF and DSIF. On the other hand, ADSIF provides the smoothest external surface followed by DSIF and SPIF. This correlates well with the measured forming forces in different toolpath strategies. As the vertical forces were similar in different strategies, the recorded in-plane forces of different strategies are plotted in Figure 6.12. Note that in SPIF, the bottom tool performed as a backing plate without contacting the measured external surface of the part. Combining the forming forces with surface roughness results, a larger forming force may cause the surface to roughen for the internal surface. For the external surface, although a larger force increases roughness, the missing contact of the bottom tool leads to the deterioration of the surface.

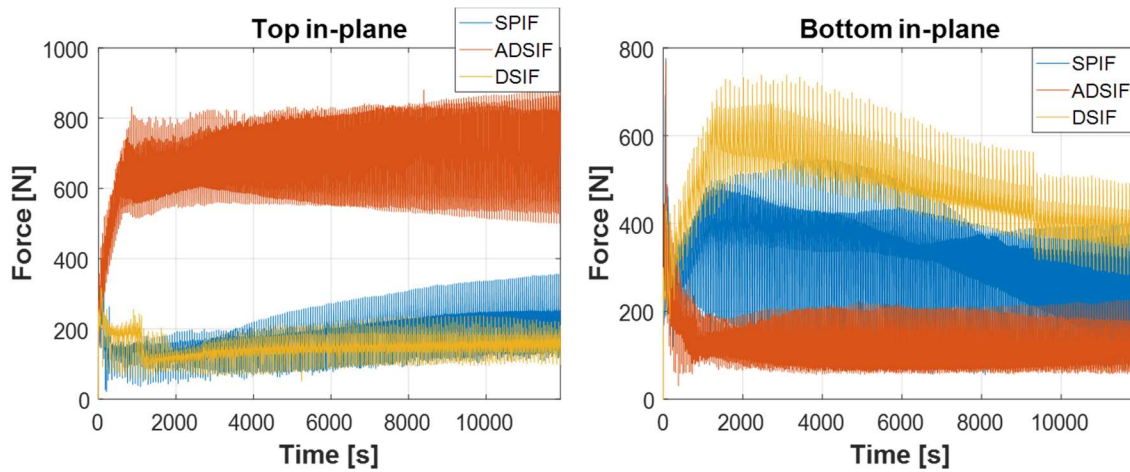


Figure 6.12 In-plane forces of forming the same geometry with different strategies

It can be concluded that the forming processes modifies the parts' surfaces. Although larger forming forces cause the surface roughness to increase, the loss of contact of the bottom tool which was the case in SPIF leads to higher roughening effects. Therefore, the surface characteristics were examined with SEM on two different DSIF parts, namely the Mountain Hat and Shamrock. The material and process parameters are given in Figure 6.13.

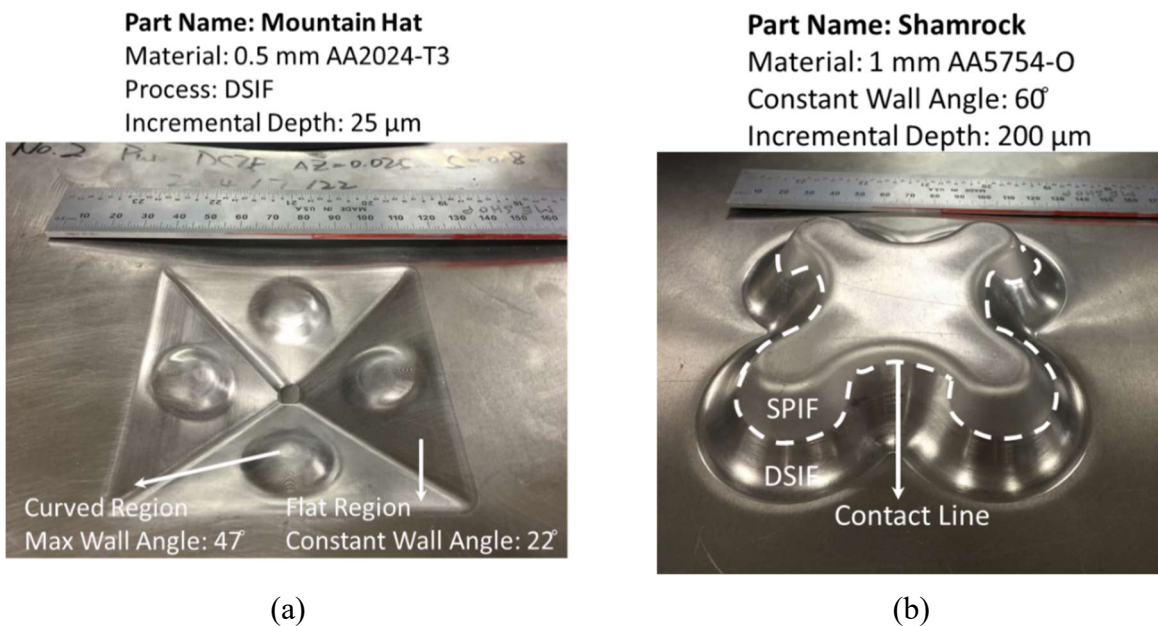


Figure 6.13 Specifications of: (a) Mountain Hat part; and (b) Shamrock part

Comparing the surface appearance of the curved region (Figure 6.14b and Figure 6.14d) with the flat region (Figure 6.14a and Figure 6.14c) on both internal and external surfaces, layered cracks are observed in the curved region where the deformation and force are higher than in the flat region. Additionally, deeper tool marks are noticeable on the internal surface of the flat region as compared to the external surface. This is because the forming force of the top tool is higher than that of the bottom tool in DSIF, which is indicated in Figure 2.13. However, more pronounced cracks are demonstrated in the curved region on the external surface (Figure 6.14d) than on the internal surface (Figure 6.14b). As it was discussed on the fracture mechanics in DSIF in Section 6.1, the stress state on the outer surface is higher than on the inner surface due to bending. The higher stress state facilitates crack formation on the outer surface in DSIF. The surface conditions of the Shamrock part are illustrated in Figure 6.15. This part was of interest because it contains both DSIF and SPIF features, separated by the contact line where the bottom tool lost contact and the process degraded from DSIF to SPIF. The cracks on the internal surface in Figure 6.15a exhibits compressed cracks along the tool direction, which may due to scratching from formed chips. The external surface in the DSIF region (Figure 6.15b) shows different topography compared to that in the SPIF region (Figure 6.15d). A smoother external surface with inhibited cracks perpendicular to the direction of tool motion is observed in the DSIF region while severe orange peel effects are generated in the SPIF region due to excessive necking of the material. This observation correlates well with the roughness measurement results in Figure 6.11. Therefore, it is beneficial to surface roughness to maintain contact between both tools and the material while reducing the forming forces as much as possible.

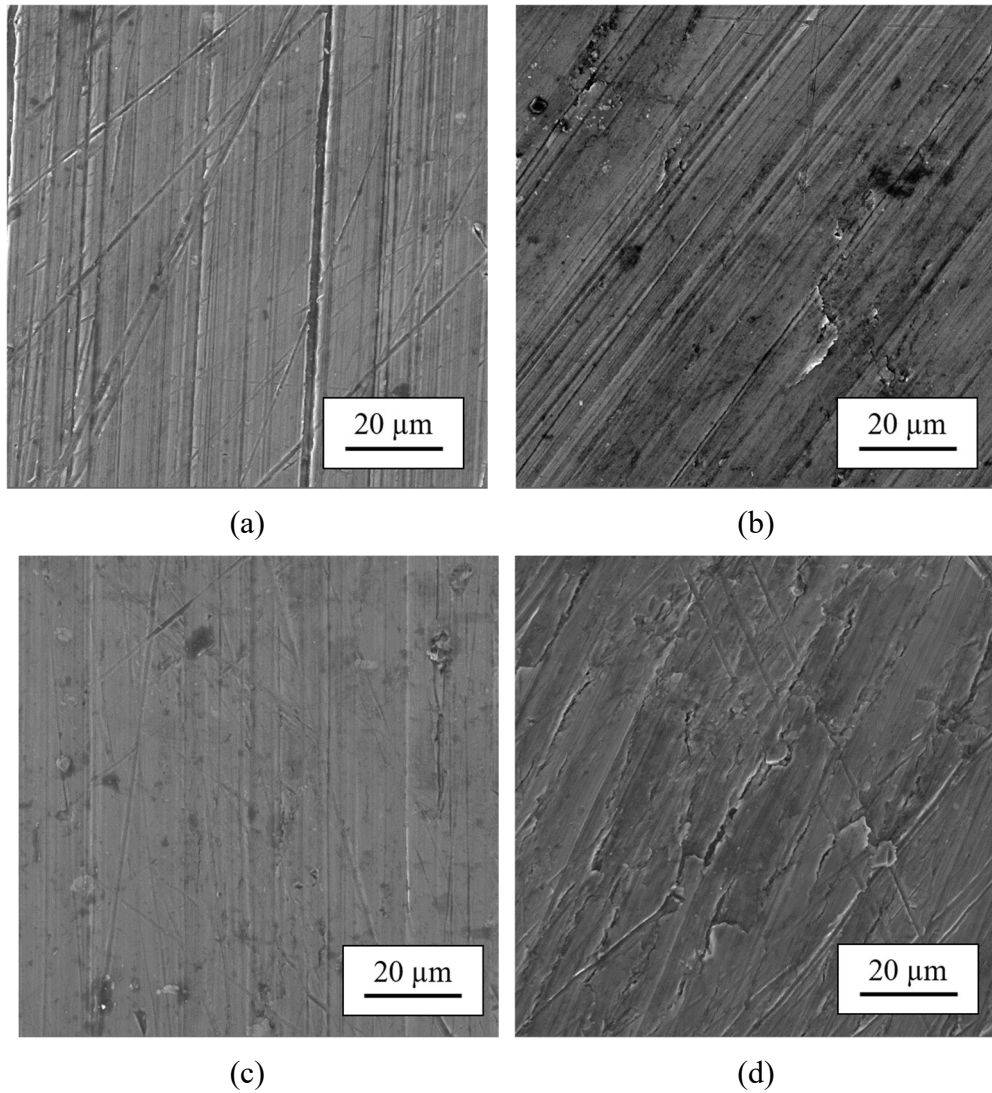


Figure 6.14 Surface topography of Mountain Hat examined with SEM (by Maya Nath from University of Michigan) on: (a) internal flat region; (b) internal curved region; (c) external flat region; (d) external curved region

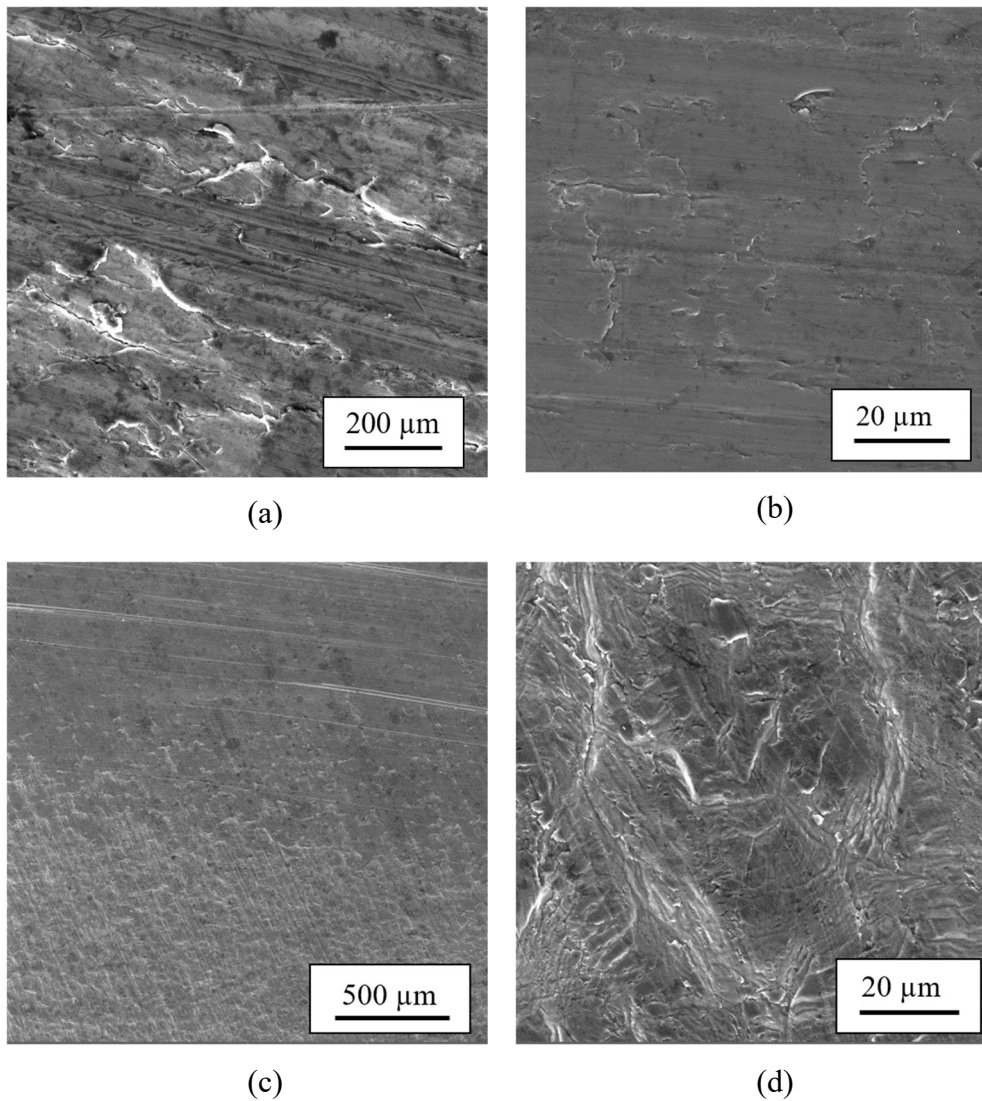


Figure 6.15 Surface topography of Shamrock examined with SEM (by Maya Nath from University of Michigan) on: (a) internal region; (b) external DSIF region; (c) external contact line region; (d) external SPIF region

### ***6.3.3 Effects of electricity and tool material***

The effects of toolpath strategy on surface topography has been studied in the earlier section. This section aims to investigate on the effects of electricity and tool material in EA-ADSIF and



EA-MDSIF. The parts formed in Chapter 4 have been examined through surface analysis in this section.

Figure 6.16 presents the surface roughness of the parts formed with EA-ADSIF and EA-MDSIF using tools made of A2 tool steel. It can be seen that even the sole ADSIF baseline process leads to increased surface roughness compared to the as-received sheet. The application of electricity makes the roughening effect even more significant, especially in the case of the internal surface. Indeed, a higher current intensity triggers the oxidization process on both internal and external surfaces, but the higher forming pressure applied by the top tool increases the roughening effect on the internal surface, i.e., removal of the oxide layer and, at the same time, increasing the average roughness (Smith et al., 2013). Concerning the effect of various forming strategies, EA-MDSIF, namely EA-ADSIF followed by EA-cDSIF in the second step, resulted in the highest values of the surface roughness. Although the rough surface generated by EA-MDSIF may be a challenge for some aesthetic purposes, it is advantageous in, e.g., biomedical applications where the surface plays a key role in the implant-bone interaction (Bagno and Di Bello, 2004). Indeed, it has been demonstrated that high surface roughness enhances the osseointegration process (Li et al., 2010). This makes the EA-MDSIF strategy suitable for biomedical applications where rougher surfaces provide better biocompatibility. Nevertheless, what if a smoother surface is desired? Severe tool damage is observed in the A2 tool case after EA-ADSIF 120 A was performed (Figure 6.17). Therefore, the effects of the material of the tool are investigated.

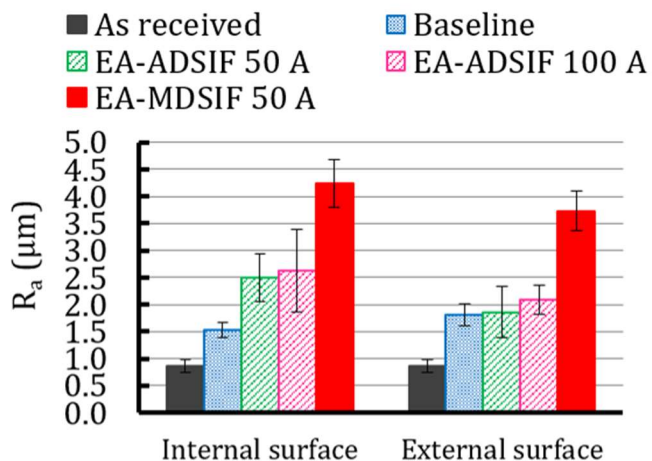


Figure 6.16 Surface roughness of the parts formed with EA-DSIF processes



Figure 6.17 Severe damage of A2 tool steel tool after one EA-ADSIF 120 *A* process

Two pairs of tools, one made of A2 and the other made of Tungsten Carbide, were examined after performing the same three EA-DSIF processes, including EA-ADSIF 50 *A*, EA-ADSIF 100 *A*, and EA-MDSIF 50 *A*. The microscopic images of the tungsten tools are demonstrated in Figure 6.18. It is noted that the machine marks on the tungsten tools almost disappear after the three

forming processes, but the overall condition of the tool is good without any visible damage. The roughness of the formed tools and parts is listed in Table 15. It is evident that tungsten tools outperform tool steel tools in resulting surface roughness. Although rougher part surfaces were generated by EA-MDSIF 50 *A* compared to the surfaces formed with EA-ADSIF 50 *A* using tools made of A2 tool steel, similar or even reduced surface roughness has been achieved by EA-MDSIF 50 *A* using the tungsten tool. This is because the surface treatment in the D-stage with reduced forming force is beneficial to the surface condition as discussed in the previous section. Therefore, depending on the desired application, different surface conditions can be achieved using different tool materials. Tool steel can be utilized to increase biocompatibility while tungsten can be utilized to increase the aesthetic value or other material properties.

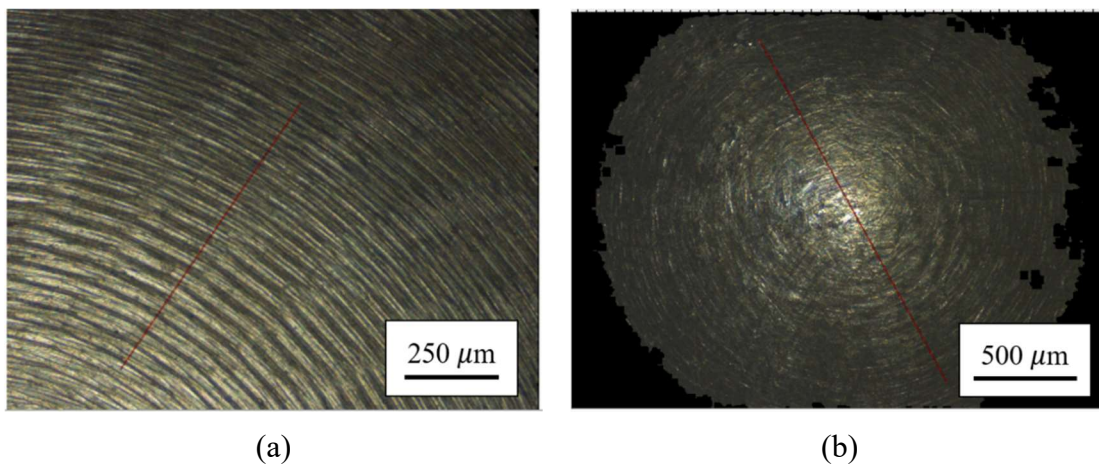


Figure 6.18 Microscopic images of tungsten carbide tool (top tool): (a) as-received ( $R_a = 0.88 \mu\text{m}$ ); (b) after 3 EA-DSIF processes ( $R_a = 1.5 \mu\text{m}$ )

Table 15 Surface roughness of parts formed with different EA-DSIF processes and forming tools made of different materials

• Tool	<b>Material</b>	<b>Upper Tool Ra (<math>\mu\text{m}</math>)</b>	<b>Bottom Tool Ra (<math>\mu\text{m}</math>)</b>
	Tool Steel	3.7118	3.5128
	Tungsten	1.4964	1.3708
• Part: MDSIF 50A	<b>Material</b>	<b>Inner Surface Ra (<math>\mu\text{m}</math>)</b>	<b>Outer Surface Ra (<math>\mu\text{m}</math>)</b>
	Tool Steel	4.2419	3.7357
	Tungsten	1.2496	0.8943
• Part: ADSIF 50A	<b>Material</b>	<b>Inner Surface Ra (<math>\mu\text{m}</math>)</b>	<b>Outer Surface Ra (<math>\mu\text{m}</math>)</b>
	Tool Steel	2.494	1.8610
	Tungsten	1.2336	1.2566
• Part: ADSIF 100A	<b>Material</b>	<b>Inner Surface Ra (<math>\mu\text{m}</math>)</b>	<b>Outer Surface Ra (<math>\mu\text{m}</math>)</b>
	Tool Steel	2.7309	2.2183
	Tungsten	1.3218	1.6324

Microscopic images of the surfaces of the ADSIF formed Ti6Al4V parts were examined. Surface cracks along the inner surface of the parts formed with conventional ADSIF were observed (Figure 6.19). However, in the EA-ADSIF parts, the surface cracks were eliminated by the thermal effects. Even with the lowest current intensity of 40 A, which only heated the part to around 50°C measured by the IR camera, no surface cracks were found on the surface of the parts. The baseline specimen shows several cracks along the profile of the internal surface orientated from the top to the bottom. These cracks were found in the middle part of the specimen, where the wall angle increases to 50° (Phase A indicated in Figure 4.13). In this specific region, the material, hardened by the previous plastic deformation, experiences a stretching condition. This stretch along with the reduction of the sheet thickness could be one of the reasons for the onset of these cracks. On the

contrary, no cracks were found in the electrically-formed specimens because the thermal contribution affects the material by releasing its internal stresses, similar to an annealing process. The thermal softening from the Joule effect prevented surface defects from crack propagation that could bring an early fracture or future fatigue failure.

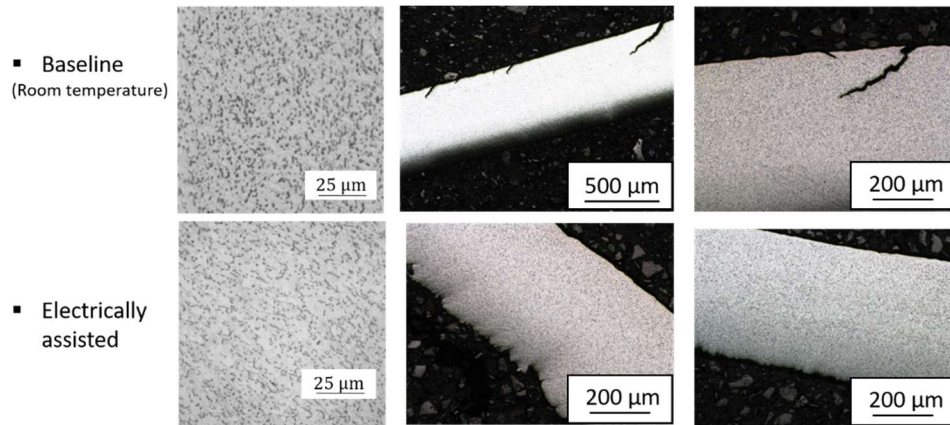


Figure 6.19 Microscopic images of surfaces on ADSIF formed Ti6Al4V parts

#### 6.4 Fatigue life

Fatigue is defined as a term applying to changes in properties which can occur in a metallic material due to the repeated application of stresses or strains, although usually this term applies specially to those changes which lead to cracking or failure. Moreover, this description is also valid for the fatigue of nonmetallic materials. Fatigue failure may happen under many circumstances. These failures generally take place under cyclic loads whose peak values are often lower than the safe loads or fracture loads (Suresh, 1998). Alternatively, manufacturing processes, such as shot-peening and autofrettage, which cause compressive surface residual stresses, can be applied to critical components to inhibit crack initiation and growth and enhance fatigue lifetimes (Hertzberg, 1989).

ISF is a localized/non-uniform deformation, where considerable residual stresses could be generated throughout the process. However, little work has been done on the direct study of residual stresses in ISF. Tanaka et al. examined the residual stress in the sheet metal part obtained by SPIF by numerical methods. The nonuniform residual stress distribution through the sheet thickness results in resultant moments throughout the sheet, which cause springback after the trimming process. They also concluded that the tool radius has a significant influence on the residual moment while the effect of tool feed rate is small (Tanaka et al., 2007). Radu et al. investigated the residual stress in SPIF experimentally by the hole-drilling method. A strong relationship between the geometric accuracy of the part and the state of the residual stresses induced by the working regime has been determined (Radu et al., 2013).

The effects of residual stress in ISF, namely, fatigue and springback, have also been barely studied. Since one of the most promising applications of incremental forming is in low volume production and prototyping of aerospace parts, fatigue life is a crucial issue and an important design constraint. However, research on fatigue behavior with respect to ISF is relatively rare. Agrawal et al. studied the fatigue life of a 90-degree bent part formed by conventional bending, SPIF and the deformation machining process, which is a hybrid process combining machining of thin-wall structures and SPIF. The reported fatigue life showed that under bending loads SPIF parts have significantly longer fatigue life, compared to parts fabricated with Deformation Machining and conventional bending (Agrawal et al., 2012). Rui et al. examined the fatigue life of parts formed with ADSIF under high frequency conditions and found that ADSIF prolonged the fatigue life as compared to the virgin AA2024-T3 material due to the compressive residual stress induced by the second forming tool (Xu et al., 2014b). However, the related stress analysis or

measurement was missing to support this opinion. Because of its importance and the lack of research in terms of residual stresses and their effects on materials formed with ISF, this section aims to analyze the fatigue life and residual stresses in ISF.

#### 6.4.1 Fatigue life measurements

Direct fatigue life measurements of the room temperature formed materials have been conducted. The testing specimens were cut from the wall of a pyramidal part (Figure 6.20) formed by the ISF process using different toolpath strategies according to ASTM E468-90. The tool diameter was 5 mm and the incremental depth was 0.1 mm. The material was 0.5 mm thick AA2024-T3. The fatigue tests were carried out on a MTS7 Servo-Hydraulic fatigue test machine, which provides tension-tension loading. This work was carried out with Rui Xu.

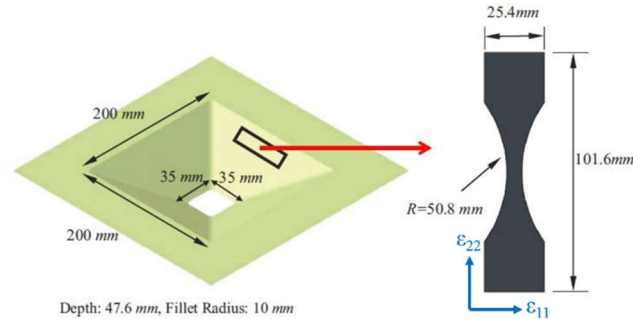


Figure 6.20 Specimen for fatigue tests (Xu et al., 2014b)

The typical S-N curve can be modeled as:

$$S_a = S'_f (2N_f)^b \quad \text{Eq. (12)}$$

where  $b$  is the fatigue strength exponent, and  $S'_f$  is the fatigue strength coefficient. This expression developed from log-log S-N plots is the most widely used equation which is known as Basquin's relation.

Preliminary work has been done to test the fatigue life of the virgin material, SPIF and ADSIF formed parts, and of the annealed part. The fatigue test results were fit using Basquin's equation (Figure 6.21). It was found that ADSIF prolongs the fatigue life of the material as compared to the virgin material, while SPIF reduces the fatigue life. This may be due to: (1) the compressive residual stresses imposed by the bottom tool in ADSIF; (2) work-hardening effects during the unique bending-unbending process in ADSIF; (3) increase of the fracture toughness by the ADSIF process. It should also be noticed that the annealed part has the shortest fatigue life within the same loading process. This might be due to the residual-stress relief effect during the annealing process that reduces the surface compressive residual stresses. It may also be by the material softening caused by the annealing process.

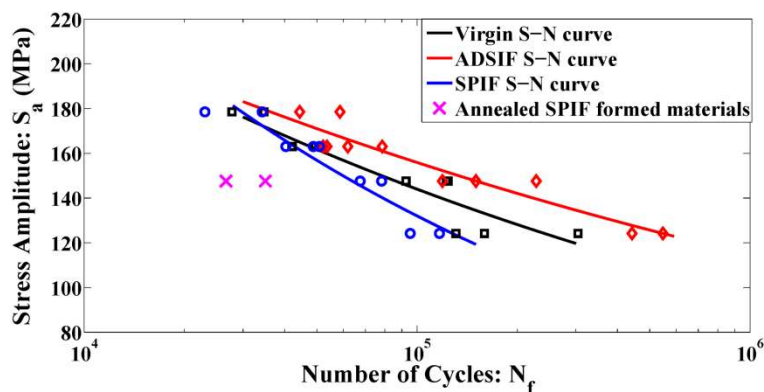


Figure 6.21 S-N curve of AA2024-T3 under cyclic tensile loading

To determine the reasons for the reduced fatigue life of the annealed part, hardness tests were carried out on the same pyramidal parts from which the fatigue specimens were cut from. Each experiment was repeated 5 times. The average values and the standard deviation of the hardness measurements are listed in Table 16. From the results, one can see that both ADSIF and SPIF increases material hardness, but ADSIF improves more. From the decreased hardness together



with the decreased fatigue life of the annealed material compared to the virgin material and SPIF material, it can be concluded that hardness plays a crucial role on determining fatigue life since the values of surface roughness are similar in ISF at room temperature as discussed in Section 6.3.2. It is noted that although SPIF generates slightly higher hardness than the virgin material, the fatigue life of the SPIF formed material is lower. This may be due to tensile residual stresses, which will be discussed in the next section.

Table 16 Micro-hardness of formed AA2024-T3 samples

Hardness (HV)	Virgin	ADSIF	SPIF	Annealed SPIF
Average	153.5	182.8	157.8	129.8
Standard Deviation	5.2	2.8	1.9	2.0

#### ***6.4.2 Residual stress measurements***

Residual stresses have been introduced in Section 3.6.1. The comparison between different common residual stress measurement methods are listed in Table 17. In general, the synchrotron X-ray diffraction method provides non-destructive measurements, high penetration depth and better spatial resolution. It is considered one of the best ways for residual stress measurements. This method is extremely suitable for this research because of its independence from surface condition. The complex 3D surface of ISF formed parts will cause difficulties and inaccuracy in other methods such as the hole-drilling methods and conventional X-ray diffraction (Kandil et al., 2001). Moreover, the capability of the diffraction method of measuring phase-dependent thermal

residual stresses (Type II stress) is beneficial to the study of the residual stresses in thermally-assisted processes.

Diffraction measures strain components from the changes in crystal lattice spacing. The fundamental relation is Bragg's equation:

$$2d_{hkl} \sin \theta_{hkl} = \lambda \quad \text{Eq. (13)}$$

where  $\lambda$  is the wavelength of the radiation,  $d_{hkl}$  is the lattice plane spacing of a family of crystallographic planes ( $hkl$ ) responsible for the Bragg peak and  $\theta_{hkl}$  is the angular position of this diffraction peak. The peak will be observed at an angle of  $2\theta_{hkl}$  from the incident beam. If a specimen is elastically strained, the lattice spacing will change. Therefore, any elastic strain will be apparent as a shift in the value of  $2\theta_{hkl}$  for a particular reflecting plane illuminated by a fixed wavelength. By differentiating the Bragg equation,

$$\Delta\theta_{hkl} = -\frac{\Delta d}{d_0} \tan \theta_0 \quad \text{Eq. (14)}$$

where  $\Delta d$  is the change of lattice spacing, and  $d_0$  is the lattice spacing of a stress-free sample of the material. So, the strain in the ( $hkl$ ) set of planes can be calculated from:

$$\varepsilon = \frac{\Delta d}{d_0} = -\Delta\theta \cot \theta_0 \quad \text{Eq. (15)}$$

The direction in which strain is measured is along the scattering vector and is perpendicular to the diffracting planes (Anderoglu, 2005, Hutchings et al., 2005, Noyan and Cohen, 2013).

Table 17 Comparison of the Residual Stress (RS) measurement techniques (Kandil et al., 2001, Schajer, 2013)

Technique	PROs	CONs
Hole Drilling	<ul style="list-style-type: none"> <li>• Quick, simple,</li> <li>• Widely available</li> <li>• Portable.</li> <li>• Wide range of materials</li> <li>• Deep hole drilling for thick section components</li> </ul>	<ul style="list-style-type: none"> <li>• Interpretation of data</li> <li>• Destructive</li> <li>• Limited strain sensitivity and resolution</li> </ul>
Curvature and Layer Removal	<ul style="list-style-type: none"> <li>• Relatively simple</li> <li>• Wide range of materials</li> <li>• Can be combined with other techniques to give stress profile</li> </ul>	<ul style="list-style-type: none"> <li>• Limited to simple shapes</li> <li>• Destructive</li> <li>• Lab-based</li> </ul>
Magnetic	<ul style="list-style-type: none"> <li>• Very fast</li> <li>• Wide variety of magnetic techniques</li> <li>• Portable</li> </ul>	<ul style="list-style-type: none"> <li>• Only ferromagnetic materials</li> <li>• Need to separate the microstructure signal from that due to stress</li> </ul>
Ultrasonic	<ul style="list-style-type: none"> <li>• Generally available</li> <li>• Very fast</li> <li>• Low cost</li> <li>• Portable</li> </ul>	<ul style="list-style-type: none"> <li>• Limited resolution</li> <li>• Bulk measurements over whole volume</li> </ul>
Neutron Diffraction	<ul style="list-style-type: none"> <li>• Excellent penetration &amp; resolution</li> <li>• 3D maps</li> <li>• Macro and micro RS</li> </ul>	<ul style="list-style-type: none"> <li>• Specialist facility only</li> <li>• Lab-based</li> </ul>
X-Ray Diffraction	<ul style="list-style-type: none"> <li>• Versatile, widely available</li> <li>• Wide range of materials</li> <li>• Portable systems</li> <li>• Macro and micro RS</li> </ul>	<ul style="list-style-type: none"> <li>• Basic measurements</li> <li>• Lab-based systems, small components</li> </ul>
Synchrotron	<ul style="list-style-type: none"> <li>• Improved penetration &amp; resolution of X-rays</li> <li>• Depth profiling</li> <li>• Fast</li> <li>• Macro and micro RS</li> </ul>	<ul style="list-style-type: none"> <li>• Specialist facility only</li> <li>• Lab-based</li> </ul>

The residual strains (Figure 6.20) were measured in the SPIF and ADSIF parts at the same position of the fatigue samples using the XRD method (Table 18). The X-ray beam penetrated from the center of the specimen through the thickness direction of the part, so that in-plane strain information was gathered. It was assumed that the material was isotropic with a Young's modulus of  $E = 73 \text{ GPa}$  and Poisson's ratio  $\nu = 0.33$ . The surface of the part was free of stress, so a plane-stress condition was assumed ( $\sigma_3 = 0$ ). The residual strains and stresses were related through:

$$\sigma_{22} = \frac{E}{1 - \nu^2} [\nu \varepsilon_{11} + \varepsilon_{22}] \quad \text{Eq. (16)}$$

Table 18 Residual stress measurement results

Process	Residual Strain $\varepsilon_{11}$	Residual Strain $\varepsilon_{22}$	Residual Stress $\sigma_{22}$
SPIF	$6.33 \times 10^{-4}$	$7.45 \times 10^{-5}$	23.2 MPa
ADSIF	-0.0018	-0.0027	-269.8 MPa

From the residual stress measurement results, it was confirmed that the ADSIF process provides compressive residual stresses which are beneficial for the fatigue life of the parts, while small amounts of tensile stress were generated through the SPIF process which weakens fatigue performance. These results correspond well with the fatigue life measurements. Due to the eliminated surface cracks and increased hardness, which is often considered as an indicator of the tensile strength, it is reasonable to believe that the fatigue life of the electrically-assisted formed material is better than that of the material formed at room temperature.

## 6.5 Summary

This chapter first investigated the fracture characteristics of Ti6Al4V sheets formed with EA-cDSIF and identifies the fracture mode as Mode I. It also locates the fracture's point of origin at the outer surface. Due to the reduced forming forces in the meridional direction in the D-stages, MDSIF and EA-MDSIF are able to achieve improved material formability.

Hardness of the material processed by EA-DSIF methods has been evaluated. Competing effects of work-hardening due to plastic deformation and thermal softening due to elevated temperature have been found. The lowest possible amperage capable of deforming the material to the desired depth is suggested to achieve optimal hardness.

Additionally, a strong dependence on toolpath strategy, tool material, and current intensity has been found in the ISF processed parts. Processes with decreased forming force are beneficial to surface quality. Processes using tungsten tools and low current intensities generate smoother surfaces. Additionally, a better surface condition has been found in EA-DSIF processes compared to the Ti6Al4V parts formed without electricity at room temperature.

Finally, fatigue life has been studied in ISF. Materials processed with ADSIF exhibit improved fatigue behavior compared to those processed with SPIF and the as-received materials. Residual stresses of the parts have also been measured using high-energy XRD. Compressive residual stresses, which are beneficial to fatigue life, have been found in ADSIF. Since little work has been done to evaluate the fatigue life or measure the residual stresses in ISF parts, the results provide missing knowledge in this field. Additionally, these residual stress measurements will be critical for the verification of future simulations.

## **Chapter 7: Summary and future directions**

This chapter presents a brief summary of the thesis work and its key findings. Insights on future directions for research and remaining issues are also presented.

### **7.1 Summary**

The technological difficulties with obtaining geometric accuracy, expanding process capability and enhancing material properties in the area of flexible manufacturing have created a disparity between qualified supply and market demand for customized sheet metal parts. Hence, the objectives of this thesis are to improve flexible sheet forming processes (i.e., ISF) in terms of their accuracy, efficiency, capability to deform hard-to-form materials, and resulting material properties.

The most prominent challenge in ISF are the large geometric deviations of the formed parts from their desired dimensions. These deviations occur both during and after the forming process. To minimize the in-process inaccuracies, a new hybrid process, MDSIF, was developed that preforms the material with ADSIF in the first and then fine tunes the part with DSIF in the second pass. This results in parts with better geometric accuracy than the previous best achievable accuracy, while also shortening the forming time by half. Thus, improved process performance is obtained.

To reduce post-process inaccuracies, a new post-forming annealing method that reduces deviations by more than one order of magnitude was established. Portable clamping devices that constrain the formed geometry during annealing were designed, together with a simple method for

selecting the proper annealing parameters. This practical annealing method also preserves the improved in-process geometric accuracy from earlier stages.

The capability to deform hard-to-form materials is achieved via the hybrid EA-ISF processes. Due to reduced forming forces in the D-stage (the second pass using DSIF after the first ADSIF pass) of MDSIF and secured tool-sheet contact, greater formability, better surface finish, and improved compatibility with electricity are attained as compared to parts produced using conventional DSIF. These aspects benefit the development of the spark-free EA-DSIF processes (including EA-ADSIF and EA-MDSIF). To further improve these processes, a simple analytical model and the corresponding experimental validation method were developed to help detect the actual forming temperature in the invisible tool-sheet contact area, which cannot be measured by IR cameras. A patient-specific acetabular cup made of Ti6Al4V for hip replacement was then successfully formed with EA-MDSIF.

Reduced forming forces were achieved when electricity was applied in the hybrid EA-DSIF processes. However, the dominant deformation mechanisms behind the reduced forming forces resulting from electro-thermo-mechanical processes are controversial. An *in situ* high-energy XRD study platform was provided to examine the material's real-time microstructural responses under macroscopic electro-thermo-mechanical loadings. Since similar macroscopic tensile behaviors and microstructural responses were found in the low to medium temperature ranges for thermo-mechanical loadings and in EA tensile tests with different electricity patterns, the existence of the athermal effect of electroplasticity could not be confirmed. While electro-thermo-mechanical processes can be analyzed using thermal-mechanical deformation mechanisms, the prediction of microstructural responses cannot be further simplified to kinetics models.

After examining the deformation mechanisms, the material properties of the formed parts were investigated. Microstructural analysis on the fracture surface was performed to understand the fracture mechanisms in EA-cDSIF. The fracture mode was identified as Mode I, and the point of origin was located at the outer surface. It is suggested that lower forming forces in the meridional direction are beneficial to the material's formability. This also explains the increased forming depth in EA-MDSIF compared to other EA-DSIF processes. Competing effects of work-hardening due to plastic deformation and thermal softening due to elevated temperature were found when hardness was examined. Since the softening effects are more pronounced when higher current intensities are applied, the lowest possible amperage capable of deforming the material to the desired depth is suggested to achieve optimal hardness. Surface topography was found to rely on toolpath strategy, tool material, and current intensity in ISF processes. Processes with low forming forces are beneficial to surface quality. In EA-DSIF processes, the use of tungsten tools and low current intensities results in smoother surfaces. Additionally, surfaces with eliminated cracks have been found in EA-DSIF processes, unlike the Ti6Al4V parts formed without electricity at room temperature. Finally, fatigue life and residual stresses have been studied in ISF, providing missing knowledge in this field.

## **7.2 Future directions**

### ***7.2.1 On-site annealing***

To reduce springback in a more efficient way, without part removal, re-assembly, or transportation after forming (as discussed in Section 4.5), an on-site annealing setup with a closed



chamber that reduces heat loss and generates sufficiently high elevated temperatures within the workpiece would further increase process efficiency and flexibility.

### ***7.2.2 DSIF for post-treatment: EA vibrational surface treatment***

It has been found that the forming force in DSIF or EA-cDSIF is directly proportional to the forming depth due to global bending. Since the part fractures in Mode I, DSIF or EA-cDSIF can only achieve limited depth as discussed in Section 6.1. Although DSIF or EA-cDSIF as forming processes have their limitations in formability, using them for secondary passes results in reduced forming forces. This improves geometric accuracy, increases formability, and enhances surface quality. Therefore, it is hypothesized that processes utilizing the configuration of DSIF in post-treatment may result in similar desirable features on the parts, such as increased hardness, surface appearance and fatigue life.

A method of flexible EA vibrational surface treatment could be developed as shown in Figure 7.1 to enhance the surface of the already manufactured parts. The vibrations may also help in reducing springback, similar to shot peening processes, but with better control on the treated location. Vibratory motions can be applied as shown in Figure 7.2.

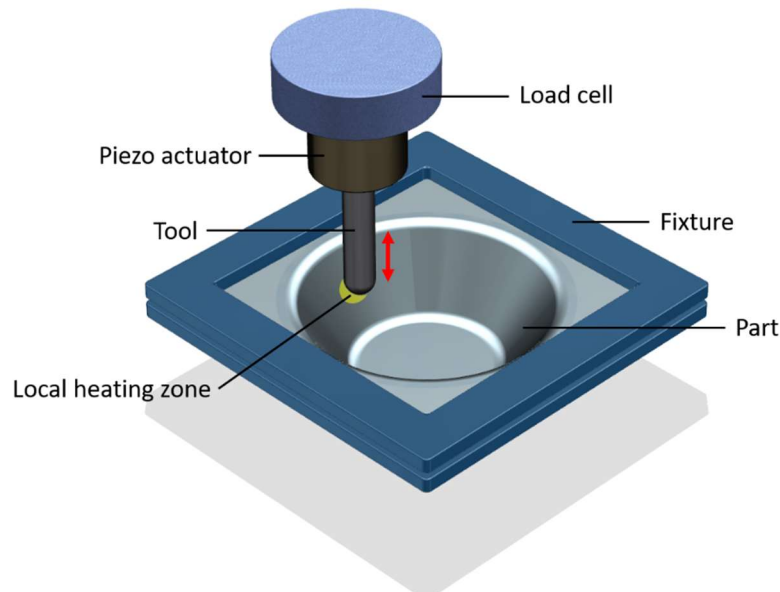


Figure 7.1 Configuration of flexible EA vibrational surface treatment

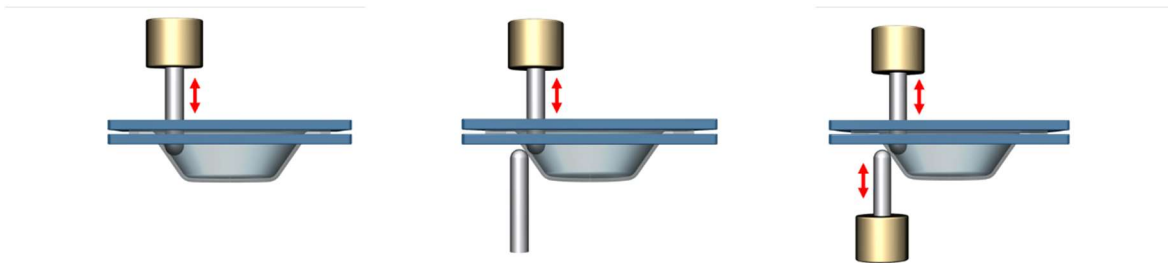


Figure 7.2 Schematic of possible tool motions

### ***7.2.3 Residual stress analysis due to non-uniform deformation and heating***

ISF is a localized deformation process suggesting that electrically-assisted DSIF would result in localized deformation combined with a localized heating process. This localization feature causes non-uniform deformation and heating in the tool-sheet interaction zone as well as in the rest of the sheet metal during the forming process. Therefore, this generates a non-uniform residual stress distribution, which affects the final part geometry and mechanical properties. Numerical simulations would be beneficial to map the residual stress distribution and optimize the annealing

process. The simulation can be validated by the results from the residual stress measurement described in Section 6.4. The established model can also be extended to additive manufacturing processes where localized heating is observed.

## References

- Al-Obaidi, A., Kräusel, V. & Landgrebe, D. 2015. Hot single-point incremental forming assisted by induction heating. *The International Journal of Advanced Manufacturing Technology*, 1-9.
- Allwood, J., Shouler, D. & Tekkaya, A. E. The increased forming limits of incremental sheet forming processes. *Key Engineering Materials*, 2007. Trans Tech Publ, 621-628.
- Allwood, J. M., Braun, D. & Music, O. 2010. The effect of partially cut-out blanks on geometric accuracy in incremental sheet forming. *Journal of Materials Processing Technology*, 210, 1501-1510.
- Ambrogio, G., Cozza, V., Filice, L. & Micari, F. 2007. An analytical model for improving precision in single point incremental forming. *Journal of Materials Processing Technology*, 191, 92-95.
- Ambrogio, G., De Napoli, L., Filice, L., Gagliardi, F. & Muzzupappa, M. 2005. Application of Incremental Forming process for high customised medical product manufacturing. *Journal of Materials Processing Technology*, 162, 156-162.
- Ambrogio, G., Filice, L. & Gagliardi, F. 2012. Formability of lightweight alloys by hot incremental sheet forming. *Materials & Design*, 34, 501-508.
- Ambrogio, G., Gagliardi, F., Bruschi, S. & Filice, L. 2013. On the high-speed Single Point Incremental Forming of titanium alloys. *CIRP Annals-Manufacturing Technology*, 62, 243-246.

- Anderoglu, O. 2005. *Residual stress measurement using X-ray diffraction*. Texas A&M University.
- Attanasio, A., Ceretti, E., Giardini, C. & Mazzone, L. 2008. Asymmetric two points incremental forming: improving surface quality and geometric accuracy by tool path optimization. *Journal of Materials Processing Technology*, 197, 59-67.
- Babu, B. & Lindgren, L.-E. 2013. Dislocation density based model for plastic deformation and globularization of Ti-6Al-4V. *International Journal of Plasticity*, 50, 94-108.
- Bagno, A. & Di Bello, C. 2004. Surface treatments and roughness properties of Ti-based biomaterials. *Journal of Materials Science: Materials in Medicine*, 15, 935-949.
- Bambach, M., Araghi, B. T. & Hirt, G. 2009. Strategies to improve the geometric accuracy in asymmetric single point incremental forming. *Production Engineering*, 3, 145-156.
- Bergman, G. 1999. *Modelling and simulation of simultaneous forming and quenching*. Luleå tekniska universitet.
- Bhushan, B. & Caspers, M. 2017. An overview of additive manufacturing (3D printing) for microfabrication. *Microsystem Technologies*, 23, 1117-1124.
- Bilyk, S., Ramesh, K. & Wright, T. 2005. Finite deformations of metal cylinders subjected to electromagnetic fields and mechanical forces. *Journal of the Mechanics and Physics of Solids*, 53, 525-544.
- Bronfenbrenner, D., Bibee, M. & Mehta, A. 2010. Visualizing Three-Dimensional Micromechanical Response in Nanomaterials. *arXiv preprint arXiv:1004.4878*.
- Bunget, C., Salandro, W., Mears, L. & Roth, J. T. 2010. Energy-based modeling of an electrically-assisted forging process. *Trans. North Am. Manuf. Res. Inst. SME*, 38, 647-654.

- Cheng, H. S., Cao, J. & Xia, Z. C. 2007. An accelerated springback compensation method. *International Journal of Mechanical Sciences*, 49, 267-279.
- Conrad, H. 2000. Electroplasticity in metals and ceramics. *Materials Science and Engineering: A*, 287, 276-287.
- Conrad, H. 2002. Thermally activated plastic flow of metals and ceramics with an electric field or current. *Materials Science and Engineering: A*, 322, 100-107.
- DebRoy, T., Wei, H., Zuback, J., Mukherjee, T., Elmer, J., Milewski, J., Beese, A., Wilson-Heid, A., De, A. & Zhang, W. 2017. Additive manufacturing of metallic components—process, structure and properties. *Progress in Materials Science*.
- Dittrich, M., Gutowski, T., Cao, J., Roth, J., Xia, Z., Kiridena, V., Ren, F. & Henning, H. 2012. Exergy analysis of incremental sheet forming. *Production Engineering*, 6, 169-177.
- Du, C. & Hsuing, C. 2011. Local Softening Technique Experiments on DP980 Steel. *US Department of Energy, Vehicle Technologies Program*.
- Dufloy, J., Callebaut, B., Verbert, J. & De Baerdemaeker, H. 2007. Laser assisted incremental forming: formability and accuracy improvement. *CIRP Annals-Manufacturing Technology*, 56, 273-276.
- Egea, A. J. S., Rojas, H. A. G., Celentano, D. J. & Peiró, J. J. 2016. Mechanical and metallurgical changes on 308L wires drawn by electropulses. *Materials & Design*, 90, 1159-1169.
- Essa, K. & Hartley, P. 2011. An assessment of various process strategies for improving precision in single point incremental forming. *International journal of material forming*, 4, 401-412.

- Ezugwu, E. & Wang, Z. 1997. Titanium alloys and their machinability—a review. *Journal of materials processing technology*, 68, 262-274.
- Fan, G., Sun, F., Meng, X., Gao, L. & Tong, G. 2010. Electric hot incremental forming of Ti-6Al-4V titanium sheet. *The International Journal of Advanced Manufacturing Technology*, 49, 941-947.
- Fan, R., Magargee, J., Hu, P. & Cao, J. 2013. Influence of grain size and grain boundaries on the thermal and mechanical behavior of 70/30 brass under electrically-assisted deformation. *Materials Science and Engineering: A*, 574, 218-225.
- Fang, Y., Lu, B., Chen, J., Xu, D. & Ou, H. 2014. Analytical and experimental investigations on deformation mechanism and fracture behavior in single point incremental forming. *Journal of Materials Processing Technology*, 214, 1503-1515.
- Fiorentino, A., Ceretti, E., Attanasio, A., Mazzoni, L. & Giardini, C. 2009. Analysis of forces, accuracy and formability in positive die sheet incremental forming. *International Journal of Material Forming*, 2, 805-808.
- Fu, Z., Mo, J., Han, F. & Gong, P. 2013. Tool path correction algorithm for single-point incremental forming of sheet metal. *The International Journal of Advanced Manufacturing Technology*, 64, 1239-1248.
- Genevois, C., Fabrègue, D., Deschamps, A. & Poole, W. J. 2006. On the coupling between precipitation and plastic deformation in relation with friction stir welding of AA2024 T3 aluminium alloy. *Materials Science and Engineering: A*, 441, 39-48.

- Göttmann, A., Diettrich, J., Bergweiler, G., Bambach, M., Hirt, G., Loosen, P. & Poprawe, R. 2011. Laser-assisted asymmetric incremental sheet forming of titanium sheet metal parts. *Production Engineering*, 5, 263-271.
- Handbook, A. S. M. 1991. Volume 4. *Heat treating*.
- Handbook, A. S. M. 2001. Volume 12. *Fractography*.
- Hertzberg, R. W. 1989. Deformation and fracture mechanics of engineering materials.
- Hexagon 2017. Romer Absolute Arm Advanced Portable 3D Measurement. *Product Brochure*.
- Hosford, W. F. 2005. *Physical Metallurgy*, Taylor & Francis Group.
- Huang, Y., Wang, Y., Cao, J. & Li, M. Prediction of forming limit in single point incremental forming with the ductile fracture criterion. ASME 2007 International Manufacturing Science and Engineering Conference, 2007. American Society of Mechanical Engineers, 929-934.
- Hussain, G., Gao, L., Hayat, N. & Dar, N. 2010. The formability of annealed and pre-aged AA-2024 sheets in single-point incremental forming. *The International Journal of Advanced Manufacturing Technology*, 46, 543-549.
- Hutchings, M. T., Withers, P. J., Holden, T. M. & Lorentzen, T. 2005. *Introduction to the characterization of residual stress by neutron diffraction*, CRC press.
- Jackson, K. & Allwood, J. 2009. The mechanics of incremental sheet forming. *Journal of materials processing technology*, 209, 1158-1174.



- Jeswiet, J., Geiger, M., Engel, U., Kleiner, M., Schikorra, M., Duflou, J., Neugebauer, R., Bariani, P. & Bruschi, S. 2008. Metal forming progress since 2000. *CIRP Journal of Manufacturing Science and Technology*, 1, 2-17.
- Jeswiet, J., Micari, F., Hirt, G., Bramley, A., Duflou, J. & Allwood, J. 2005. Asymmetric single point incremental forming of sheet metal. *CIRP Annals-Manufacturing Technology*, 54, 88-114.
- Kandil, F., Lord, J., Fry, A. & Grant, P. 2001. A review of residual stress measurement methods. *A Guide to Technique Selection, NPL, Report MATC (A)*, 4.
- Kang, W., Beniam, I. & Qidwai, S. M. 2016. In situ electron microscopy studies of electromechanical behavior in metals at the nanoscale using a novel microdevice-based system. *Review of Scientific Instruments*, 87, 095001.
- Karbasian, H. & Tekkaya, A. E. 2010. A review on hot stamping. *Journal of Materials Processing Technology*, 210, 2103-2118.
- Kim, Y. & Park, J. 2002. Effect of process parameters on formability in incremental forming of sheet metal. *Journal of materials processing technology*, 130, 42-46.
- Kinsey, B., Cullen, G., Jordan, A. & Mates, S. 2013. Investigation of electroplastic effect at high deformation rates for 304SS and Ti-6Al-4V. *CIRP Annals-Manufacturing Technology*, 62, 279-282.
- Kolupaeva, S. & Semenov, M. The stored energy of plastic deformation in crystals of face-centered cubic metals. *IOP Conference Series: Materials Science and Engineering*, 2015. IOP Publishing, 012077.

- Lee, T., Magargee, J., Ng, M. K. & Cao, J. 2017. Constitutive analysis of electrically-assisted tensile deformation based on non-uniform thermal expansion, plastic softening and dynamic strain aging. *International Journal of Plasticity*.
- Levy, B. 1984. Empirically derived equations for predicting springback in bending. *Journal of Applied Metalworking*, 3, 135-141.
- Li, D. L. & Yu, E. L. An Approach Based on the Classical Free-Electron Theory to Study Electroplastic Effect. *Advanced Materials Research*, 2011. Trans Tech Publ, 71-74.
- Li, X., Guo, G., Xiao, J., Song, N. & Li, D. 2014. Constitutive modeling and the effects of strain-rate and temperature on the formability of Ti-6Al-4V alloy sheet. *Materials & Design*, 55, 325-334.
- Li, Y., Zou, S., Wang, D., Feng, G., Bao, C. & Hu, J. 2010. The effect of hydrofluoric acid treatment on titanium implant osseointegration in ovariectomized rats. *Biomaterials*, 31, 3266-3273.
- Lin, Y. & Chen, X.-M. 2011. A critical review of experimental results and constitutive descriptions for metals and alloys in hot working. *Materials & Design*, 32, 1733-1759.
- Lu, B., Fang, Y., Xu, D., Chen, J., Ai, S., Long, H., Ou, H. & Cao, J. 2015a. Investigation of material deformation mechanism in double side incremental sheet forming. *International Journal of Machine Tools and Manufacture*, 93, 37-48.
- Lu, B., Xu, D. K., Liu, R. Z., Ou, H., Long, H. & Chen, J. 2015b. Cranial reconstruction using double side incremental forming. *Key Engineering Materials*, 639, 535-542.

- Madeira, T., Silva, C., Silva, M. & Martins, P. 2015. Failure in single point incremental forming. *The International Journal of Advanced Manufacturing Technology*, 80, 1471-1479.
- Magargee, J., Fan, R. & Cao, J. 2013a. Analysis and observations of current density sensitivity and thermally activated mechanical behavior in electrically-assisted deformation. *Journal of Manufacturing Science and Engineering*, 135, 061022.
- Magargee, J., Morestin, F. & Cao, J. 2013b. Characterization of flow stress for commercially pure titanium subjected to electrically assisted deformation. *Journal of Engineering Materials and Technology*, 135, 041003.
- Magargee, J. K. 2014. *Mechanics of Electrically-Assisted Deformation in Metals*. NORTHWESTERN UNIVERSITY.
- Mai, J., Peng, L., Lin, Z. & Lai, X. 2011. Experimental study of electrical resistivity and flow stress of stainless steel 316L in electroplastic deformation. *Materials Science and Engineering: A*, 528, 3539-3544.
- Maidagan, E., Zettler, J., Bambach, M., Rodríguez, P. & Hirt, G. 2007. A new incremental sheet forming process based on a flexible supporting die system. *Key Engineering Materials*, 344, 607-614.
- Malhotra, R., Cao, J., Beltran, M., Xu, D., Magargee, J., Kiridena, V. & Xia, Z. C. 2012a. Accumulative-DSIF strategy for enhancing process capabilities in incremental forming. *CIRP Annals-Manufacturing Technology*, 61, 251-254.

- Malhotra, R., Cao, J., Ren, F., Kiridena, V., Xia, Z. C. & Reddy, N. 2011. Improvement of geometric accuracy in incremental forming by using a squeezing toolpath strategy with two forming tools. *Journal of Manufacturing Science and Engineering*, 133, 061019.
- Malhotra, R., Xue, L., Belytschko, T. & Cao, J. 2012b. Mechanics of fracture in single point incremental forming. *Journal of Materials Processing Technology*, 212, 1573-1590.
- Manyika, J., Sinclair, J., Dobbs, R., Strube, G., Rasse, L., Mischke, J., Remes, J., Roxburgh, C., George, K., O'Halloran, D. & Ramaswamy, S. Manufacturing the future: The next era of global growth and innovation. McKinsey Global Institute. McKinsey Global Institute 2012
- Meier, H. & Magnus, C. Incremental sheet metal forming with direct resistance heating using two moving tools. *Key Engineering Materials*, 2013. Trans Tech Publ, 1362-1367.
- Meier, H., Smukala, V., Dewald, O. & Zhang, J. 2007. Two point incremental forming with two moving forming tools. *Key Engineering Materials*, 344, 599-605.
- Molotskii, M. I. 2000. Theoretical basis for electro-and magnetoplasticity. *Materials Science and Engineering: A*, 287, 248-258.
- Mori, K., Maki, S. & Tanaka, Y. 2005. Warm and hot stamping of ultra high tensile strength steel sheets using resistance heating. *CIRP Annals-Manufacturing Technology*, 54, 209-212.
- Moser, N., Zhang, Z., Ren, H., Ehmann, K. & Cao, J. An investigation into the mechanics of double-sided incremental forming using finite element methods. *AIP Conference Proceedings*, 2016a. AIP Publishing, 070021.
- Moser, N., Zhang, Z., Ren, H., Zhang, H., Shi, Y., Ndip-Agbor, E. E., Lu, B., Chen, J., Ehmann, K. F. & Cao, J. 2016b. Effective forming strategy for double-sided incremental forming

- considering in-plane curvature and tool direction. *CIRP Annals-Manufacturing Technology*, 65, 265-268.
- Ndip-Agbor, E. E., Smith, J., Xu, R., Malhotra, R. & Cao, J. Effect of relative tool position on the geometric accuracy of accumulative DSIF. AIP Conference Proceedings, 2013. AIP, 828-831.
- Ng, M.-K., Fan, Z., Gao, R. X., Smith, E. F. & Cao, J. 2014. Characterization of electrically-assisted micro-rolling for surface texturing using embedded sensor. *CIRP Annals-Manufacturing Technology*, 63, 269-272.
- Nielsen, C. V., Zhang, W., Alves, L., Bay, N. & Martins, P. 2012. *Modeling of thermo-electro-mechanical manufacturing processes: applications in metal forming and resistance welding*, Springer Science & Business Media.
- Noyan, I. C. & Cohen, J. B. 2013. *Residual stress: measurement by diffraction and interpretation*, Springer.
- Okazaki, K., Kagawa, M. & Conrad, H. 1978. A study of the electroplastic effect in metals. *Scripta Metallurgica*, 12, 1063-1068.
- Olson, G. B. 2000. Designing a new material world. *Science*, 288, 993-998.
- Ortiz, M., Penalva, M., Puerto, M. J., Homola, P. & Kafka, V. Hot Single Point Incremental Forming of Ti-6Al-4V Alloy. Key Engineering Materials, 2014. Trans Tech Publ, 1079-1087.

- Palmer, T., Elmer, J. & Wong, J. 2002. In situ observations of ferrite–austenite transformations in duplex stainless steel weldments using synchrotron radiation. *Science and technology of Welding and Joining*, 7, 159-171.
- Park, C. H., Ko, Y. G., Park, J.-W. & Lee, C. S. 2008. Enhanced superplasticity utilizing dynamic globularization of Ti–6Al–4V alloy. *Materials Science and Engineering: A*, 496, 150-158.
- Radu, C., Tampu, C., Cristea, I. & Chirita, B. 2013. The effect of residual stresses on the accuracy of parts processed by SPIF. *Materials and Manufacturing Processes*, 28, 572-576.
- Ramaswamy, S., Manyika, J., Pinkus, G., George, K., Law, J., Gambell, T. & Serafino, A. Making it in America: Revitalizing US manufacturing. McKinsey Global Institute. 2017
- Ross, C. D., Kronenberger, T. J. & Roth, J. T. 2009. Effect of dc on the formability of Ti–6Al–4V. *Journal of Engineering Materials and Technology*, 131, 031004.
- Rudnev, V., Brown, D., Van Tyne, C. & Clarke, K. Intricacies for the successful induction heating of steels in modern forge shops. Proceedings of the 19th Forging Congress, Chicago, IL, 2008.
- Salandro, W. A., Bunget, C. J. & Mears, L. 2012. A thermal-based approach for determining electroplastic characteristics. *Proceedings of the Institution of Mechanical Engineers, Part B: Journal of Engineering Manufacture*, 226, 775-788.
- Santos, T. G., Miranda, R. & Vilaca, P. 2014. Friction Stir Welding assisted by electrical Joule effect. *Journal of Materials Processing Technology*, 214, 2127-2133.
- Schajer, G. S. 2013. *Practical residual stress measurement methods*, John Wiley & Sons.

- Sieniawski, J. & Motyka, M. 2007. Superplasticity in titanium alloys. *Journal of Achievements in Materials and Manufacturing Engineering*, 24, 123-130.
- Smith, J., Malhotra, R., Liu, W. & Cao, J. 2013. Deformation mechanics in single-point and accumulative double-sided incremental forming. *The International Journal of Advanced Manufacturing Technology*, 69, 1185-1201.
- Soeiro, J., Silva, C., Silva, M. & Martins, P. 2015. Revisiting the formability limits by fracture in sheet metal forming. *Journal of Materials Processing Technology*, 217, 184-192.
- Sprecher, A. & Conrad, H. 1989. Effect of strain rate on the electroplastic effect in Nb. *Scripta Metallurgica*, 23, 151-155.
- Suresh, S. 1998. *Fatigue of materials*, Cambridge university press.
- Tanaka, S., Nakamura, T., Hayakawa, K., Nakamura, H., Motomura, K., Cesar de Sa, J. M. & Santos, A. D. Residual stress in sheet metal parts made by incremental forming process. *AIP Conference Proceedings*, 2007. AIP, 775-780.
- Tekkaya, A. E., Shankar, R., Sebastiani, G., Homberg, W. & Kleiner, M. 2007. Surface reconstruction for incremental forming. *Production Engineering*, 1, 71-78.
- U.S. Bureau of Economic Analysis. Gross Domestic Product (GDP) by Industry. 2017
- Ungar, E. E. 1960. *Mechanics of the Sheet-Bending Process*1.
- Unger, J., Stiemer, M., Walden, L., Bach, F., Blum, H. & Svendsen, B. On the effect of current pulses on the material behavior during electromagnetic metal forming. 2nd International Conference on High Speed Forming,(ICHSF 2006), Dortmund, Germany March, 2006. 20-21.

- Valoppi, B., Bruschi, S. & Ghiotti, A. 2016. Modelling of Fracture Onset in Ti6Al4V Sheets Deformed at Elevated Temperature. *Procedia Manufacturing*, 5, 248-258.
- Walczyk, D. F. & Hardt, D. E. 1998. Design and analysis of reconfigurable discrete dies for sheet metal forming. *Journal of Manufacturing Systems*, 17, 436-454.
- Wang, C., Kinzel, G. & Altan, T. 1993. Mathematical modeling of plane-strain bending of sheet and plate. *Journal of Materials Processing Technology*, 39, 279-304.
- Wang, J., Wagoner, R., Carden, W., Matlock, D. & Barlat, F. 2004. Creep and anelasticity in the springback of aluminum. *International Journal of Plasticity*, 20, 2209-2232.
- Wang, X., Xu, J., Shan, D., Guo, B. & Cao, J. 2016. Modeling of thermal and mechanical behavior of a magnesium alloy AZ31 during electrically-assisted micro-tension. *International Journal of Plasticity*, 85, 230-257.
- Wang, Y., Huang, Y., Cao, J. & Reddy, N. V. Experimental study on a new method of double side incremental forming. ASME 2008 International Manufacturing Science and Engineering Conference collocated with the 3rd JSME/ASME International Conference on Materials and Processing, 2008. American Society of Mechanical Engineers, 601-607.
- Xu, Q., Guan, L., Jiang, Y., Tang, G. & Wang, S. 2010. Improved plasticity of Mg–Al–Zn alloy by electropulsing tension. *Materials Letters*, 64, 1085-1087.
- Xu, R., Ren, H., Zhang, Z., Malhotra, R. & Cao, J. A mixed toolpath strategy for improved geometric accuracy and higher throughput in double-sided incremental forming. ASME 2014 international manufacturing science and engineering conference collocated with the JSME 2014 international conference on materials and processing and the 42nd North



- American manufacturing research conference, 2014a. American Society of Mechanical Engineers, V002T02A082-V002T02A082.
- Xu, R., Shi, X., Xu, D., Malhotra, R. & Cao, J. 2014b. A preliminary study on the fatigue behavior of sheet metal parts formed with accumulative-double-sided incremental forming. *Manufacturing Letters*, 2, 8-11.
- Ye, X., Kuang, J., Li, X. & Tang, G. 2014. Microstructure, properties and temperature evolution of electro-pulsing treated functionally graded Ti-6Al-4V alloy strip. *Journal of Alloys and Compounds*, 599, 1-9.
- Yu, T. & Johnson, W. 1983. Cylindrical bending of metal strips. *Metals Technology*, 10, 439-447.
- Zhang, D., To, S., Zhu, Y., Wang, H. & Tang, G. 2012. Dynamic electropulsing induced phase transformations and their effects on single point diamond turning of AZ91 alloy. *Journal of Surface Engineered Materials and Advanced Technology*, 2, 16.
- Zhang, Z., Ren, H., Xu, R., Moser, N., Smith, J., Ndip-Agbor, E., Malhotra, R., Xia, Z. C., Ehmann, K. F. & Cao, J. 2015. A mixed double-sided incremental forming toolpath strategy for improved geometric accuracy. *Journal of Manufacturing Science and Engineering*, 137, 051007.
- Zhang, Z., Zhang, H., Shi, Y., Moser, N., Ren, H., Ehmann, K. F. & Cao, J. 2016. Springback reduction by annealing for incremental sheet forming. *Procedia Manufacturing*, 5, 696-706.

## Appendix A

Tutorial for operating the DSIF Machine

### Before Use

- a. DO NOT operate the machine alone

Any new operator must run the machine with the supervision of Ebot/Huaqing/Newell/Zixuan before we give the permission.

Please make the reservation at the following website:

[https://docs.google.com/a/u.northwestern.edu/spreadsheet/cc?key=0Aifs4ReSJHCydDIweV1Ddl16MXJ2TXVnRk11SWZnMnc&usp=sharing\\_eil#gid=21](https://docs.google.com/a/u.northwestern.edu/spreadsheet/cc?key=0Aifs4ReSJHCydDIweV1Ddl16MXJ2TXVnRk11SWZnMnc&usp=sharing_eil#gid=21)

And find a supervisor (Ebot, Huaqing, Newell, or Zixuan) before you turn on the machine.

- b. Press the STOP bottom in emergency

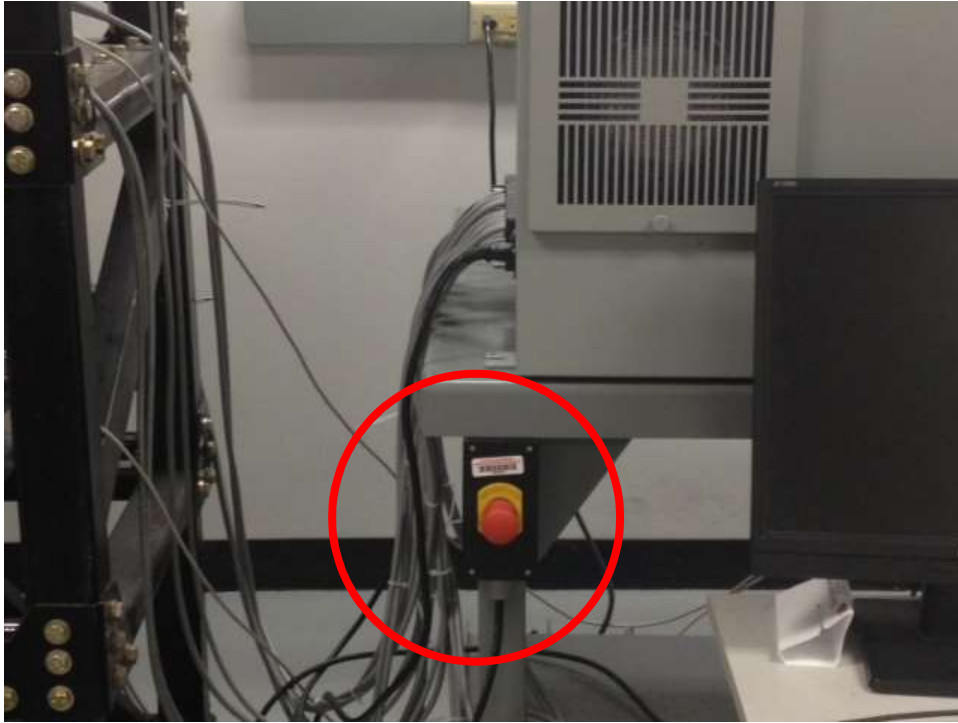


Figure 7.3 STOP Bottom

The STOP bottom is a red bottom which is placed between the computer and the machine (as shown in Figure 1).

## Machine Basics

- a. Hardware

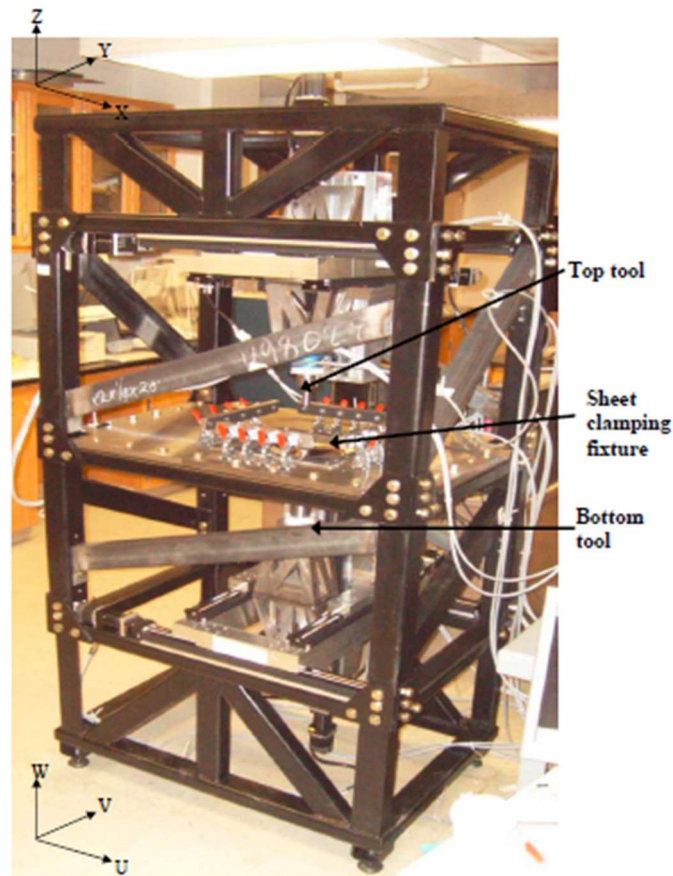


Figure 7.4 Components of the DSIF Machine

The Double-Sided Incremental Forming (DSIF) machine is basically composed of top tool, bottom tool and clamping fixture. The X-Y-Z and U-V-W coordinate system correspond to right-handed Cartesian axis system for the top and bottom tools respectively (as shown in Figure 2). For X, Y, U, and V axis, each has two linear guides; for Z and W, each has one linear guide. Each linear guide is individually controlled by its own motor. The clamping fixture provides a maximum forming area of 250 mm by 250 mm.

b. Control

The control system used for the DSIF machine is Delta Tau PMAC. In our case, we always assign the center of the forming area as  $X=0$ ,  $Y=0$ ,  $U=0$  and  $V=0$ . Both  $Z=0$  and  $W=0$  are at the top surface of the sheet. The motors are assigned as follows:

X axis: motors #1 and #2

Y axis: motors #3 and #4

Z axis: motor #5

U axis: motors #6 and #7

V axis: motors #8 and #9

W axis: motor #10

The servo motors have 8000 counts per revolution. There is a gearbox with 1:10 ratio connected to each motor. The pitch of the linear guide is 5 mm. These mean that each millimeter is equal to 16000 counts of the motor. Because of the assembly direction, sometimes the natural positive direction of the motor is not the same with the direction of Cartesian coordinate in Figure 2. This is why there are minus signs shown in the programs in the directions of X, U and W.

More details about the control system of the DSIF machine can be found in Rajiv Malhotra's PhD thesis page 158-166. A nice example of the program is also provided in his thesis.

## Operation Steps

- a. Turn on the devices
  - Plug the connection cable to the control box

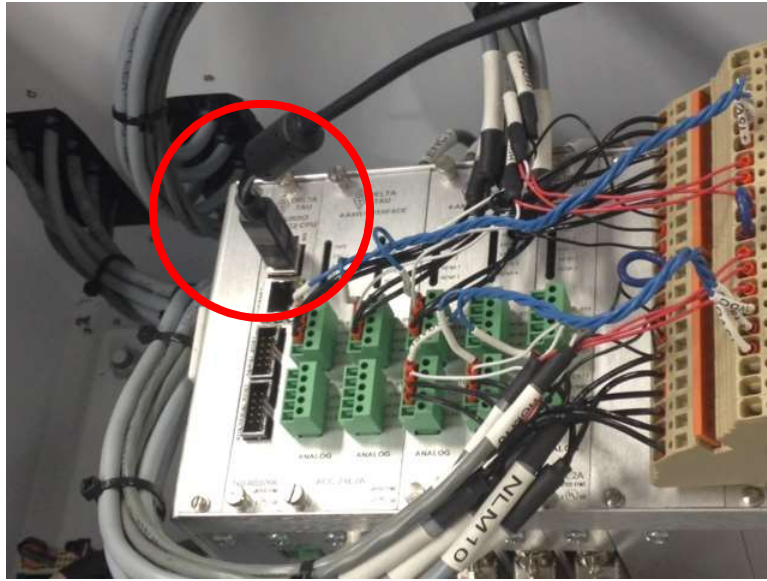


Figure 7.5 Connection Plug In

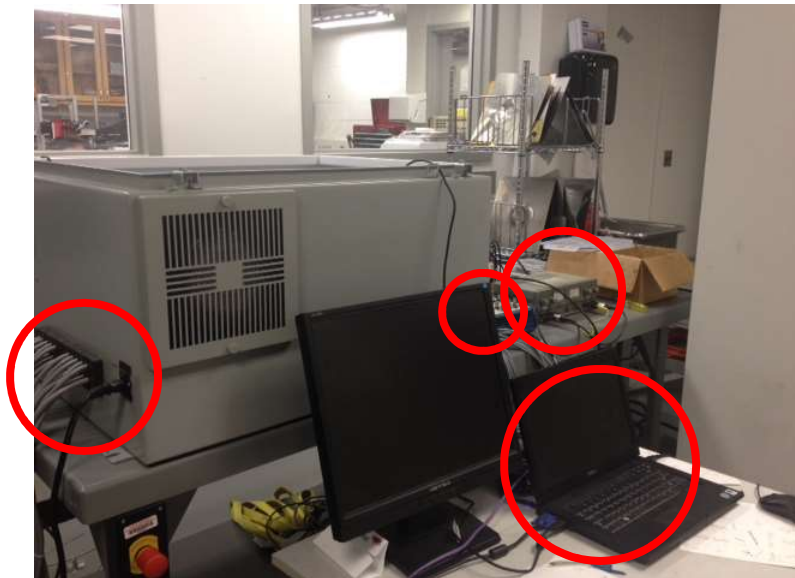


Figure 7.6 Devices to turn on

- Turn on the 4 devices circled in Figure 4

*If the machine clicks repeatedly when turned on, it could be that the Emergency Off button was pushed. Then you need to reset the STOP bottom first.*

#### b. PEWIN32-PRO program initial commands

- Select *Earlier Version* when the computer is asking for your selection of system
- Password for the computer is *hydra*
- Double click the icon of PEWIN32 Pro2 (shown in Figure 5) on the desktop

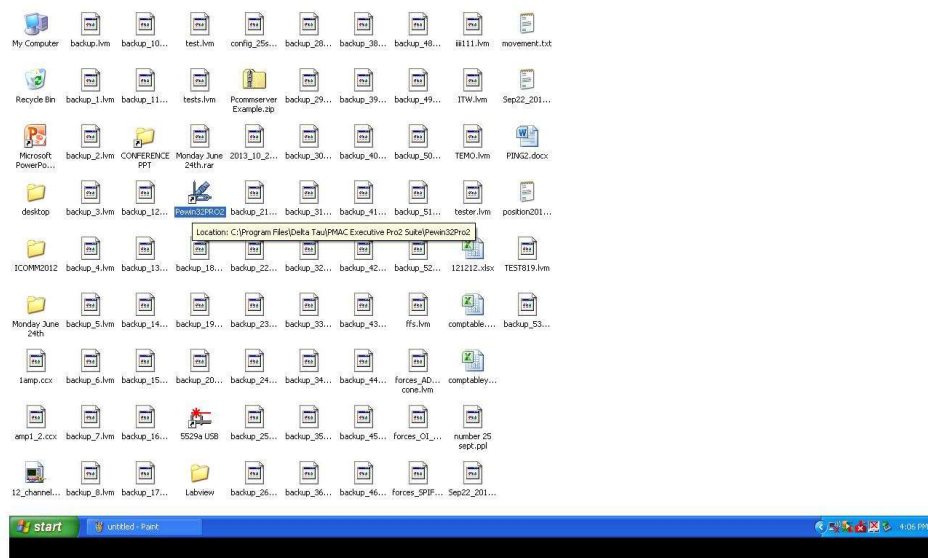


Figure 7.7 PEWIN32 PRO2

The interface of the software is shown in Figure 6. The right window of the three windows is showing the position of the counts of the motors (i.e., the position of the tools). The initial command will be typed in the left window.

When you look into the control box after you turn on the box, you will notice that the lights of the motors are flashing. This is because the motors are now open loop.

So the first thing to do after we open the software is to make closed loop.

- Type in:  
#1j/
- Then hit *Enter*

Now when you look into the control box, you will see that the light corresponding to motor #1 is on and not flashing anymore.

- Similarly type in #2j/ and hit Enter...till #10j/ and Enter (shown in the right window of Figure 6)
- Now check the box and make sure that every motor is closed loop

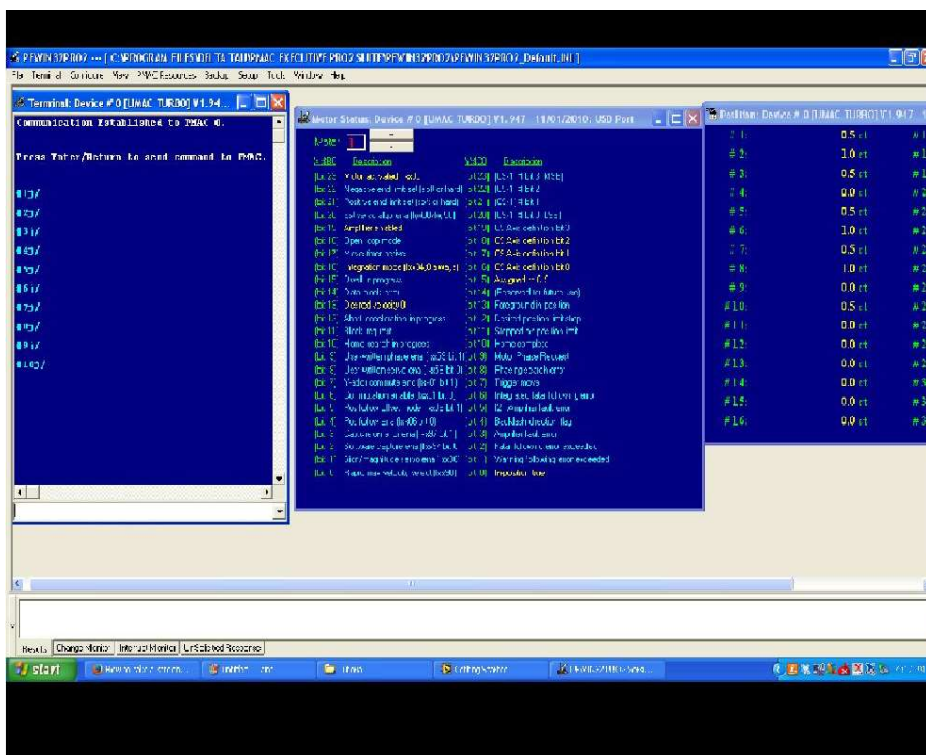


Figure 7.8 PEWIN interface

c. Home motors



Because the motors need home their positions each time they are switched off and on again. The motors are homed by taking the tools to the home position and then assign this position to be home. We will bring the top tool to (0 0 100) and the bottom tool to (0 0 -100) before we switch off the machine. With this in mind, we will have the following steps to set home.

- Set every motor home at the current position by typing:  
#1HMZ
- Then hit *Enter*
- Till #10HMZ and *Enter*

Now set motor #5 home by bringing down the top tool by 100 *mm*.

- Select *File* → *Open File* → *My Computer* → *F:* → *EADSIF* → *programs* → select *text files* in *Files of type* → *Open first program test.txt* (as shown in Figure 7)

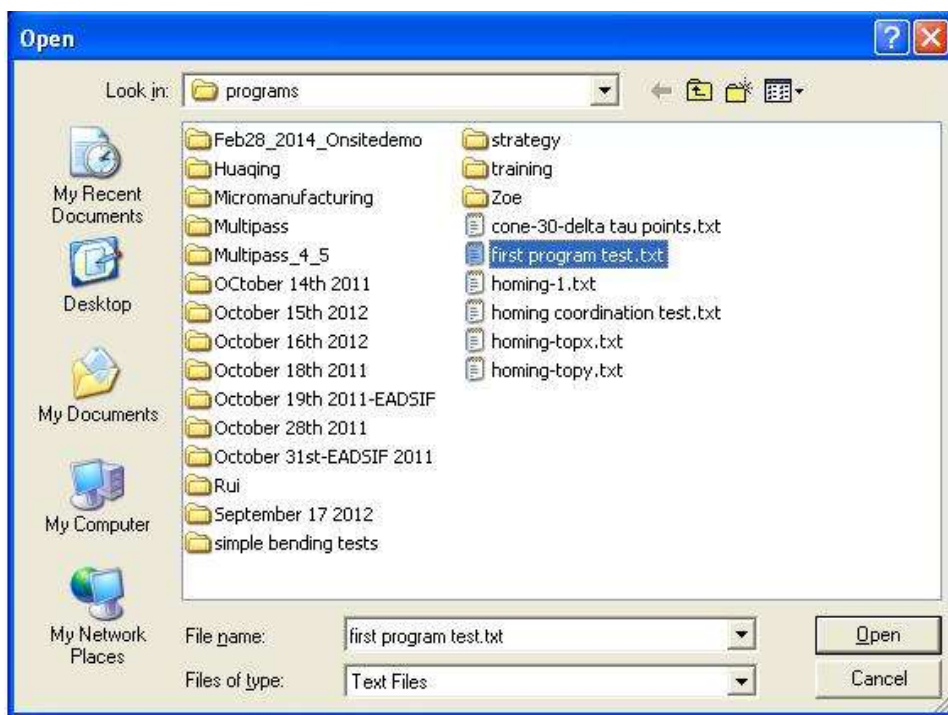


Figure 7.9 First program test.txt

- Change *ABS* to *INC*, which means that the tool will move incrementally based on the values in the second to last line of the program (Figure 8).

- Change the value behind *Z* to *-100.0*, and delete all other value except for *F* (Figure 9).
- Press *Save* in the middle window
- Press *Download* (↓) in the middle window
- Type in the left command window :  
    &1 B2 R

Here &1 corresponds to the coordinate system for which B2, i.e., program number 2 is to be used. The R command simply asks the controller to run this particular program for this particular coordinate system.

- Wait until the top tool moved to the position and stopped
- Set motor #5 home by typing in the left command window:  
    #5HMZ
- Now change both *Z* and *W* into *100.0* to move both tools up
- Press *Save* in the middle window
- Press *Download* (↓) in the middle window
- Type in the left command window:  
    &1 B2 R
- Set motor #10 home by typing in the left command window:  
    #10HMZ

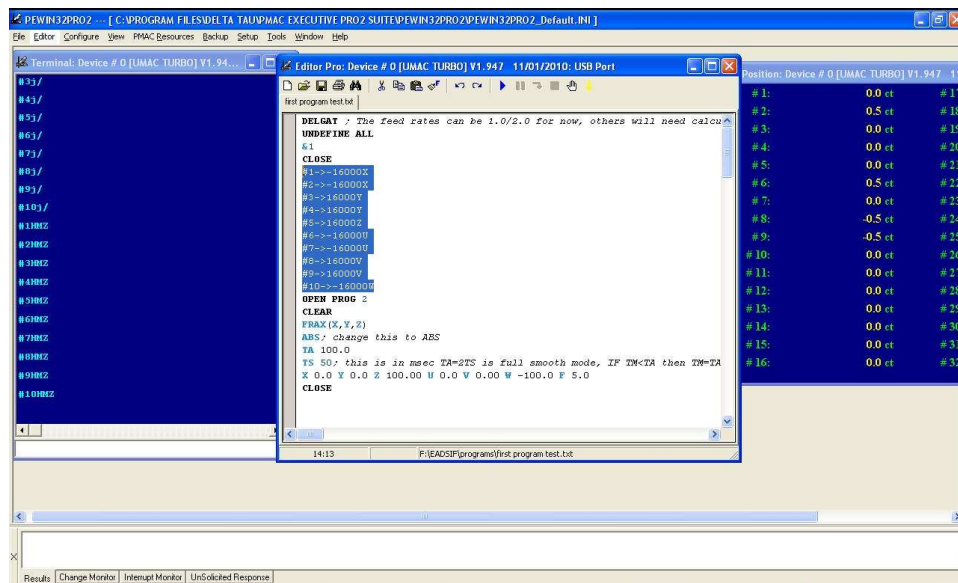


Figure 7.10 Interface of first program test.txt

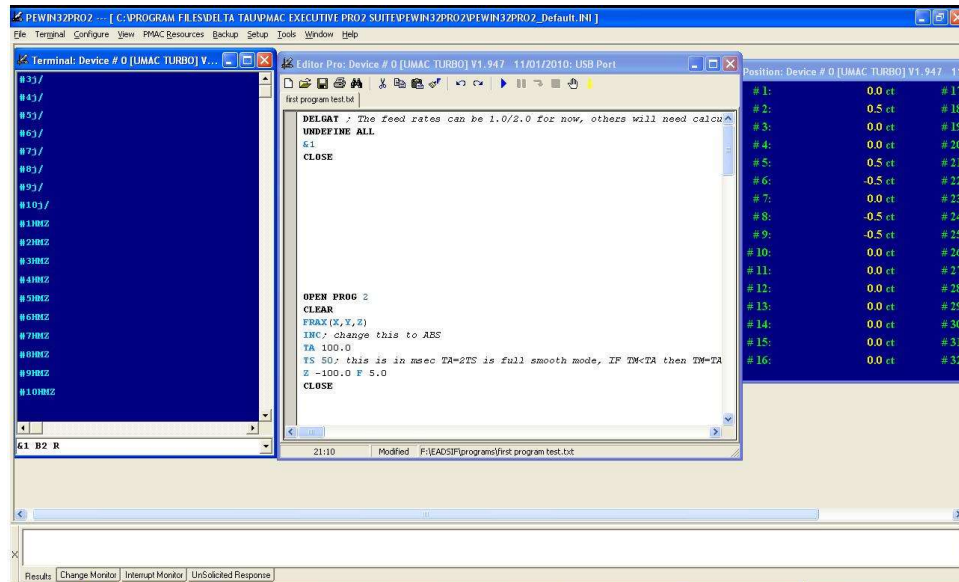


Figure 7.11 change first program test

The motors are now all homed. But before the next step, the bottom tool should be back down to -100.0.

- Change INC to ABS
  - X 0.0 Y 0.0 Z 100.0 U 0.0 V 0.0 W -100.0
  - Save, download and run (&1 B2 R)
  - Check the right window if both motor #5 and #10 are at 1,600,000 while the rest of the motors are 0
- d. Apply lubricant at the forming area on both sides of the sheet
  - e. Clamp the lubricated sheet in the fixture
  - f. Open the toolpath center files

Select *File* → *Open File* → *My Computer* → *F:* → *EADSIF* → *programs* → *your file* → select *text files* in *Files of type* → open your toolpath center file

- g. Open Labview

- Double click the *12 channel LabVIEW* program on the desktop
- Hit run and select the location where you want to place your force file

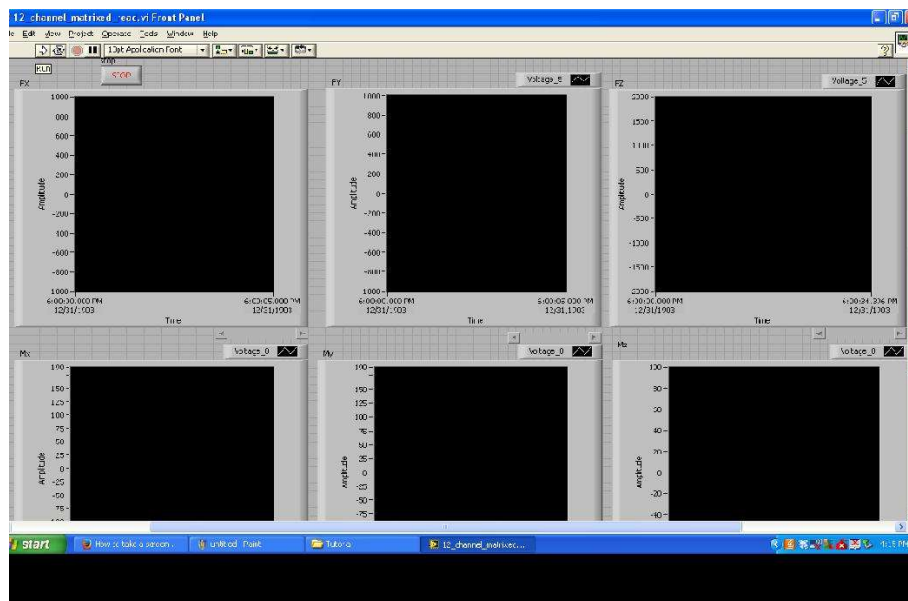


Figure 7.12 LabVIEW Interface

h. Run the toolpath

In the PEWIN program:

- Press *Save* in the middle window
- Press *Download* ( $\downarrow$ ) in the middle window
- Type in the left command window :  
 $\&1 B2 R$

i. After forming

- Open *first program test.txt*
- Lift the bottom tool and bring down the bottom tool by  
 ABS  
 $Z 100.0 W -100.0$
- Save, download and run ( $\&1 B2 R$ )
- Bring the top tool to (0 0 100) and bottom tool to (0 0 -100)  
 $X 0.0 Y 0.0 Z 100.0 U 0.0 V 0.0 W -100.0$

- Save, download and run (&1 B2 R)
- Check the right window if both motor #5 and #10 are at 1,600,000 while the rest of the motors are 0
- Take out the sheet
- Turn off the devices
- Plug off the connection cable
- Shut the lid of the control box

## Appendix B

Matlab code for geometric deviation/thickness

```

clear all;clc
datapath='directory here';
data=load([datapath, 'data here']);
xip=0:0.1:35;
o=data.desired;
a=data.experiment;
o1 = interp1(o(:,1),o(:,2),xip);
a1 = interp1(a(:,1),a(:,2),xip);
error = zeros(length(o1),1);
slope=diff(o1)./diff(xip);
size(o1)
size(slope)

g=1;
for i=1:length(error)-1

    if slope(i)~=0
        l1=[-1/slope(i),o1(i)+1/slope(i)*xip(i)];
        for j=1:1000
            y1=a1(g);y2=a1(g+1);x1=xip(g);x2=xip(g+1);
            l2=[(y2-y1)/(x2-x1),(y1*x2-y2*x1)/(x2-x1)];
            A=[l1(1),-1;l2(1),-1];
            B=[-l1(2);-l2(2)];
            point=A\B;
            if point(1)<xip(g)
                g=g-1;
            elseif point(1)>xip(g+1)
                g=g+1;
            else
                break
            end
            if g==0;g=1;point=[nan;nan];break;end
            if g==length(a1);g=length(a1)-1;point=[nan;nan];break;end
        end
    end

error(i)=sqrt((o1(i)-point(2))^2+(xip(i)-point(1))^2);
else
    error(i)=abs(o1(i)-a1(g));
end
end
plot(error)
E = sqrt(sum(error.^2)/length(error))

```



## Appendix C

### Tutorial for EA-ISF setup

#### Before Use

- a. DO NOT conduct the experiment alone

At least two operators are required to conduct the EA-ISF experiments. One student should be in charge of the electricity related issues and the other in charge of the DSIF machine related items.

- b. Stop both the power supply and the DSIF machine in emergency

When smoke, sparks, unexpected high temperature are observed, terminate the experiment immediately by stopping both the power supply and the DSIF machine.

- c. Be very careful with the electricity

Operators should look after each other, approach to 911 or the research safety department when there is an electric shock. Always check the electrical insulation before turning on the power supply. DO NOT touch any part within the electrical circuit after the power supply is turned on.

- d. Be careful of the heat

After a part is being formed, the tools can be very hot, detect the temperature with the IR camera before touching the tools.



## Electrical insulation

### a. Machine/load cell

To insulate the machine from the circuit, electrically insulated materials such as ceramic, nylon, PVC, etc. are used to machine the adapter between the DSIF machine and the tool holder. Then, the electrical insulated adapter and the tool holder can be assembled with the DSIF machine.

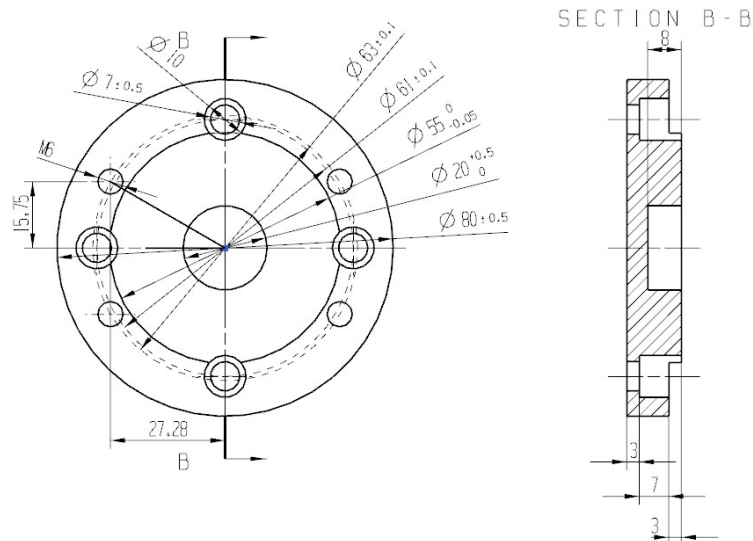


Figure 1 Drawing of the tool holder adapter

Also check the working temperature of the adapter's material and make sure that the temperature at any part of the adapter is beneath that value. Forced air can be used for cooling purposes.

### b. Sheet metal

To electrically insulate the workpiece from the machine during the forming process, electrical tape is used to cover the entire clamping area of the sheet metal.

### c. Inspection

Use the multimeter to check the insulation between the tool holders and the loadcells, the workpiece and the machine. Additionally, check the condition of the cables from the power supply.

### **Operation procedures**

a. Electrical circuit built-up

Utilize the cylindrical metal parts of the tool holders as the terminals of the electricity. Note that cables should be placed in distance with each other and avoid tangles. Check the insulation again.

b. Temperature measurement

After the establishment of the electrical circuit, place the IR camera so that its window can capture the whole field of the forming process. Adjust the focus. Note that the emissivity differs with material and temperature, make sure that the IR camera is calibrated by the thermocouple with the same material (with the same paint or lubricant to be used in the forming process) first.

c. Operation procedures

- Apply solid lubricant ( $\text{MoS}_2$ ) on both sides of the sheet
- Start the recording systems (load, temperature)
- Start the DSIF machine with the pre-generated toolpath (refer to Appendix B)
- Turn on the power supply after the tools are in contact with the sheet
- After one center file, stop the power supply

- After loading the new center file, start the power supply and wait till the temperature rises, then start the toolpath
- Make sure everything is turned off before leaving